

**Dependency of deformation of cell nucleus
on stretch direction of tissue:
Relation to anisotropic response of
aortic media to hypertension**

Fan Yong

**Dependency of deformation of cell nucleus
on stretch direction of tissue:
Relation to anisotropic response of
aortic media to hypertension**

Fan Yong

A thesis submitted in fulfilment of the requirement for the award of the

Doctor of Philosophy

Department of Mechanical Systems Engineering

Graduate School of Engineering

Nagoya University

2022

ACKNOWLEDGEMENT

It is my great pleasure to acknowledge all the people who concerned about this work.

First of all, I would like to thank Professor Takeo Matsumoto from the Department of Mechanical Systems Engineering, Nagoya University. A high-level professor like him still works so hard every day, which always shocks me and encourages me to be a better researcher. During these years, I have learned from him not only the biomechanical knowledge, what is more important, his rigorous attitude towards research, science, and daily life. I was lucky and grateful for being his student.

Then, I would like to thank Dr. Junfeng Wang from the Biomechanics research group. During these years, he has offered me so much guidance and help not only on my experiment but also in my life in Japan during my hard time, like a family. I wish him greater achievements in his future research.

I would like to thank Dr. Jeonghyun Kim, an older brother from this research group. He helped me revise my English writing of my paper and doctoral thesis. He is always concerned about my situation with his kind-hearted advice. We had a great year of happiness.

I would like to thank Prof. Eijiro Maeda from this research group. He helped me revising the first paper and offered submission advice on my second paper.

I would like to thank Mrs. Satomi Tsuruga from this research group and Mr. Yunteng Fu who has graduated from this lab. It was they who patiently taught me so

much about the experiments during my early day in this laboratory.

I would like to thank Miss Asako Muraki from this research group. She is responsible for my experimental purchasing, and she always reminds me about the school affairs as I always forget something important.

I would like to thank so many other members during these years for their advice and support.

Finally, I would like to thank my parents, who offered me financial support for my study and life. Whenever a hard time I am in, they always stand with me, encouraging me. I miss them so much.

June 2022

Yong Fan

Contents

Acknowledgement

Contents I

Chapter 1 Introduction 1

1.1 Background	1
1.1.1 Structure of the aortic wall	1
1.1.2 Mechanical response of the artery wall to hypertension	5
1.1.3 Structure of the animal cell and mechanotransduction	9
1.2 Hypothesis and Purpose	18
1.2.1 Possible mechanotransduction mechanism of the wall thickening	18
1.2.2 Conceivable reason for the directional difference in mechanical response of the wall	19
1.2.3 Purpose and outline	20
References	22

Chapter 2 Experiment and analysis 27

2.1 Summary of this chapter	27
2.2 Specimen preparation	28
2.2.1 Test model	28
2.2.2 Preparation of the aortic slice	29
2.3 Staining of the smooth muscle cell nucleus and the actin filaments	31
2.4 Stretch test	32
2.4.1 Stretch device and experimental setup	32
2.4.2 Type-1 slice: Circumferential stretch for 2D and 3D analyses	36
2.4.3 Type-2 slice: Axial stretch for 2D analysis	36
2.4.4 Type-3 slice: Axial stretch for 3D analysis	37
2.5 Image processing	39
2.5.1 Imaging processing in 2D	39
2.5.2 Imaging processing in 3D	40

2.6	Deformation analysis	40
2.6.1	Macroscopic deformation of the specimen	40
2.6.2	Heterogeneous deformation of the media	42
2.6.3	Microscopic deformation of the nucleus in 2D	44
2.6.4	Microscopic deformation of the nucleus in 3D	48
2.6.5	Microscopic deformation of actin filament network in 2D	49
2.7	Statistical analyses	59
2.8	Discussion	60
	References	63

Chapter 3	Heterogeneous deformation of the media	64
3.1	Summary of this chapter	64
3.2	Macroscopic shear deformation between the laminae of the media	65
3.3	Microscopic heterogeneous deformation of the media	68
3.4	Discussion	72
	References	75

Chapter 4	Deformation of the actin filament (AF) network against stretch	77
4.1	Summary of this chapter	77
4.2	Deformation of the AF	78
4.2.1	Circumferential stretch	78
4.2.2	Axial stretch	81
4.3	Comparison with the deformation of the homogeneous body	84
4.4	Discussion	85
	References	86

Chapter 5	Deformation of the nucleus against stretch	87
5.1	Summary of this chapter	87

5.2	Deformation and rotation in 2D	88
5.2.1	Circumferential stretch	88
5.2.2	Axial stretch	91
5.2.3	Measurement of deformation of multiple nuclei in each sample slice	95
5.2.4	Comparison with the deformation of the homogeneous body	98
5.2.5	Comparison with the deformation of the AF network	98
5.3	Deformation and rotation in 3D	102
5.3.1	Nuclear deformation in the circumferential and axial stretch	102
5.3.2	Orientation angle change of the nucleus	105
5.3.3	Comparison between 3D and 2D results	107
5.4	Discussion	108
	References	110

Chapter 6 Discussion 111

6.1	Possible causes of the difference in the strain between the nucleus and cell body	111
6.2	Difference in the mechanical properties of the nucleus and cell body cannot explain the difference in strain	112
6.3	Anisotropic nuclear deformation against different stretches: Qualitative explanation	116
6.4	Anisotropic nuclear deformation against different stretches: Quantitative analysis	119
6.5	Comparison of the present results with biaxial stretch case	126
6.6	Deformation of the nucleus and the cell body under physiological condition	128
6.7	Physiological implications: Anisotropic nuclear deformation causes the anisotropic response of aortic media to hypertension	130
6.8	Limitations and future works	131
	References	132

Chapter 7 Conclusions 134

Appendix 136

Chapter 1 Introduction

1.1 Background

1.1.1 Structure of the aortic wall

Blood vessels are the channels of blood flow, which are divided into arteries, veins and capillaries. The arteries start from the heart and continue to branch. The caliber gradually becomes smaller, and the pipe wall gradually becomes thinner. Finally, it is divided into many capillaries, which are distributed among the tissues and cells of the whole body. The capillaries gradually converge into veins and finally return to the heart. Arteries and veins are the pipes for transporting blood, while capillaries are the places for material exchange between blood and tissues.

The aortic wall consists of three layers: intima, media, and adventitia, as shown in Fig. 1.1.

The intima is mainly a monolayer of endothelial cells that contacts with blood, and it senses shear stress produced by the blood flow. In response to low shear stress, endothelial cells make vascular smooth muscle cells (SMCs) in the media contract to increase the wall shear stress back to normal level by releasing endothelin (Ohlstein and Douglas 1993). In response to high shear stress, they make SMCs relaxed to restore the wall shear stress by generating nitric oxide (Ohlstein and Douglas 1993; Douglas et al. 1994; Uematsu et al. 1995; Di et al. 2000). Any imbalance between these two counter-regulatory systems causes pathological consequences within the

cardiovascular system (Ohlstein and Douglas 1993).

The adventitia is mainly made up by loosely connective tissues. The complex vascular adventitia acts as a biological processing center for the retrieval, integration, storage, and release of key regulators of vessel wall function (Stenmark et al. 2011). The resident cells (fibroblasts, dendritic cells, progenitor cells) in the adventitia are the first vascular cells that react biochemically and physiologically to the external stimulation, such as hormonal, inflammatory, and environmental stresses. Such reaction is denoted as an increase in cell proliferation, the expression of contractile and extracellular matrix (ECM) proteins, which in return, affect vascular tone and wall structure. Thus, the adventitia is regarded as “injury-sensing tissue” from “outside” of the vascular wall (Michel et al. 2007; Hu and Xu 2011; Stenmark et al. 2011).

The media is located between the intima and adventitia. The media mainly consists of “sandwiched” structures in which the collagen, elastin fibers and SMCs intervene between every two elastic laminae, *i.e.*, lamellar unit (Wolinsky and Glagov 1967).

The elastic lamella and adjacent interlamellar zone denote the function unit of the structure of the aortic media. These lamellar units of the media are oriented as concentric layers, and the number of lamellar units is proportional to the aortic wall thickness. Smooth muscle protein occupies 20% of the media weight while the elastin and collagen occupy 60%. The three components form well-defined elastic layers. Their close association results in viscoelastic properties that account for many of its

static and dynamic mechanical features (Wolinsky and Glagov 1964).

This work concentrates on the media because it occupies the most thickness and weight of the aorta, its weight proportion is even as high as 80% in rat aorta (Matsumoto and Hayashi 1996), and it occupies most of the elastin and collagen of the vessel, which dominate the aortic anisotropic and hyperelastic passive mechanical behaviors (Dobrin 1978; Zhang 2005; Fonck et al. 2007; Zou and Zhang 2009, 2012; Chow et al. 2014).

The most important three structural components of the artery wall, *i.e.*, smooth muscle cells, collagen and elastin have extremely different Young's modulus. It is about 0.01–0.1 MPa for smooth muscle cells, 1000 MPa for collagen and 0.6 MPa for the elastin (Matsumoto and Nagayama 2012). Such difference makes the complex mechanical property of the media (Valdez et al. 2011; Matsumoto and Nagayama 2012) and may cause a heterogeneous distribution of intramural stress in the loaded wall (Matsumoto et al. 2008) and a complicated distribution of residual stress (Matsumoto et al. 2004). The stress and strain distributions in the artery wall are highly complicated at the microscopic level.

The hypertension results wall stiffening, this disease is often associated with ECM changes including the collagen/elastin ratio, increased media thickness, and reduced fenestration of the elastic lamina (Chow et al. 2014). Hypertension increase the deformation of the vessel, *i.e.*, circumferential stress, which may induce large losses of elastin content along with the fragmentation of the elastic laminae/fibers (Humphrey 2008; Boumaza et al. 2001). During this process, the collagen begins to

be recruited to bear the major load applied on the artery, and as the collagen fibers are almost three orders of magnitude stiffer than elastic fibers, the collagen recruitment increase the stiffness of the arteries (Chow et al. 2014).

Figure 1.2 shows the structure of the elastic artery. A layer of endothelial cells orderly arranged in the intima. The concentric elastic lamellae occupy the main thickness of the media, with SMCs, collagen fibers and collagen fibrils sandwiched among them. Other tissues or cells like fibroblast, unmyelinated nerves and macrophages distribute in the adventitia.

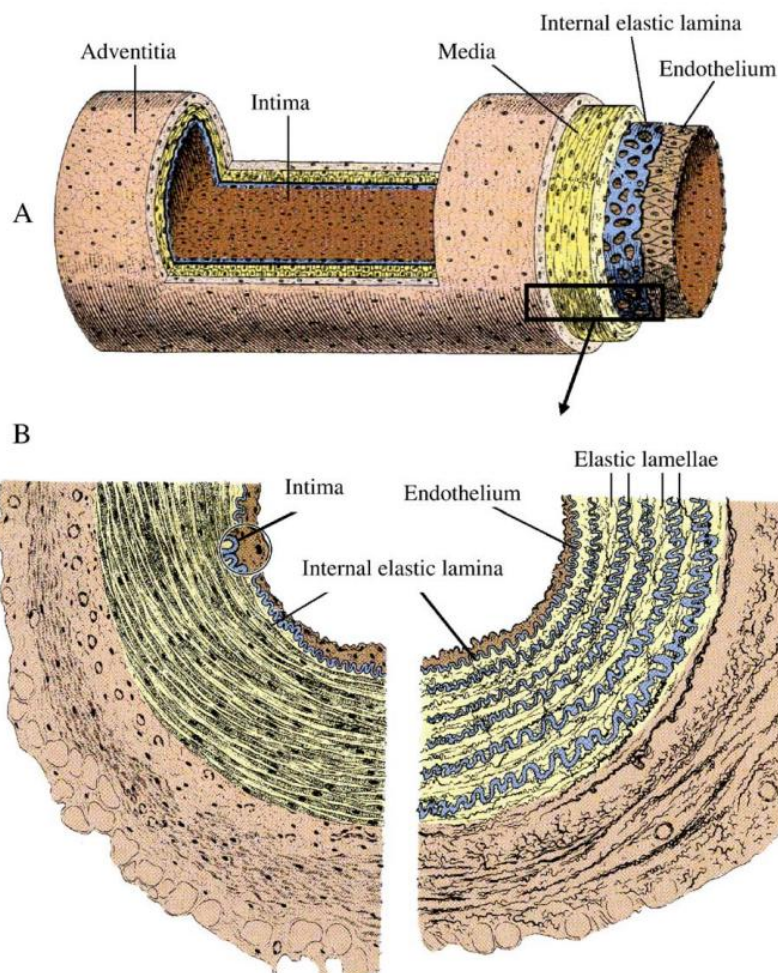


Fig. 1.1 The structure of blood vessels showing three layers (A). The distribution of elastin within the vessel wall is shown for a muscular artery (left) and elastic artery (right) (B) (Junqueira and Carneiro 2005).

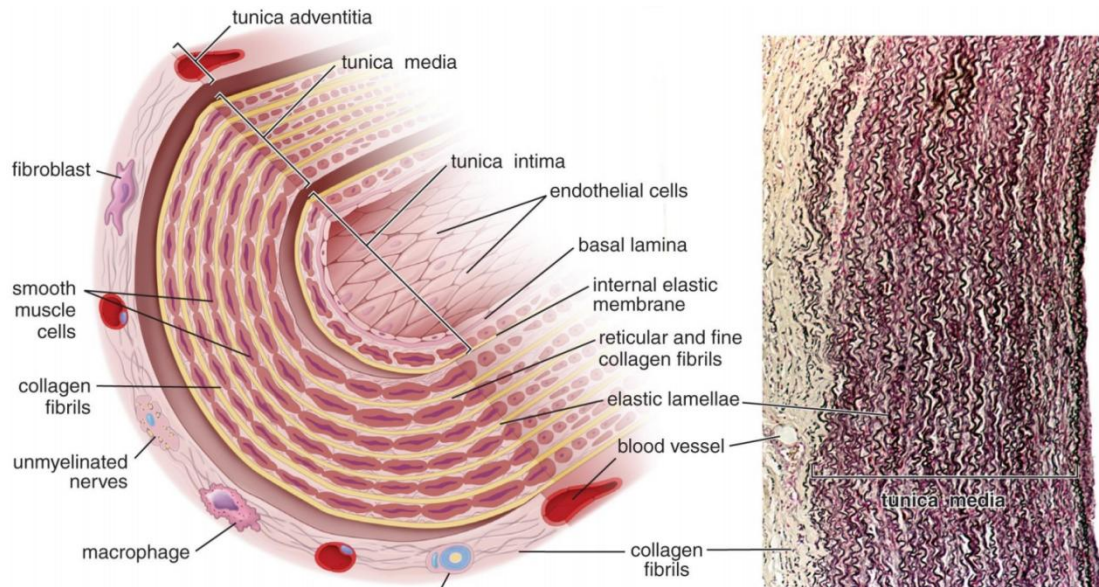


Fig. 1.2 The composite structure of elastic artery (Michael and Wojciech 2011).

1.1.2 Mechanical response of the artery wall to hypertension

Hypertension causes severe cardiovascular, neurovascular, and renovascular diseases, including heart attacks, stroke, and end-stage kidney failure (Humphrey et al. 2009). While it is well known that biological tissues change their dimensions and mechanical properties adaptively in response to mechanical stimulation, the aortic walls also alter their dimensions and mechanical properties in response to mechanical stimulation under the hypertension (Wolinsky and Glagov 1964; Wolinsky 1971, 1972; Vaishnav et al. 1990, Matsumoto and Hayashi 1994, 1996; Folkow 1987). For example, the vessel increases its wall thickness i.e., hypertrophy as a response to hypertension (Wolinsky 1971, 1972; Folkow 1987; Matsumoto and Hayashi 1994;

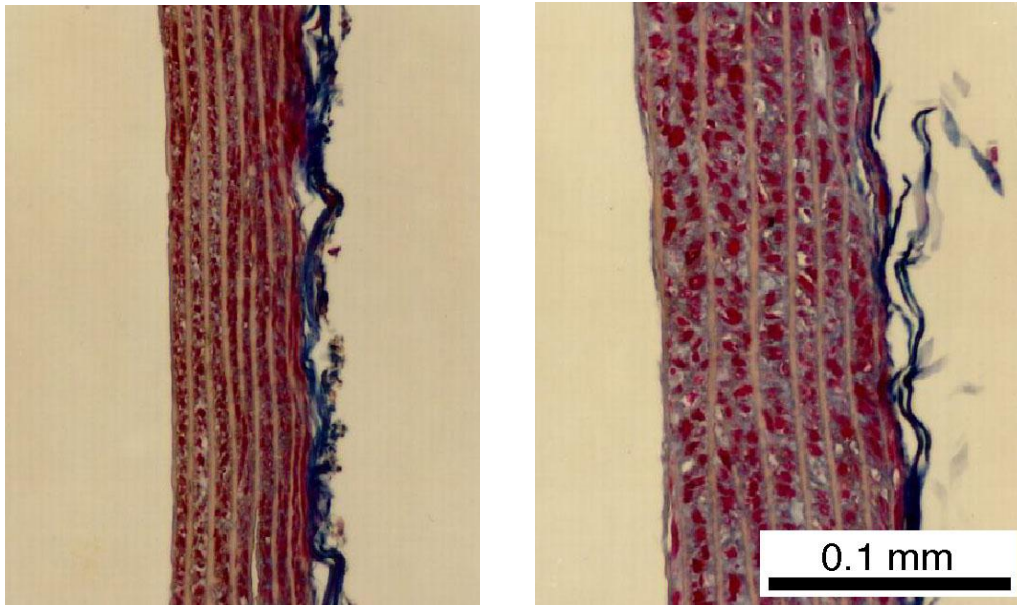
Vaishnav et al. 1990) as represented in Fig. 1.3. The images show the normotensive and hypertensive thoracic aorta of rats, we can see obvious wall thickening caused by hypertrophy of the lamellar units instead of increase in the number of the lamellar units.

The hypertrophy of the media occurs because of the increase of extracellular matrix (ECM) (Wiener et al. 1977; Owens and Schwartz 1983; Matsumoto et al. 1999) and the increase in SMC volume. With the development of the hypertension, the hypertrophic SMCs produce more ground substances of ECM such as elastin, collagen and glycosaminoglycan (Ito 1989; O'Callaghan and Williams 2000; Stanley et al. 2000; Haga et al. 2007). Particularly, the hypertrophy of the lamellar units occurs in the sub-intimal region (Matsumoto and Hayashi 1996). The nonuniform hypertrophy in the radial direction, *i.e.*, gradual decrease from the inner wall toward the outer wall may be caused by the nonuniformity of the intramural mechanical environment: the magnitudes of the strain and stress are larger in the inner wall than in the outer wall, especially in the circumferential direction (Matsumoto and Hayashi 1996), which means larger mechanical stimuli to the nucleus near the inner wall. Fig. 1.4 represents such hypertrophy of the lamellar units especially near the subintimal space. Selective thickening near the inner wall is evident in the severely hypertensive case (Fig.1.4 (c)).

One of the main causes of the media hypertrophy is the volume increase of SMC (Owens 1989). It has been reported that hypertrophy of SMCs occurs in the direction perpendicular to their axial direction but not in their axial direction

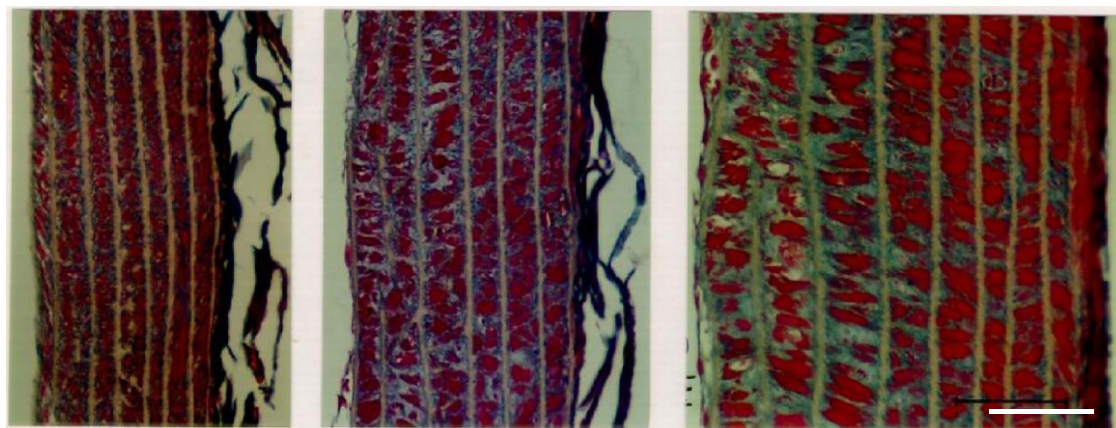
(Matsumoto et al. 2011). As the spindle-shaped SMCs show a helical pattern along a predominantly vascular circumferential direction (Takamizawa et al. 1992; Matsumoto et al. 1999; Valdez et al. 2011), they may become hypertrophied in the vascular radial and axial directions equibiaxially in response to hypertension. If this is the case, the radial hypertrophy of the SMC may cause the wall thickening, and the axial hypertrophy of the SMC may cause increased axial length of the artery at no-load state.

In fact, Matsumoto and Hayashi (1996) reported that axial stress decreased significantly in response to hypertension, while circumferential stress remained unchanged. The hypertrophic mechanism of the wall remains unclear, so does the reason for the unchanged circumferential and the decreased axial stress. When the vessel is removed from the body, *i.e.*, from physiological state to no-load state, the axial length will decrease, as shown in Fig.1.5. Other studies pointed out that the mechanical response of the vessels is not isotropic. The wall thickening in response to the hypertension is thought to occur to maintain the circumferential stress developed under normal *in vivo* condition (Wolinsky 1971, 1972; Matsumoto and Hayashi 1994, 1996; Folkow 1987; Vaishnav et al. 1990; Berry and Greenwald 1976). In contrast, the wall thickening does not maintain the stress in the longitudinal direction as concisely illustrated in Fig. 1.5. It has been reported that no load length of the aorta increases in response to the hypertension (Vaishnav et al. 1990, Matsumoto and Hayashi 1994), as shown in Fig.1.5 lower left, thus the longitudinal stress in the hypertensive aorta decreases significantly (Matsumoto and Hayashi 1996).



(a) Normotension ($P_{sys} = 140$ mmHg) (b) Hypertension ($P_{sys} = 255$ mmHg)

Fig. 1.3 Hypertrophy of rat thoracic aortas caused by hypertension. Normotensive (a) and hypertensive (b) aortas were stretched and pressurized to restore in vivo dimensions, fixed with formalin, and stained with Azan-Mallory (red, smooth muscle cells; blue, collagen; pale brown, elastic lamina) (Matsumoto and Hayashi 1996). P_{sys} , systolic pressure.



(a) $P_{sys} = 145$ mmHg (b) $P_{sys} = 200$ mmHg (c) $P_{sys} = 240$ mmHg

Fig. 1.4 Thickening of the lamellar units of the media in three aortas fixed under the in vivo loading condition and stained with Azan-Mallory. In case of normotensive rat (a), the thickness of the lamellar unit is almost uniform along the wall thickness, while in case of severely hypertensive animal (c), the thickening of the inner units are remarkable. The length marker ($50\text{ }\mu\text{m}$) in (c) applies to all (Matsumoto and Hayashi 1996).

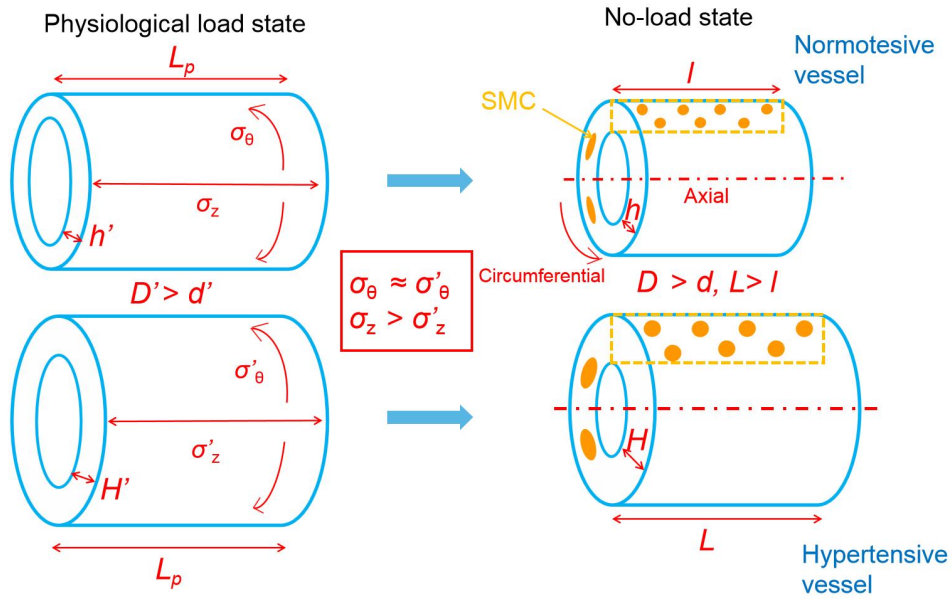


Fig. 1.5 The circumferential stress remains unchanged when the hypertension occurs, but not for the axial stress. H and h represent no-load wall thickness of normotensive and hypertensive vessel; H' and h' represent normotensive and hypertensive wall thickness of the vessel at physiological load state; l and L represent no-load lengths of normotensive and hypertensive vessel; L_p represent the length of the vessel at physiological load state.

1.1.3 Structure of the animal cell and mechanotransduction

In biological systems, cell is the smallest unit that can live on its own and that makes up all living organisms and the tissues of the body. An animal cell is mainly composed of the cell membrane, the cytoskeleton, the nucleus and other cell organelles like endoplasmic reticulum, Golgi body, lysosome, mitochondria and peroxisome, etc.

The cell membrane

The cell membrane is mainly an elastic semi-permeable membrane composed of phospholipid bilayer. For animal cells, the outside of the membrane is in contact with

the external environment. Its main function is to selectively exchange substances, absorb nutrients, discharge metabolic wastes, secrete and transport proteins. Fig. 1.6 shows immunofluorescently stained plasma membrane in the human cell line U-2 OS.

The cytoskeleton

There are three kinds of cytoskeletons: microtubule, intermediate filament and microfilament (Fig. 1.7). They are important in maintaining cell shape and generating force for the intracellular and extracellular movements. The microtubules are polymers of tubulin that form part of the cytoskeleton, and it provides structure and shape to animal cells, and plays an important role in intracellular material transport. The intermediate filaments are ropelike fibers that extend across the cytoplasm, giving cells mechanical strength and carrying the mechanical stresses in a epithelial tissue by spanning the cytoplasm from one cell-cell junction to another (Bruce et al.1994). The microfilament is made up of actin, so it is also called actin filament (AF). Bundles of actin filaments constitute the main body of the stress fiber (SF) (Fig. 1.8 lower), whose ends are connected to the extracellular matrix (ECM) or substrate *via* focal adhesions, which is responsible for the perception of extracellular mechanical signals and exchange of intracellular biochemical signals (Fig. 1.8 upper).

The nucleus

The nucleus is the site for the storage, replication, and transcription of genetic material, which is known for deoxyribo nucleic acid (DNA). The nucleus is

separated from the cytoplasm by a double-layer porous nuclear membrane. Nuclear pores distributed on the nuclear membrane act as the channels for macromolecular substances to pass through under the help of carrier proteins. Chromatin is a complex structure composed of DNA chain, histone, non-histone, and a small amount of ribonucleic acid (RNA).

Nagayama et al. (2011) observed marked local deformation of the nucleus as well as disappearance or re-distribution of the intranuclear DNA after dissecting the SFs in rat embryonic aortic SMCs (A7r5 cells). After dissecting the stress fibers, they found that the nucleus moved toward the AF retraction and dissecting the stress fibers also deformed the nucleus and eventually induced conformational changes of chromatin (Fig. 1.9).

Other cellular organelles

Some other cellular organelles also exist in the cytoplasm, where most biochemical reactions and transformation of biochemical signals occur. The endoplasmic reticulum acts as the transportation system, and it has functions such as protein folding. The Golgi body, as a part of the endomembrane system, packages proteins into membrane-bound vesicles inside and send the vesicles to their destination. The lysosomes act as the waste disposal system of the cell; the mitochondria generate most of the cell's supply of adenosine triphosphate (ATP) through aerobic respiration, which is subsequently used as a source of chemical energy for the cell. The peroxisome plays a key role in lipid metabolism and the

conversion of reactive oxygen species.

About the mechanotransduction

The process that individual cells sense mechanical signals and transduce them into changes in intracellular biochemistry and gene expression is called mechanotransduction (Wang et al., 2009). Some examples of mechanotransduction will be introduced here.

The ends of the SFs are connected to the extracellular matrix (ECM) via the focal adhesions, by which the extracellular mechanical signals are transferred to biochemical signals and transmitted to the inside of the cell through the SF (Figs. 1.8 and 1.10). The SF also links the nucleus via the linker of nucleoskeleton and cytoskeleton (LINC) proteins (Wang et al. 2009; Wang et al. 2018; Davidson et al. 2021). LINC complex is a generic term of nesprin, protein UNC-83 homolog A (it is often called SUN1), protein UNC-84 homolog B (it is often called SUN2), and other nuclear components that are distributed in the envelope of the nucleus. The LINC complex exchanges and transmits mechanical or biochemical signals between the ECM and the nucleus. Fig. 1.11 simply shows how the SF of cytoskeleton link the plasma membrane and the nucleus (Wang et al. 2009, Wang et al. 2018).

Generally, the focal adhesion is physically coupled to cytoskeletal filament networks that, in turn, link to the nucleus (nuclear scaffolds of lamin, nucleolus, chromatin, etc.) via LINC complex. When an extracellular physical force is applied to the cell surface, it distorts the membrane in the cell surface then it is transmitted

through the AF to the nucleus by promoting deep structural rearrangements in the cytoplasm and nucleus (Wang et al. 2009), then, induce the conformational chromatic changes (Nagayama et al. 2011).

The stress transmitted through the SF to the nucleus is thought to cause a dispersion of the chromatin, enhancing the protein synthesis. Tajik's group controlled magnetic beads to apply the mechanical stress on the cellular surface to deform the nucleus (Tajik et al. 2016). By stimulating the nucleus, the local surface force is propagated via integrins, tensed actin myosin and LINC to the nucleus. Then, the transmitted force stretched the flanking chromatin to induce its dispersion. By quantitatively detecting the amount of protein expressed by the dihydrofolate reductase (DHFR) gene, they found the significant enhancement of protein expression along with increased duration of stress as shown in Fig. 1.12.

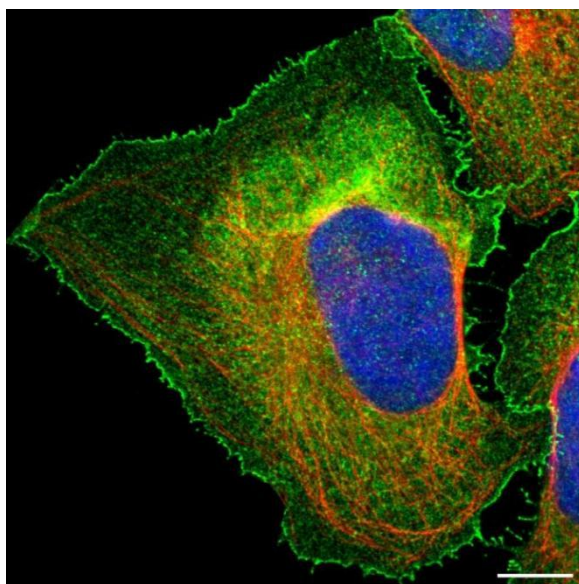


Fig. 1.6 Staining of plasma membrane in human cell line U-2 OS. Scale bar represents 10 μ m. Green, cell membrane; blue, nucleus; red, microtubules. (<https://v15.proteinatlas.org/learn/dictionary/cell/plasma+membrane+2>).

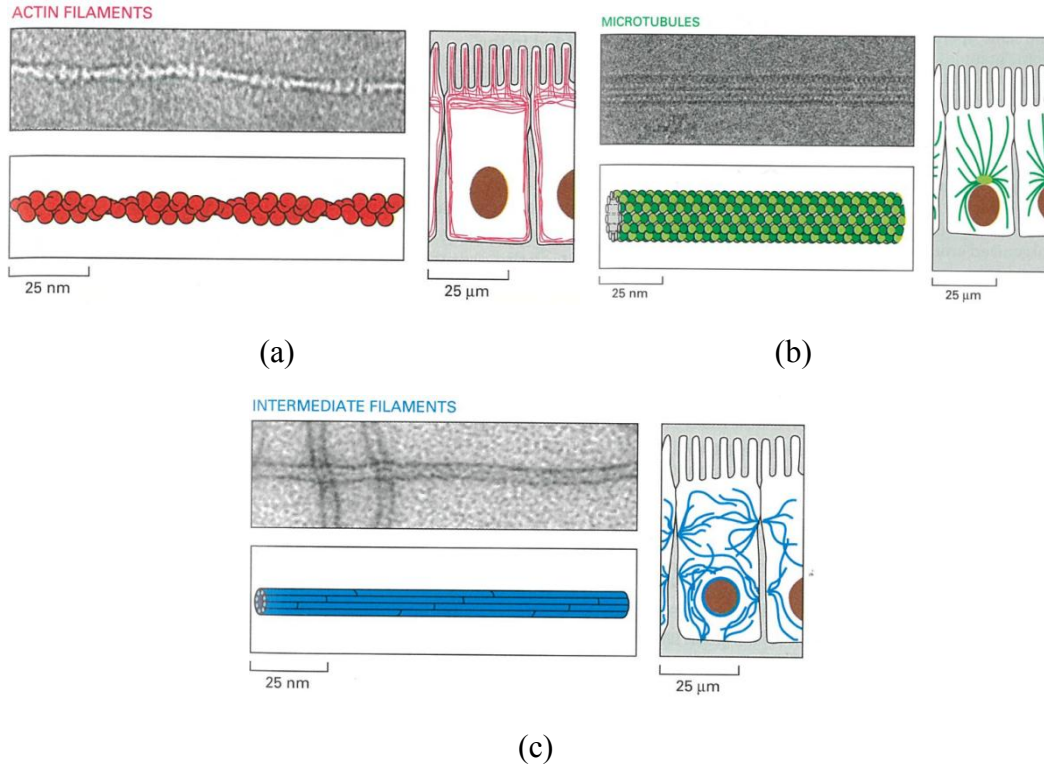


Fig. 1.7 The three types of protein filaments that form the cytoskeleton. Actin filaments (a), microtubules (b), and intermediate filaments (c) (Bruce et al. 1994).

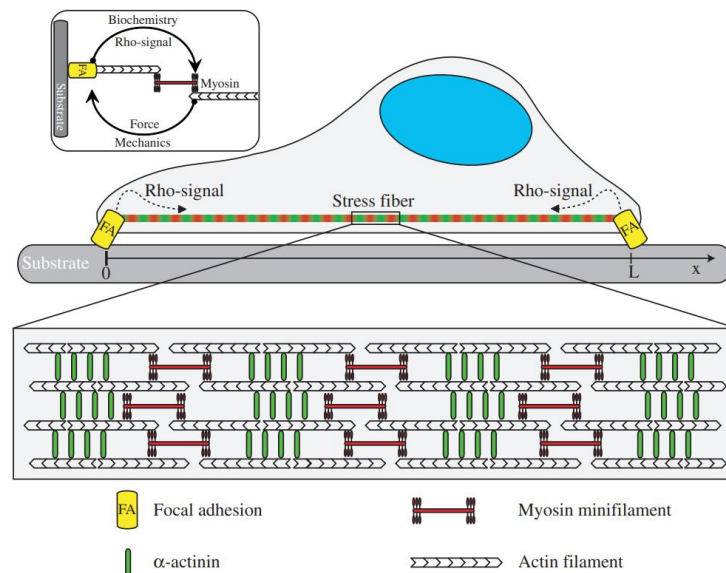


Fig. 1.8 Scheme of stress fiber structure. Rho-signal is a kind of biochemical signals. The mechanical stimuli triggers Rho-signal that originate from focal adhesions and propagate into the cytoplasm, altering in turn myosin activity thus regulate and modify the cell migration (Besser et al. 2007).

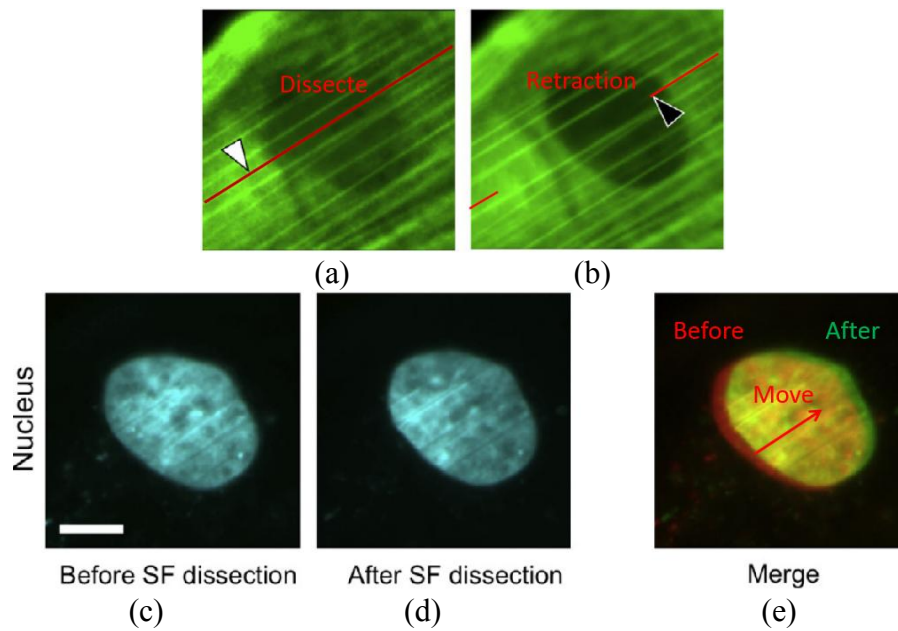


Fig. 1.9 The nucleus moves along the direction of AF stress fibers retraction. SFs and nucleus before (a, c) and after (b, d) dissection of a single SF. The nuclear moved after the dissection (e). The arrowheads in (a, b) indicate the dissection point (Nagayama et al. 2011). A white bar indicates 10 μm .

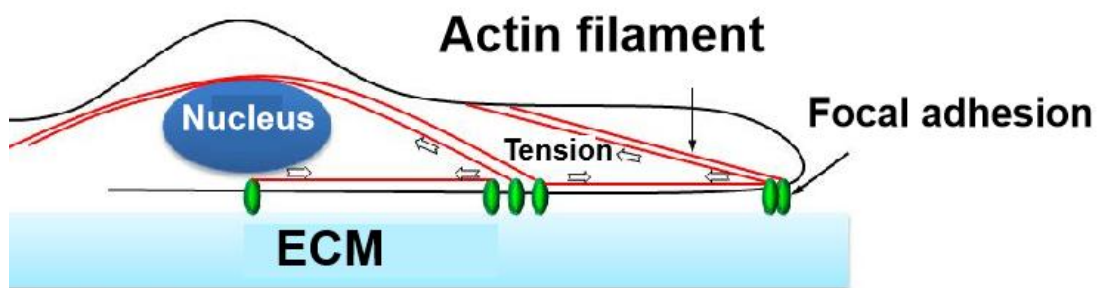


Fig. 1.10 A simplified illustration of cytoskeletal AF stress fibers. The SFs are distributed around the nucleus, the focal adhesion perceive the extracellular mechanical stimuli, then the SFs contract to generate tension stress to stimulate the nucleus *i.e.* stress transmitted through the SF to the nucleus (Wang 2016).

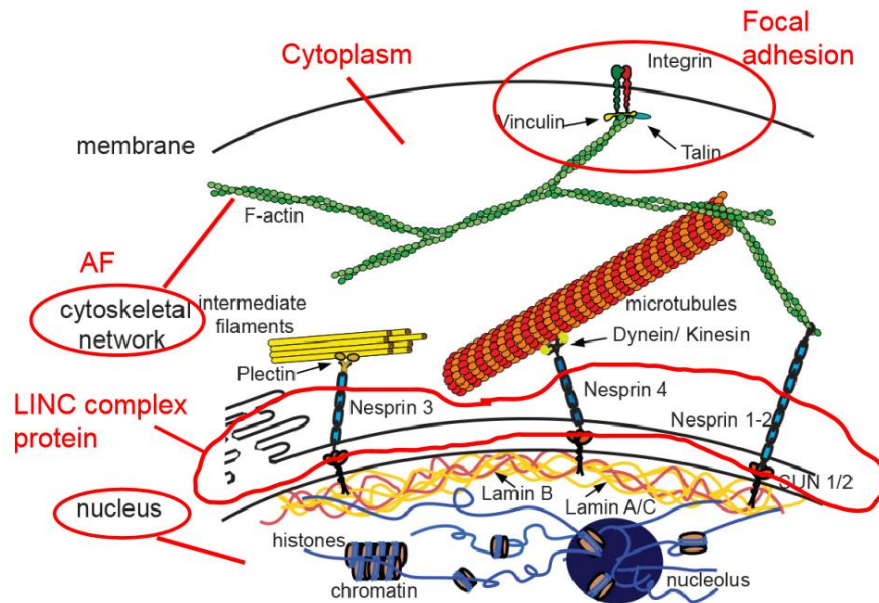


Fig. 1.11 A simplified illustration showing the AF link between the nucleus and the cytoplasm (Wang et al. 2018).

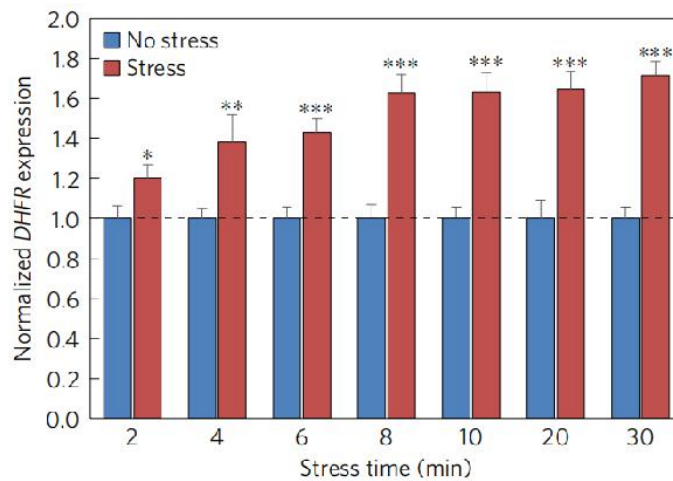
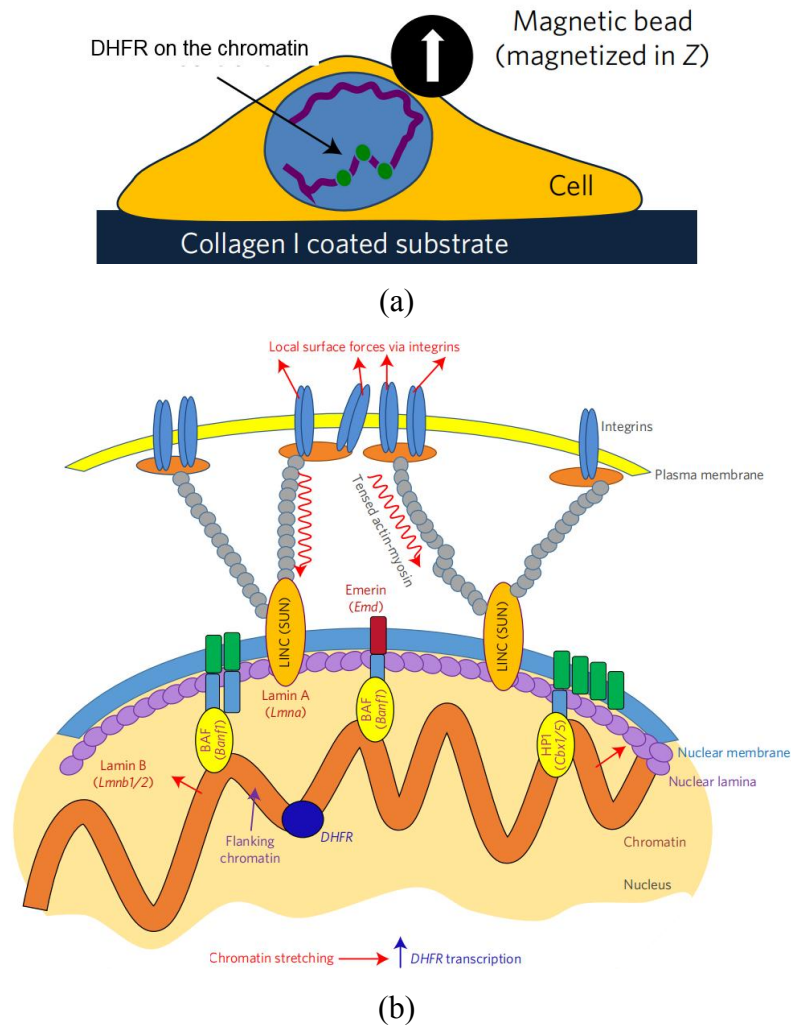


Fig. 1.12 The stress applied on the cellular surface stretched the chromatin and induce protein expression enhancement. Applying stress on the cellular surface to deform the nucleus by magnetic beads (a). The local force is transmitted to the nucleus (b). DHFR gene expression was significantly enhanced (c) (Tajik et al. 2016).

1.2 Hypothesis and Purpose

1.2.1 Possible mechanotransduction mechanism of the wall thickening

Among many possible mechanisms explaining the wall thickening, this dissertation focuses on the nucleus deformation against the mechanical stimulations.

Taking all those background into consideration, it is hypothesized that an increased deformation of the artery wall due to hypertension causes an increase in the nuclear deformation. Then, the increased nuclear deformation elicits a dispersion of chromatin which is normally densely packed in the SMC nuclei and eventually enhances transcription, translation, and protein expression. Fig. 1.13 represents the hypothesis in this dissertation explained above. In this work, it is assumed that the wall thickening is induced by the stimuli transmitted to the nucleus. Hence, it is thus essential to explore the nuclear deformation behavior of the SMC when the vessel is subjected to the mechanical stimuli.

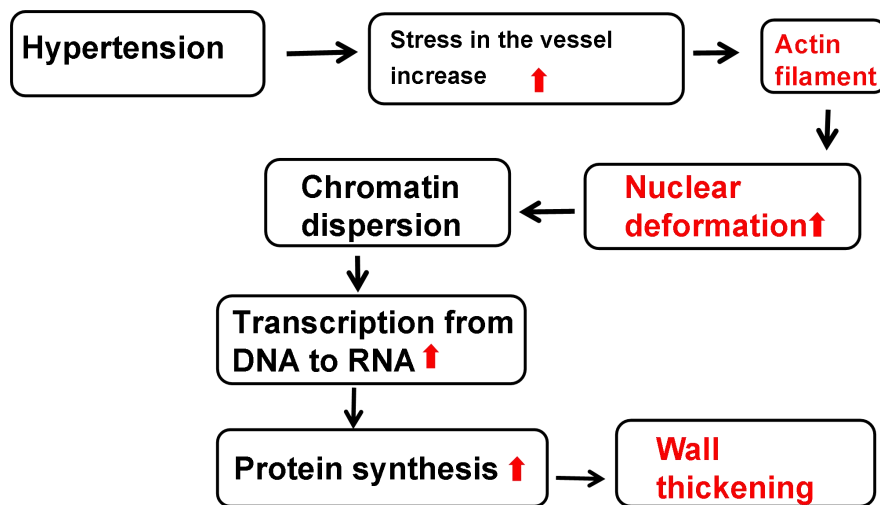


Fig. 1.13 Hypothesis of possible hypertension mechanism in this dissertation.

1.2.2 Conceivable reason for the directional difference in mechanical response of the wall

Why does the vessel exert the anisotropic response to the mechanical stimulation?

Based on all the knowledge above, this work proposes a possible mechanotransduction mechanism of the wall thickening. The directional difference in the nuclear deformation in response to the stretch may explain the directional difference in the mechanical response of the aorta to the hypertension.

As the SFs aligned mainly along the nuclear longitudinal direction (circumferential direction of the vessel), when the cell is stretched, the mechanical stimuli are more easily and effectively transmitted to the nucleus in its longitudinal direction (circumferential direction of the vessel) than other directions (transversal direction of the nucleus *i.e.* axial direction of the vessel), which explains the greater deformation in the nuclear longitudinal direction.

Or we can explain the anisotropic response of the vessel like this: Let us assume first that the hypertrophy of the SMC as well as the excretion of the ECM proteins occurs equibiaxially in the plane perpendicular to the stretched direction of a cell. If the nucleus is more sensitive to the circumferential stretch of the vessel, it is mainly the circumferential stimuli that induce hypertrophy of the SMC in its radial and axial directions of the vessel. The radial hypertrophy of the cell and the increased ECM make the media hypertrophy to maintain the circumferential stress unchanged; the axial hypertrophy of the cell induced the decreased stress of the vessel.

1.2.3 Purpose and outline

To answer this, this work aims to explore the SMC nuclear deformation against the mechanical stretch in the circumferential and axial directions. Since the hypertrophy develops gradually from the normal state of blood vessels. In the present experiment, the specimens cut from the normotensive vessel tissue were used to perform tensile tests to explore the underlying mechanism.

Additionally, since the nuclei are surrounded and sustained by the cytoskeleton inside the cell, the AF is thought to play a significant role in the deformation of the nucleus while the stress applied to the aortic wall is transmitted to the chromatin inside the nuclei through the cytoskeleton (Crisp et al. 2006; Davidson and Cadot 2021). Hence, this dissertation aims to measure the deformation of the AF network.

This dissertation consists of seven chapters. In Chapter 1, the background of the research and describe my research aims will be introduced. In Chapter 2, the procedures of the tensile experiments, methods for processing the images obtained from the experiment, analyzing methods for the macroscopic deformation of the specimens, the heterogeneous deformation of the media, and the microscopic deformation of the nucleus and the microscopic deformation of AF network will be introduced. In Chapter 3, the heterogeneous deformation of the media against circumferential stretch is evaluated. The shear deformation between the laminae of the media is calculated by using the results of circumferential stretch. Then, the heterogeneous deformation by calculating the Green strain distribution of the media

during stretch was evaluated. In Chapter 4, the 2D deformation of the AF network against stretch was evaluated and it was compared to the deformation depending on the homogeneous assumption. In Chapter 5, the 2D and 3D deformations of the SMC nuclei against stretch were evaluated and they were compared to the AF and to the deformation of the nuclear peripheral cell body depending on the homogeneous assumption. In Chapter 6, the results will be discussed regarding following points: 1) the different deformation between the nucleus and the surrounding cell body, and 2) the anisotropic nuclear deformation to the stretch. And finally in Chapter 7, the conclusions of the thesis will be summarized.

References

- Berry CL, Greenwald SE (1976) Effects of hypertension on the static mechanical properties and chemical composition of the rat aorta. *Cardiovasc. Res.* 10:437–451.
- Besser A, Schwarz US (2007) Coupling biochemistry and mechanics in cell adhesion: a model for inhomogeneous stress fiber contraction. *New. J. Phys.* 9.
- Bruce A, Dennis B, Julain L, Martin R, Keith R, James DW (1994) *Molecular biology of the cell*. Garland Publishing, Inc. New York, pp. 788–789.
- Boumaza S., Arribas SM, Challande P (2001) Fenestrations of the carotid internal elastic lamina and structural adaptation in strokeprone spontaneously hypertensive rats. *Hypertension*. 37:1101–1107.
- Chow MJ, Turcotte R, Lin CP, Zhang Y (2014) Arterial extracellular matrix: A mechanobiological study of the contributions and interactions of elastin and collagen. *Biophys. J.* 106(12):2684–2692.
- Crisp M, Liu Q, Roux K, Rattner JB, Shanahan C, Burke B, Stahl PD, Hodzic D (2006) Coupling of the nucleus and cytoplasm: Role of the LINC complex. *J. Cell. Biol.* 172:41–53.
- Davidson PM, Cadot B (2021) Actin on and around the nucleus. *Trends. Cell. Biol.* 31:211–223.
- Di LG, Bhargava J, Powell RJ (2000) Vascular smooth muscle cell effect on endothelial cell endothelin-1 production. *J. Vasc. Surg. Cases*. 31(4):781–789.
- Dobrin PB (1978) Mechanical Properties of Arteries. *Physiol. Rev.* 58(2):397–460.
- Douglas SA, Loudon C, Vickery-Clark LM (1994) A role for endogenous endothelin-1 in neointimal formation after rat carotid artery balloon angioplasty. Protective effects of the novel nonpeptide endothelin receptor antagonist SB. *Circ. Res.* 75(1):190–197.
- Folkow B (1987) Structure and function of the arteries in hypertension. *Am. Heart J.* 114:938–948.
- Fonck E, Prod'homme G, Roy S, Augsburger L, Rü DA, Stergiopoulos N (2007) Effect of elastin degradation on carotid wall mechanics as assessed by a constituent-based biomechanical model. *Am. J. Physiol. Heart. Circ. Physiol.* 292:2754–2763.

Haga JH, Li Y-SJ, Chien S (2007) Molecular basis of the effects of mechanical stretch on vascular smooth muscle cells. *J. Biomech.* 40:947–960.

Humphrey JD (2008) Mechanisms of arterial remodeling in hypertension: coupled roles of wall shear and intramural stress. *Hypertension*.52:195–200.

Humphrey JD, Eberth JF, Dye WW, Gleason RL (2009) Fundamental role of axial stress in compensatory adaptations by arteries. *J. Biomech.* 42(1):1–8.

Hu Y, Xu Q (2011) Adventitial biology: Differentiation and function. *Arterioscler. Thromb. Vasc. Biol.* 31(7):1523–1529.

Ito H (1989) “Vascular Connective Tissue Changes in Hypertension,” *Blood Vessel Changes in Hypertension: Structure and Function Vol. I*, R. M. K. W. Lee, ed., CRC Press, Boca Raton, Florida, pp. 99–122.

Junqueira LC, Carneiro J (2005) *Basic histology: text and atlas*. 11th edn. McGraw Hill, pp. 206 – 7.

Matsumoto T, Hayashi K (1994) Mechanical and dimensional adaptation of rat Aorta to hypertension. *ASME. J. Biomech. Eng.* 116:278–283.

Matsumoto T, Hayashi K (1996) Stress and strain distribution in hypertensive and normotensive rat aorta considering residual strain. *ASME. J. Biomech. Eng.* 118:62–73.

Matsumoto T, Okumura E, Miura Y, Sato M (1999) Effect of smooth muscle cells on the mechanical response of rabbit carotid arteries in culture. *JSME. Int. J. C-Mech. Sy.* 42:514–520.

Matsumoto T, Goto T, Furukawa T, Sato M (2004) Residual stress and strain in the lamellar unit of the porcine aorta: experiment and analysis. *J. Biomech.* 37:807–815.

Matsumoto T, Fukunaga A, Narita K, Nagayama K (2008) Microscopic mechanical analysis of aortic wall: estimation of stress in the intramural elastic laminae and smooth muscle cells in a physiological state. In: *Proceedings of 2008 Summer Bioengineering Conference (CD-ROM)*, 192450.pdf.

Matsumoto T, Yamamoto M, Seo S, Sato J, Kato Y, Sato M (2011) Effects of Hypertension on Morphological, Contractile and Mechanical Properties of Rat Aortic Smooth Muscle Cells. *Cell. Mol. Bioeng.* 4-3: 340–347.

Matsumoto T, Nagayama K (2012) Tensile properties of vascular smooth muscle cells: Bridging vascular and cellular biomechanics. *J. Biomech.* 45(5):745–755.

Michael HR, Wojciech P (2011) *Histology, A Text and Atlas*, 6th Edition, Wolters Kluwer/Lippincott Williams & Wilkins Health

Michel JB, Thaumat O, Houard X, Meilhac O, Caligiuri G, Nicoletti A (2007) Topological determinants and consequences of adventitial responses to arterial wall injury. *Arterioscler. Thromb. Vasc. Biol.* 27(6):1259–1268.

Nagayama K, Yahiro Y, Matsumoto T (2011) Stress fibers stabilize the position of intranuclear DNA through mechanical connection with the nucleus in vascular smooth muscle cells. *FEBS Letters* 585(24):3992–3997.

O’Callaghan CJ, Williams B (2000) Mechanical strain-induced extracellular matrix production by human vascular smooth muscle cells role of TGF- β 1. *Hypertension* 36:319–324.

Ohlstein EH, Douglas SA (1993) Endothelin-1 Modulates Vascular Smooth Muscle Structure and Vasomotion: Implications in Cardiovascular Pathology. *Drug Dev. Res.* 29(2):108–128.

Owens GK, Schwartz SM (1983) Vascular smooth muscle cell hypertrophy and hyperploidy in the Goldblatt hypertensive rat. *Circ. Res.* 53:491–501.

Owens GK (1989) Control of hypertrophic versus hyperplastic growth of vascular smooth muscle cells. *Am. J. Physiol. Heart Circ. Physiol.* 257(6):1755–1765.

Saarikangas J, Zhao H, Lappalainen P (2010) Regulation of the actin cytoskeleton-plasma membrane interplay by phosphoinositides. *Physiol. Rev.* 90(1):259–289.

Stanley AG, Patel H, Knight AL, Williams B (2000) Mechanical strain-induced human vascular matrix synthesis: The role of angiotensin II. *J. Renin-Angio-Aldo S.* 1:32–35.

Stenmark KR, Nozik-Grayck E, Gerasimovskaya E, Anwar A, Li M, Riddle S, Frid M (2011) The adventitia: Essential role in pulmonary vascular remodeling. *Compr. Physiol.* 1(1):141–161.

Tajik A, Zhang Y, Wei F, Sun J, Jia Q, Zhou W, Singh R, Khanna N, Belmont AS, Wang N (2016) Transcription upregulation via force-induced direct stretching of chromatin. *Nat. Mater.* 15:1287–1296.

Takamizawa K, Hayashi K, Matsuda T (1992) Isometric biaxial tension of smooth muscle in isolated cylindrical segments of rabbit arteries. *Am. J. Physiol.* 263(1):H30–H34.

Uematsu M, Ohara Y, Navas JP, Nishida I, Murphy TJ, Wayne AR, Nerem RM, Harrison DG (1995) Regulation of endothelial cell nitric oxide synthase mRNA expression by shear stress. *Am. J. Physiol., Cell Physiol.* 269(6): C1371–C1378.

Vaishnav RN, Vossoughi J, Patel DJ, Cothran LN, Coleman BR, Ison-Franklin EL (1990) Effect of hypertension on elasticity and geometry of aortic tissue from dogs. *J. Biomech. Eng.* 112:70–74.

Valdez-Jasso D, Bia D, Zócalo Y, Armentano RL, Haider MA, Olufsen MS (2011) Linear and nonlinear viscoelastic modeling of aorta and carotid pressure-area dynamics under in vivo and ex vivo conditions. *Ann. Biomed. Eng.* 39(5):1438–1456.

Wang JF (2016) A study on actin and focal adhesion dynamics focusing on adhesion process of the cell. Japan, Nagoya Institute of Technology.

Wang N, Tytell JD, Ingber DE (2009) Mechanotransduction at a distance: mechanically coupling the extracellular matrix with the nucleus. *Nat. Rev. Mol. Cell. Bio.* 10:75–82.

Wang X, Liu H, Zhu M, Cao C, Xu Z, Tsatskis Y, Lau K, Kuok C, Filletter T, McNeill H, Simmons CA, Hopyan S, Sun Y (2018) Mechanical stability of the cell nucleus – roles played by the cytoskeleton in nuclear deformation and strain recovery. *J. Cell. Sci.* 131:jcs209627.

Wiener J, Loud AV, F Giacomelli F, and Anversa P (1977) Morphometric analysis of hypertension-induced hypertrophy of rat thoracic aorta. *Am. J. Pathol.* 88:619–633.

Wolinsky H, Glagov S (1964) Structural basis for the static mechanical properties of the aortic media. *Circ. Res.* 14(5):400–413.

Wolinsky H, Glagov S (1967) A Lamellar Unit of Aortic Medial Structure and Function in Mammals. *Circ. Res.* 20(1):99–111.

Wolinsky H (1971) Effects of hypertension and its reserval on the Thoracic Aorta of the Male and Female Rats. *Circ. Res.* 28:622–637.

Wolinsky H (1972) Long-term effects of hypertension on the rat aortic wall and their relation to concurrent aging changes. *Circ. Res.* 30:301–309.

Zhang Y, Dunn ML, Drexler ES, McCowan CN, Slifka AJ, Ivy DD, Shandas R (2005) A microstructural hyperelastic model of pulmonary arteries under normo- and hypertensive conditions. *Ann. Biomed. Eng.* 33(8):1042–1052.

Zou Y, Zhang Y (2009) An experimental and theoretical study on the anisotropy of elastin network. *Ann. Biomed. Eng.* 37(8):1572–1583.

Zou Y, Zhang Y (2012) The biomechanical function of arterial elastin in solutes. *J. Biomech. Eng.* 134(7):071002.

Chapter 2 Experiment and analysis

2.1 Summary of this chapter

This research aims at exploring the nuclear anisotropic deformation against the tissue stretch in different directions. In this chapter, the details of the stretching experiment, including detailed procedures of preparing for three types of sliced specimens, staining the specimen, and performing tensile test in the circumferential and axial directions will be introduced.

The thoracic aorta was harvested from Japanese White rabbit, and they were cut into 0.2-mm-thick ring-like segments in the direction perpendicular to the aortic axial axis (for type 1 specimen), or 0.2-mm-thick strip-like segments in the direction perpendicular to the circumferential direction (for type 2 and 3 specimen). Then, the SMC and AF were stained and the tensile tests with the three types of sliced specimens were performed.

Then, the process of image analysis will be introduced. Those processed images will be used for measuring and calculating for the following: 1) the macroscopic stretch of the specimen in the horizontal and vertical directions of the image in the 2D analysis; 2) heterogeneous strain of the specimen; 3) nuclear stretch ratio in 2D and 3D view; 4) AF deformation in 2D view.

Distinct methods were used to measure the stretch ratios of the nucleus and AF in the stretched specimen because the nucleus and AF have different morphological shapes. ImageJ was employed to measure the nuclear deformation while a modified

“Image correlation method” was utilized for the AF deformation measurement.

2.2 Specimen preparation

2.2.1 Test model

All animal experiments were approved by the institutional review board for animal care at the Faculty of Engineering, Nagoya University (approval #18-8) and were performed under the Guide for Animal Experimentation, Nagoya University.

The experiment aims at observing the SMC nucleus and AF with sliced samples of the vessel tissue. To get the sliced samples, thoracic aortas were harvested from ten 17 to 19-week-old male Japanese White rabbits weighing 3.1–3.5 kg, sacrificed with an overdose of sodium pentobarbital. Fig. 2.1 concisely shows the descending thoracic aortas of Japanese White rabbit. The harvested vessels were immersed in the PBS(-) (phosphate-buffered saline without calcium and magnesium, Nissui Pharmaceutical, Japan) at 4°C. Then, the loose-connective tissues were removed from the adventitia by tweezers slightly for subsequent experimental steps. The removing process was performed in the PBS(-) and takes about 10 min–0.5 h. The descending thoracic aortas were used to slice the specimen because it has a straight cylindrical shape, which is long enough and has no large branches for the ease of handling with a micro-slicer.

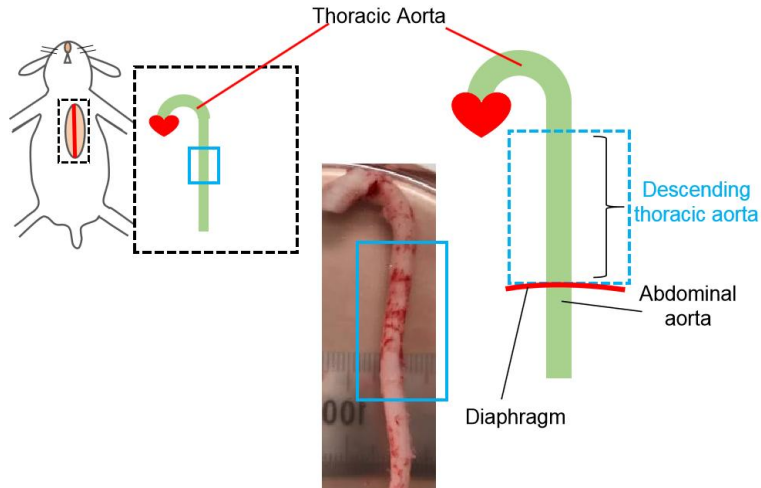


Fig. 2.1 The descending thoracic aorta of Japanese White rabbit.

2.2.2 Preparation of the aortic slice

After loose-connecting tissues were removed from the adventitia, a cotton stick was used to sweep the intima surface gently and slowly in circumferential direction to remove the endothelial cell layer. By doing this, the AF in SMCs could be stained more clearly.

The aortic samples were then embedded in an agar (Nacalai Tesque, Japan) and they were cut into 0.2-mm-thick ring-like segments in the direction perpendicular to the aortic axial axis, or 0.2-mm-thick strip-like segments in the direction perpendicular to the circumferential direction using a micro-slicer (DTK-1000, Dosaka EM, Japan).

Three types of the sliced specimen were prepared to perform tensile experiments and also to explore the anisotropic properties of SMC in the media. Three types of specimens were prepared as illustrated in Fig. 2.2. For type 1, the ring-like segments were cut into arc specimens with the size of approximately 0.3 mm in the radial

direction (wall thickness) \times 6 mm in the circumferential \times 0.2 mm in the axial direction for a circumferential stretch test and photographed in the circumferential-radial plane during stretch for 2D and 3D analyses. For type 2, the strip-like segments were cut into rectangular specimens with the size of approximately 0.2 mm in the circumferential direction \times 6 mm in the axial \times 0.3 mm in the radial direction (wall thickness). The samples were then photographed in the circumferential-axial plane during an axial stretch test for 2D analysis. For type 3, the specimens with the same dimensions to the type 2 were photographed in the radial-axial plane during the axial stretch for 3D analysis. All the cutting procedures above were finished within 3–6 h after the animal was sacrificed.

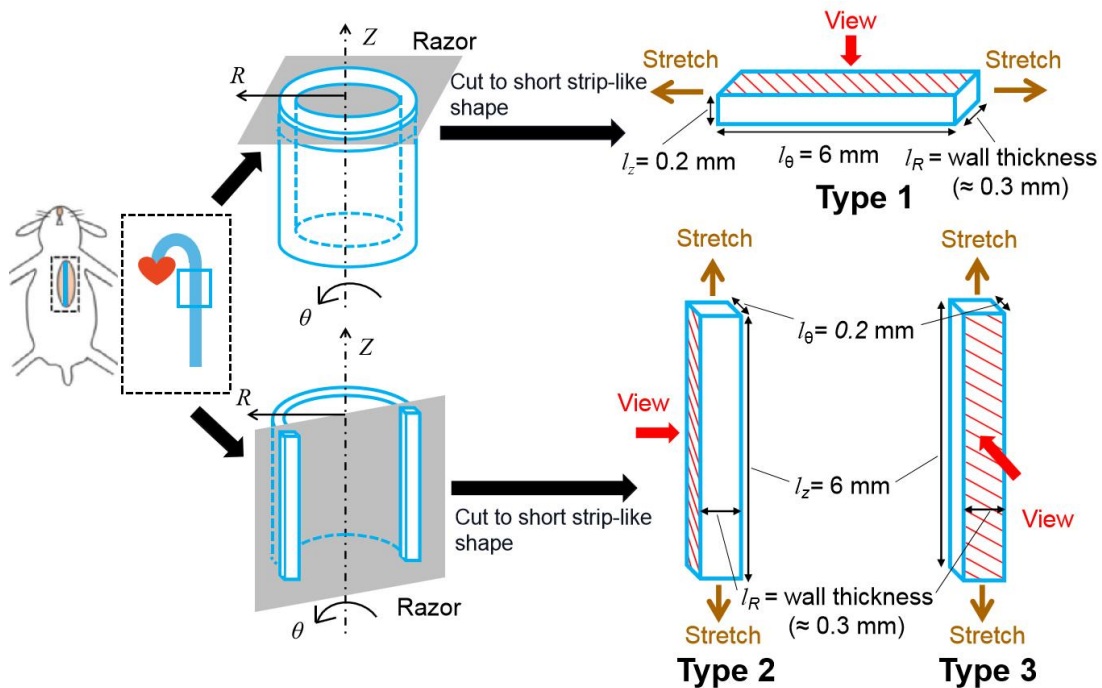


Fig. 2.2 Three types of the specimens for stretching.

2.3 Staining of the smooth muscle cell nucleus and the actin filaments

All of the three types of specimens were immersed in PBS(-) containing Hoechst 33342 (10 mg/mL, Molecular Probes, USA) at 1:500 for 1 h at room temperature to stain the nuclei. During the staining process, the sliced specimens were incubated in the shade. After incubation, the specimens were washed with PBS(-) solution 3 times for 5 minutes.

After staining the SMC nuclei, the slices were immersed in Alexa Fluor 546 phalloidin (Thermo Fisher Scientific Inc, USA) diluted in PBS(-) at 1:400 for 2–3 h on a shaker at room temperature to stain the AFs in the tissue. After that, the specimens were washed with PBS(-) solution 3 times for 5 minutes.

All the staining procedures were performed within 5 hours after trimming the tissue.

2.4 Stretch test

2.4.1 Stretch device and experimental setup

The experiment was performed on a tensile tester (STB-150W-NK, Strex, Japan) under a confocal laser scanning microscope (FV1200, Olympus, Japan) with a 100 \times oil immersion objective (NA = 1.4) at room temperature.

The tester was originally used for stretching cells on an elastic membrane and was modified to stretch thin-sliced tissue specimens. Fig. 2.3 concisely shows the diagram of the tensile tester. Both ends of the rectangular strip-like specimen were attached to two 0.1-mm-thick OHP sheets of 6 mm \times 3 mm with cyanoacrylate adhesive. The OHP sheet was attached on a pair of custom-made stainless-steel pieces with the same cyanoacrylate adhesive. Next, the pieces with the specimen were mounted to the arms of the tensile tester with silicone jigs. Finally, the tester was mounted to the microscope. On the two sides of the tensile tester, equispaced colorful tape markers were prepared for the 33 teeth in each gear to rotate the gears quantitatively. One round for one gear makes 1 mm movement in the stretch direction of the arm of the tensile tester. By counting the number of teeth being rotated, the strain was obtained.

Both ends of the specimens were attached to the arms of the tensile tester leaving about 3 mm space for observation of the deformation. An initial distance between the arms was shorter than 3 mm so that the arc specimens can be regarded as a rectangular shape. For the stretching experiment, the initial position of the specimen was determined as the no load state that should satisfy the following two conditions: First, a

clear fiducial nucleus is located in the center of the field of view, and both the nuclei and ELs can be observed clearly. Second, the wavy morphology of the ELs begins to be straightened as the gears of the tester are imposed a small rotation as shown in Fig. 2.4.

The tensile strain was then applied to the specimen with a stepwise increment (6–8%). The stepwise stretch step was repeated 5–6 times so that the sliced specimen was stretched about 1.4 times greater than the initial length. At the end of each step (including the initial no-load state), Z-stack images were obtained. The nuclei (Hoechst 33342) were visualized with 405-nm excitation and 430–470-nm emission while the F-actin (Alexa Fluor 546 phalloidin) with 543-nm excitation and 560–660 nm-emission. The $100\times$ lens (NA=1.4) was used for observing and taking photos during the test.

Three series of Z-stack images were taken at each steps; 1) a series of about 40 image slices with an interval of $0.4\ \mu\text{m}$ for SMC nucleus which was used to calculate macroscopic stretch ratio, 2) a series taken in twice magnification of about 50–90 image slices with an interval of $0.2\text{--}0.4\ \mu\text{m}$ for a nucleus with typical ellipsoid shape, in Fig. 2.5 (a), and 3) a series taken in twice magnification of about 50–90 image slices with an interval of $0.2\text{--}0.4\ \mu\text{m}$ for the surrounding AF network of that nucleus in Fig. 2.5 (b). PBS was intermittently dripped onto the specimen to prevent the dehydration during the stretch. The tensile experiment for each sample was performed for 2–3 h after staining. Four to six slices were obtained from each rabbit and the total of 29 slices were stretched successfully. The nucleus and perinuclear AFs whose images were most clearly seen in each slice were used for the analysis. The tensile

process for every slice was finished within 2 hours.

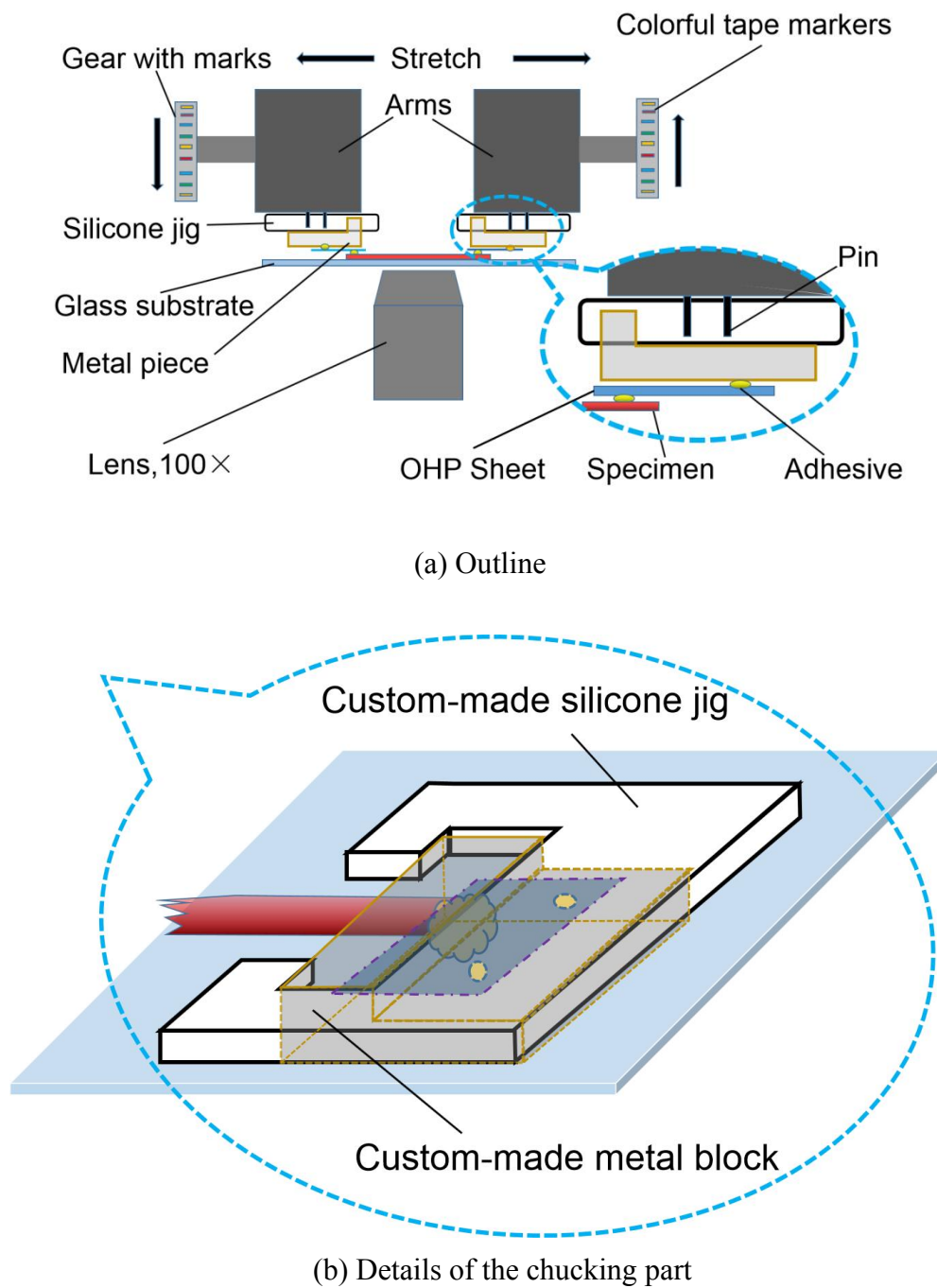


Fig. 2.3 Diagram of the tensile tester. Schematic diagram of the tensile tester on the microscope (a). The specimen was set to the custom-made jig (b).

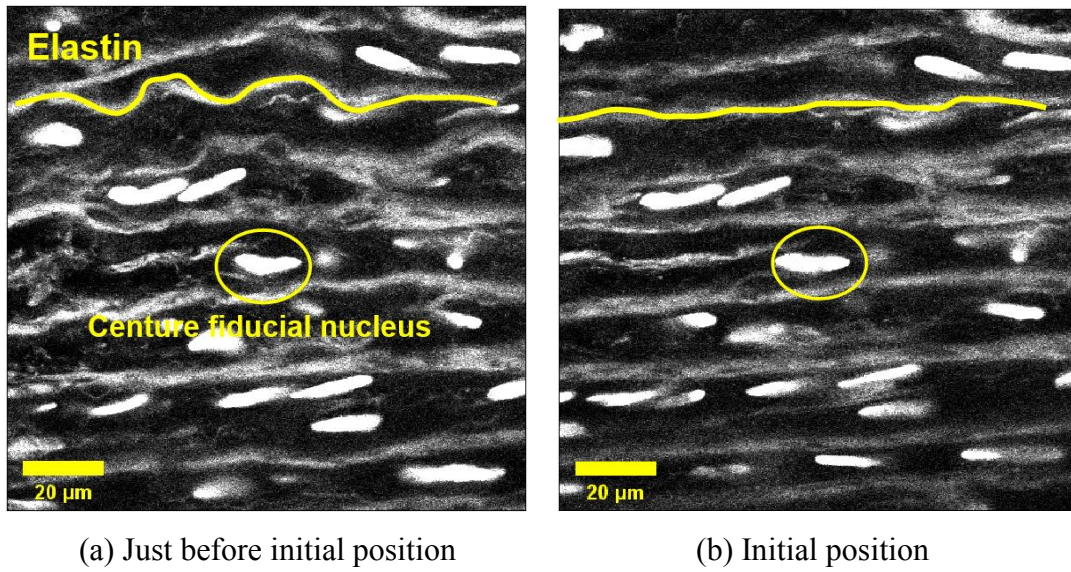


Fig. 2.4 Determination of the initial position for the stretch test.

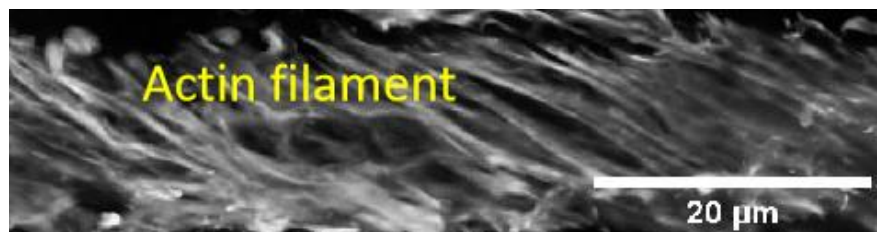


Fig. 2.5 Staining images of the twice magnification image taken at the same position.

2.4.2 Type-1 slice: Circumferential stretch for 2D and 3D analyses

The type-1 slice was stretched in the vascular circumferential direction and was observed in the circumferential-radial plane as shown in Fig. 2.6 (a). The laser of the microscope scanned the specimen in the vertical (vascular axial in the figure) direction from the bottom to the top. Fig. 2.6 (a) shows the type-1 case in which the nucleus oriented in the circumferential direction while one transverse axis of the ellipsoidal nuclei oriented in the vertical direction. A series of 70–90 stack images of the nucleus and AF were taken in the vertical direction with the interval distance of 0.2–0.3 μm , which altogether observed about 20 μm of the specimen thickness in its axial direction. The type-1 slice was stretched to 1.4 times greater to the initial length in the circumferential direction, which is close to the physiological state (Matsumoto et al. 2002). Data obtained for type-1 slices were used for 2D and 3D analyses for the deformation of the SMC and AF.

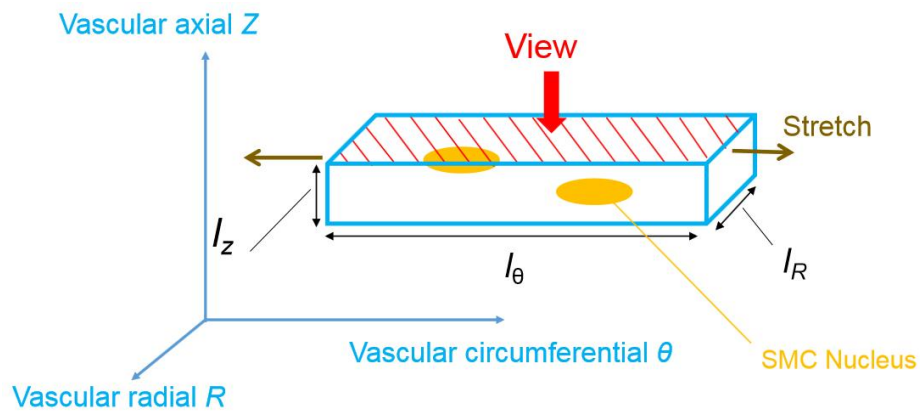
2.4.3 Type-2 slice: Axial stretch for 2D analysis

The type-2 slice was stretched in the vascular axial direction and was observed in the circumferential-axial plane as shown in Fig. 2.6 (b). Here, the nuclear transverse axis elongates, whereas its longitudinal axis contracts. Like type-1 slices, one of the ellipsoidal nuclear transverse axes oriented in the vertical direction (vascular radial in the figure), i.e., the direction of the laser irradiation. A series of 70–90 stack images of the nucleus and AF were taken in the spatial vertical direction with the interval distance of 0.2–0.3 μm , which altogether observed about 20 μm of the specimen

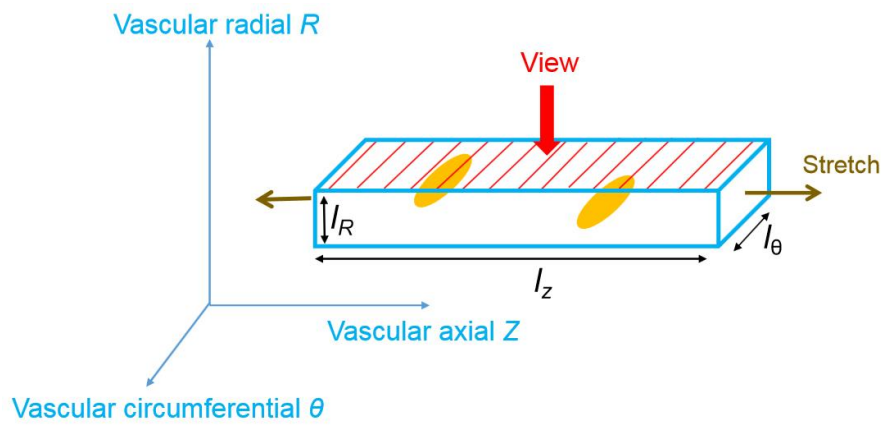
thickness in its radial direction. The type-2 slice was stretched to 1.4 times greater the initial length in the axial direction, which is close to the physiological state (Matsumoto et al. 2002). Data obtained for type-2 slices were used for 2D analyses for the deformation of the SMC and AF

2.4.4 Type-3 slice: Axial stretch for 3D analysis

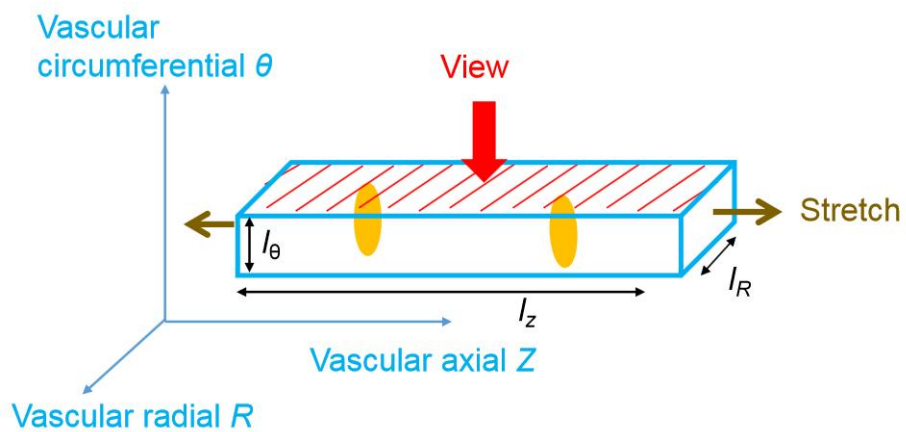
The type-3 slices were also stretched in the vascular axial direction, but they were observed in the radial-axial plane as described in Fig. 2.6 (c). This type of slice was used to evaluate the 3D motion of the nucleus, i.e., whether the nucleus will rotate from an “upright” posture when the stretching in the axial direction was applied. For this type of specimen, a series of 50–70 stack images of the nucleus were taken in the spatial vertical direction with the interval distance of 0.3–0.4 μm because the nucleus in this case oriented with its longitudinal axis in the vertical direction which might take longer time to take the photos. Hence, fewer images were taken compared to type-1 and 2 slices, but the interval distance was set larger to ensure that about 20 μm of the specimen thickness was observed in its circumferential direction.



(a) Type 1 slice



(b) Type 2 slice



(c) Type 3 slice

Fig. 2.6 Three types of specimen used in the tensile test.

2.5 Image processing

2.5.1 Image processing in 2D

The images obtained from 8 slices in the circumferential stretch and 5 slices in the axial stretch were stacked and used for the 2D analysis. All the images taken during the experiment were processed for deconvolution with cellSens (ver.1.18, Olympus, Japan) 10 times to reduce the noise. Then, the 40 image stacks of the nucleus taken at each step of the tensile test were projected onto a single image with a ‘standard deviation intensity’ of ImageJ (Fiji, version 1.53g, NIH, USA), as described in Fig. 2.7. The standard deviation intensity was used to make a projected image because for black and white images, this projected method makes an image relatively closer to its real state without too high/low saturation.

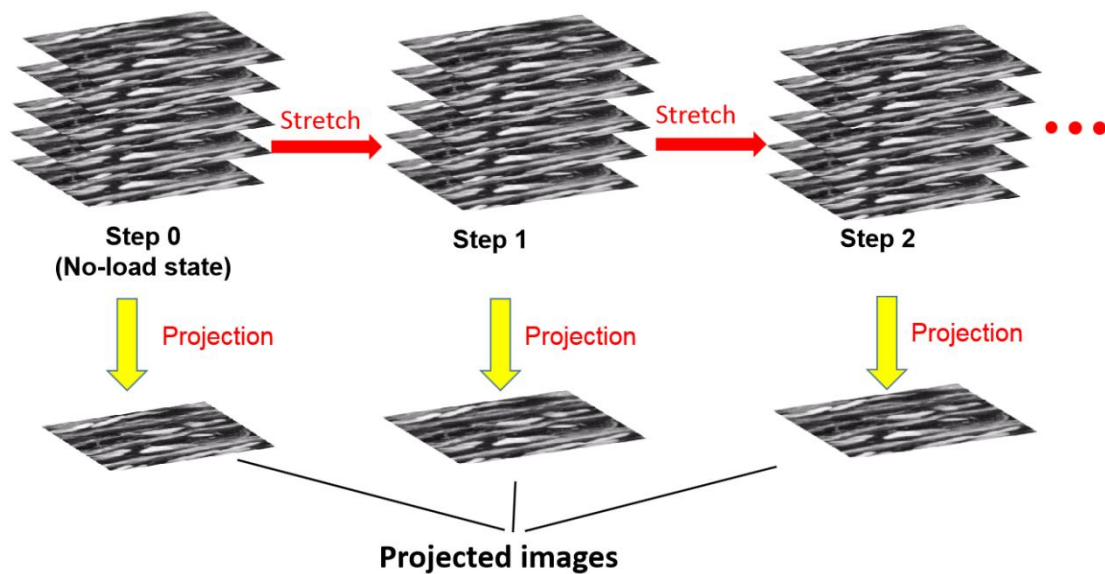


Fig. 2.7 Projection of the stack images for every stretch step.

2.5.2 Image processing in 3D

To evaluate the orientation and rotation of the nuclei three-dimensionally, the 3D nuclei were reconstructed with an image processing software Imaris (Version 9, Bitplane, Switzerland) from the 2D stack images of type-1 and type-3 specimens. As the same laser intensity condition was kept for every step so that the 3D nucleus body was reconstructed through the Imaris automatically.

2.6 Deformation analysis

2.6.1 Macroscopic deformation of the specimen

Macroscopic stretch ratio of the tissue in the stretch direction (horizontal direction in the images) was calculated by selecting three pairs of characteristic points in the image of the initial position as fiducial markers. Fig. 2.8 (a) shows the process of calculating the macroscopic stretch ratio in horizontal (stretch) direction. One point in a pair located near the left edge and the other located near the right edge of the images, and the positions of each pair perpendicular to the stretch direction were set to become almost equal. The distance between each pair was then measured at each step. The macroscopic stretch ratio between two stretch steps was calculated for the stretch direction as:

$$\Lambda_x(i-1, i) = \frac{1}{3} \cdot \sum_{p=1}^3 \left(\frac{l_p(i)}{l_p(i-1)} \right), \quad (2.1)$$

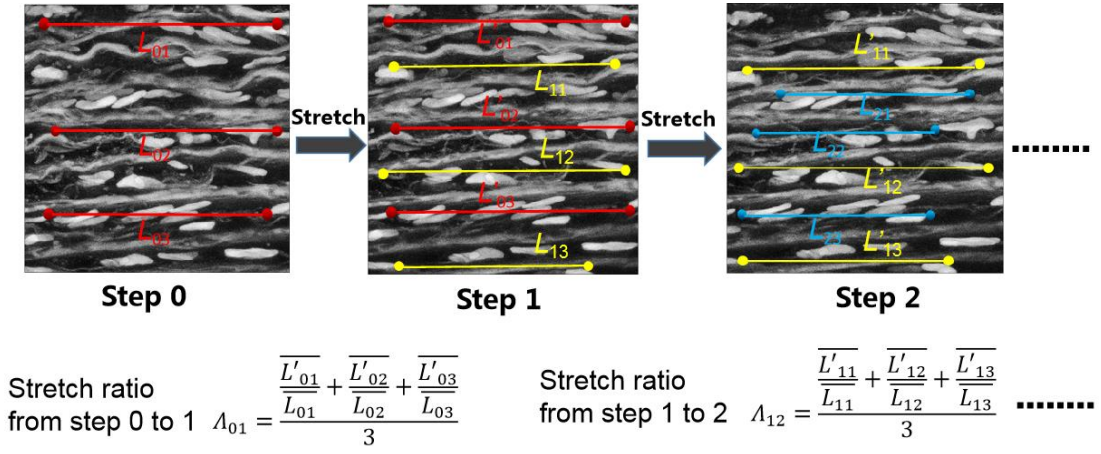
where $\Lambda_x(i-1, i)$ is the stretch ratio between stretch steps $i-1$ and i , and $l_p(i)$ is the distance between pair p in step i . The macroscopic stretch ratio of the tissue at the n -th

stretch step from the initial position was calculated as:

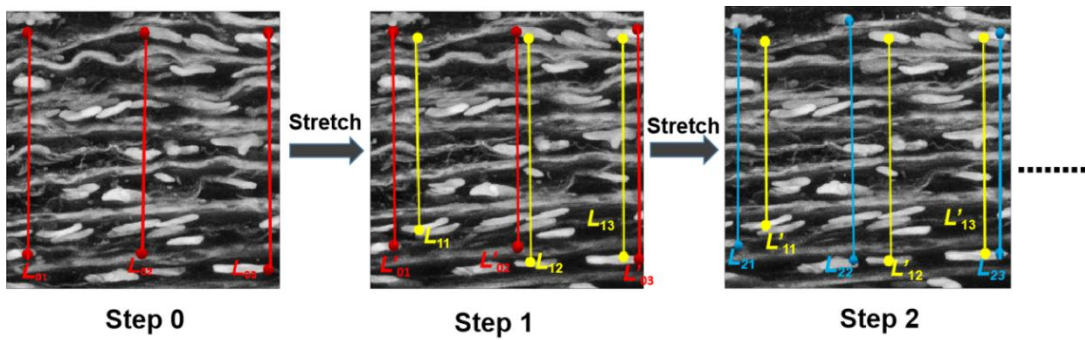
$$\Lambda_x(n) = \prod_{i=1}^n \Lambda_x(i-1, i), \quad (2.2)$$

where $\Lambda_x(n)$ is the macroscopic stretch ratio of the specimen at step n .

The macroscopic stretch ratio of the tissue in the direction perpendicular to the stretch direction (vertical direction in the images) $\Lambda_y(n)$ was also calculated with a similar method by choosing pairs of points near the top and bottom edges of the images and measuring their interval changes, as shown in Fig. 2.8 (b).



(a) Macroscopic stretch ratio parallel to the stretch direction



(b) Macroscopic stretch ratio perpendicular to the stretch direction

Fig. 2.8 Calculation of macroscopic stretch ratios of the specimen in the stretch direction (a) and in the direction perpendicular to the stretch direction (b) for the first three steps in the test.

2.6.2 Heterogeneous deformation of the media

For the images obtained from the tensile test in the circumferential direction, the SMLs in the images were selected according to the morphology of the ELs and they were numbered (Fig. 2.9). Similarly, a pair of characteristic points or the centroids of two nuclei with almost equal radial position on the left and right sides was chosen in each SML. The change in the circumferential distance between these two points was measured to obtain the stretch ratio in each SML as

$$\lambda_{mn} = \prod_{i=1}^n \frac{L_{m_i}}{L_{m_{i-1}}} , \quad (2.3)$$

where λ_{mn} indicates the stretch ratio of the SML m at the n th strain step, i the stretch step, and L the distance between the two chosen points in each SML.

For calculating the shear deformation between two SMLs, the coordinates of the central point between the two side points in each SML selected as described above were calculated first. Subsequently, the below equation was obtained:

$$\tau_{(m)(m+1)} = \frac{|\bar{X}_{(m+1)i+1} - \bar{X}_{(m+1)i}| - |\bar{X}_{m_{i+1}} - \bar{X}_{m_i}|}{d_{(m+1)i} - d_{m_i}}, \quad (2.4)$$

where $\tau_{(m)(m+1)}$ is the shear deformation between the SML m and $m+1$; d_{m_i} and $d_{(m+1)i}$ are the radial coordinates of the central point of SML m and $m+1$, respectively; \bar{X} is the mean value of the two chosen points in each SML.

For calculating the local Green strain, triangles were set in the image of the initial position. Then the three vertices of every small triangle were traced in every stretch step. Fig. 2.10 (a) and (b) show a case of these small triangles used for calculating the strain before and after stretch, respectively. By doing that, each line of the triangles is always connected to the same characteristic points in the images obtained under tensile

strain. The local Green strain relative to the initial step 0 was calculated as

$$ds'^2_{(1,2,3)} - ds^2_{(1,2,3)} = \sum_{j=2}^2 \sum_{k=1}^2 2E_{jk} \cdot da_j \cdot da_k \quad (2.5)$$

where ds'^2 is the line length of the triangle at the present strain step, ds^2 the line length at the initial step, E_{11} the local Green strain along the circumferential direction, E_{22} the local Green strain along the radial direction, and E_{12} ($=E_{21}$) the shear strain. Further, da_j and da_k are the components of ds in the circumferential and radial directions, respectively. The calculation was performed using a custom-made MATLAB code (Appendix 1) (Ver. 2016a, Mathworks, USA).

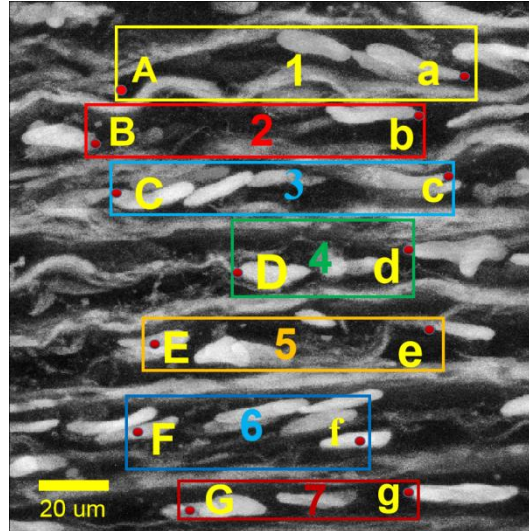


Fig. 2.9 Example of fluorescent image of a specimen in the circumferential stretch case. Capital letters (A – G) indicate the corresponding boundary points with different colors.

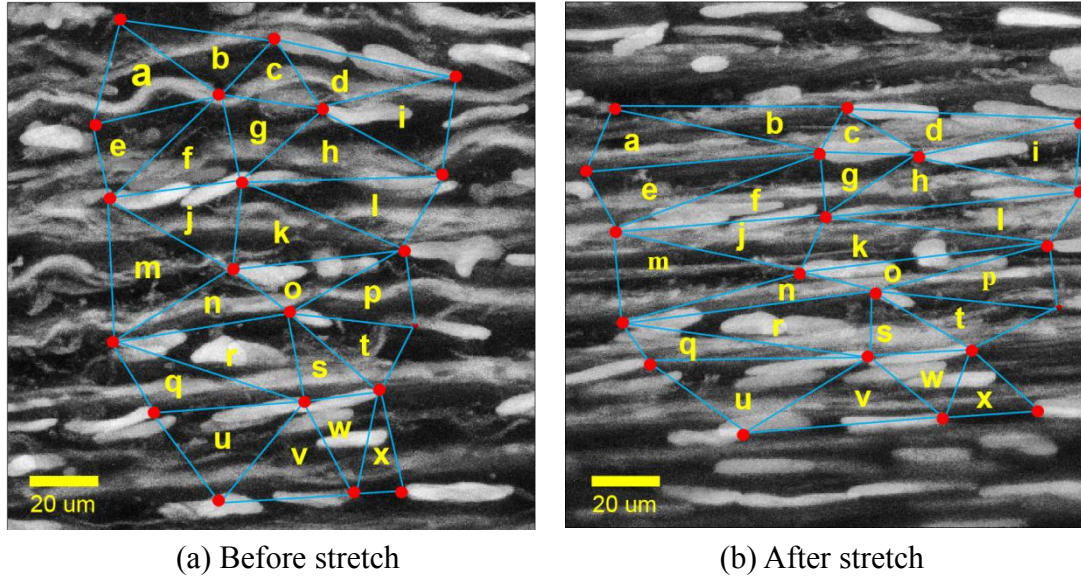


Fig. 2.10 A case showing the small triangles used for calculating the Green strain. A type-1 specimen. Red points indicate the vertex of the triangles with blue lines while the triangles are marked with small letters.

2.6.3 Microscopic deformation of the nucleus in 2D

All the 50–80 image stacks of the nucleus taken during the tensile test were projected onto a single image as in the previous section. Deformation of the nucleus in response to the stretch was evaluated by calculating changes in the lengths of its longitudinal and transverse axes as well as its rotation angle. In each stretch step i , the nuclear outlines were manually depicted by a ‘Freehand Selections’ tool in ImageJ. Then, each outline was fitted to an ellipse to measure its length of the longitudinal axis $l_N(i)$, area $A_N(i)$, and oriented angle $\theta_N(i)$ to the horizontal direction. The longitudinal axis length $l_N(i)$ was termed as nuclear length. According to the previous study, the length of the transverse axis of the nucleus (nuclear width), $w_N(i)$, was obtained as:

$$w_N(i) = \frac{A_N(i)}{l_N(i)}. \quad (2.6)$$

The stretch ratio of the nuclear length in step i was calculated as:

$$\Lambda_{\text{Nl}}(i) = \frac{l_N(i)}{l_N(0)}, \quad (2.7)$$

where $l_N(0)$ and $l_N(i)$ are the nuclear lengths in step 0 and i , respectively. The stretch ratio of the nuclear width in step i was calculated as:

$$\Lambda_{\text{Nt}}(i) = \frac{w_N(i)}{w_N(0)}, \quad (2.8)$$

where $w_N(0)$ and $w_N(i)$ are the nuclear widths in step 0 and i , respectively.

The rotation of the nuclear major axis from the initial state to step i was measured and indicated as $\Delta\theta_N(i)$.

$$\Delta\theta_N(i) = \theta_N(0) - \theta_N(i), \quad (2.9)$$

where $\theta_N(0)$ is the initial oriented angle of the nucleus, and $\theta_N(i)$ is the oriented angle at stretch step i . Fig. 2.11 (a) shows the longitudinal axis, transverse axis and the oriented angles of the nucleus fitted to ellipsoid for a type-1 slice. Fig. 2.11 (b) shows those parameters for a type-2 slice.

For comparison, the stretch ratios and the change in the orientation angles were calculated from the macroscopic stretch ratios obtained in Section 2.6.1 assuming homogeneous deformation of the tissue. The horizontal and the vertical macroscopic stretch ratios from stretch step i to $i+1$ were calculated and denoted as $\Lambda_x(i, i+1)$ and $\Lambda_y(i, i+1)$, respectively as shown in Eq. 2.1 for Λ_x . For the nucleus deformation, the nucleus was stretched from step i to $i+1$ in a homogeneous body as shown in Fig. 2.12, its orientation angles at step $i+1$ was marked with $\theta_N^h(i+1)$ and calculated as:

$$\tan \theta_N^h(i+1) = \frac{l_N(i) \cdot \sin \theta_N^h(i) \cdot \Lambda_y(i, i+1)}{l_N(i) \cdot \cos \theta_N^h(i) \cdot \Lambda_x(i, i+1)} = \tan \theta_N^h(i) \cdot \frac{\Lambda_y(i, i+1)}{\Lambda_x(i, i+1)}, \quad (2.10)$$

where $\theta_N^h(i)$ represents the hypothetical oriented angles in step i , and $\theta_N^h(0) = \theta_N(0)$.

The hypothetical length was calculated as:

$$l_N^h(i+1) = \sqrt{[l_N^h(i) \cdot \cos \theta_N^h(i) \cdot \Lambda_x(i, i+1)]^2 + [l_N^h(i) \cdot \sin \theta_N^h(i) \cdot \Lambda_y(i, i+1)]^2}, \quad (2.11)$$

where $l_N^h(i)$ and $l_N^h(i+1)$ represent the hypothetical length of the nucleus in step i and $i+1$, respectively, and $l_N^h(0) = l_N(0)$.

The hypothetical stretch ratio of the nuclear length in a homogeneous tissue from step i to $i+1$, $\Lambda_{Nl}^h(i, i+1)$ was calculated as:

$$\Lambda_{Nl}^h(i, i+1) = \frac{l_N^h(i+1)}{l_N^h(i)} = \sqrt{[\cos \theta_N^h(i) \cdot \Lambda_x(i, i+1)]^2 + [\sin \theta_N^h(i) \cdot \Lambda_y(i, i+1)]^2} \quad (2.12)$$

Thus, the hypothetical stretch ratio of the nuclear length at the n -th stretch step from the initial position $\Lambda_{Nl}^h(n)$ was calculated as:

$$\Lambda_{Nl}^h(n) = \prod_{i=0}^n \Lambda_{Nl}^h(i, i+1). \quad (2.13)$$

Similarly, the hypothetical width of the nucleus was calculated as:

$$w_N^h(i+1) = \sqrt{[w_N^h(i) \cdot \sin \theta_N^h(i) \cdot \Lambda_x(i, i+1)]^2 + [w_N^h(i) \cdot \cos \theta_N^h(i) \cdot \Lambda_y(i, i+1)]^2}, \quad (2.14)$$

where $w_N^h(i)$ and $w_N^h(i+1)$ represent the hypothetical widths of the nucleus in step i and $i+1$, respectively, and $w_N^h(0) = w_N(0)$.

The hypothetical stretch ratio of the nuclear width from i to $i+1$ steps, $\Lambda_{Nt}^h(i, i+1)$, was calculated as:

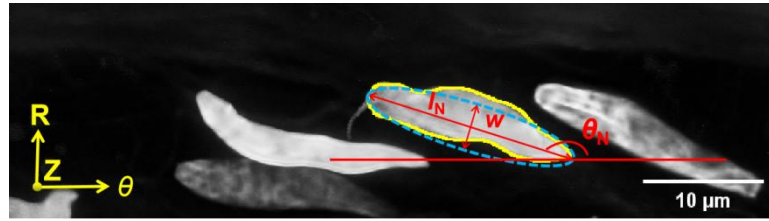
$$\Lambda_{Nt}^h(i, i+1) = \frac{w_N^h(i+1)}{w_N^h(i)} = \sqrt{[\sin \theta_N^h(i) \cdot \Lambda_x(i, i+1)]^2 + [\cos \theta_N^h(i) \cdot \Lambda_y(i, i+1)]^2}, \quad (2.15)$$

and the hypothetical stretch ratio of the nuclear width at the n -th stretch step from the initial position $\Lambda_{Nt}^h(n)$ was calculated as:

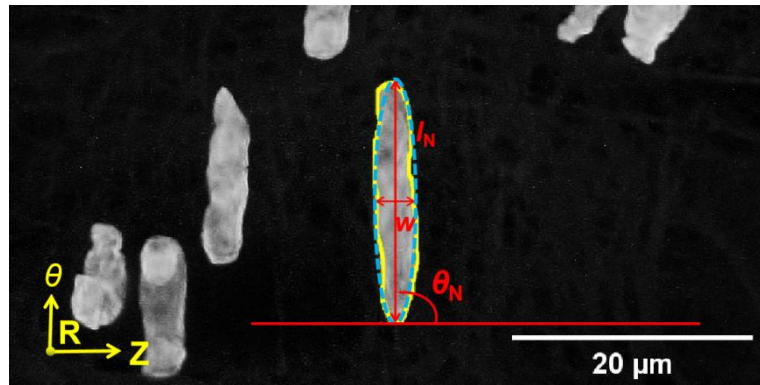
$$\Lambda_{Nt}^h(n) = \prod_{i=0}^n \Lambda_{Nt}^h(i, i+1). \quad (2.16)$$

Eqs. 2.10-2.16 were utilized to calculate the hypothetical deformations of all the

nuclei in the circumferential and axial stretch cases.



(a) Type 1 slice



(b) Type 2 slice

Fig. 2.11 Some parameters used for measurement of the ellipsoid-fitted nuclei (blue dash lines) for a type-1 slice (a) and a type-2 slice (b). l_N , Longitudinal axis; w , transverse axis of the ellipsoid-fitted nucleus; θ_N , Nuclear oriented angle.

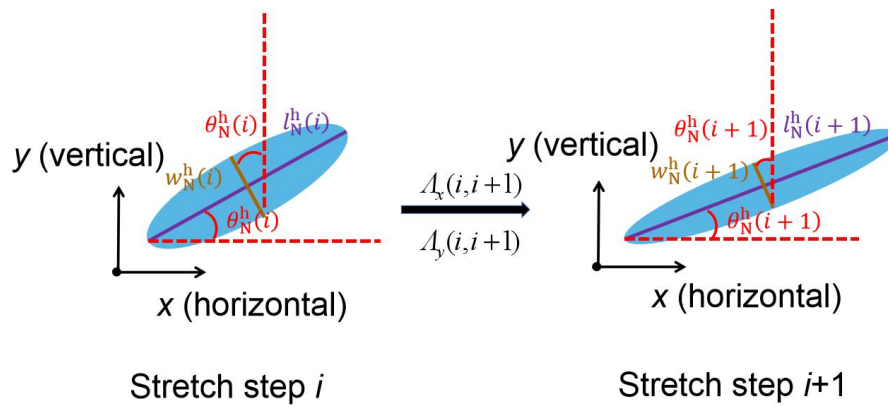


Fig. 2.12 Two-dimensional homogeneous deformation of the nucleus stretched from step i to $i+1$.

2.6.4 Microscopic deformation of the nucleus in 3D

To evaluate the orientation and rotation of the nuclei three-dimensionally, the 3D nuclei were reconstructed with an image processing software Imaris (Version 9, Bitplane, Switzerland) from their 2D stack images. The 3D nucleus body was reconstructed through the Imaris automatically. The reconstructed 3D nuclei were fitted with ellipsoids to obtain the lengths of their three axes a, b, c ($a < b < c$), as well as their three vector components projected in the Cartesian coordinates, i.e., direction cosines. The lengths of the three axes were calculated for each step i and denoted as $M(i)$ ($M = a, b$, or c). The stretch ratios of the ellipsoid axes in stretch step i were thus calculated as:

$$\lambda_M(i) = \frac{M(i)}{M(0)}. \quad (2.17)$$

The orientation angles of the nuclei were described as the angles of the nuclear longitudinal axis C to the three axes of Cartesian coordinate corresponding to the aortic circumferential, radial, and axial direction. The angles between the longitudinal axis C and the circumferential, axial, and radial directions of the aorta were marked as $\varphi_{C\theta}$, φ_{CZ} , and φ_{CR} , respectively. They were calculated through the direction cosine by using the three vector components of the C axis projected in the Cartesian coordinates. Fig. 2.13 shows a case of the 3D model of a nucleus.

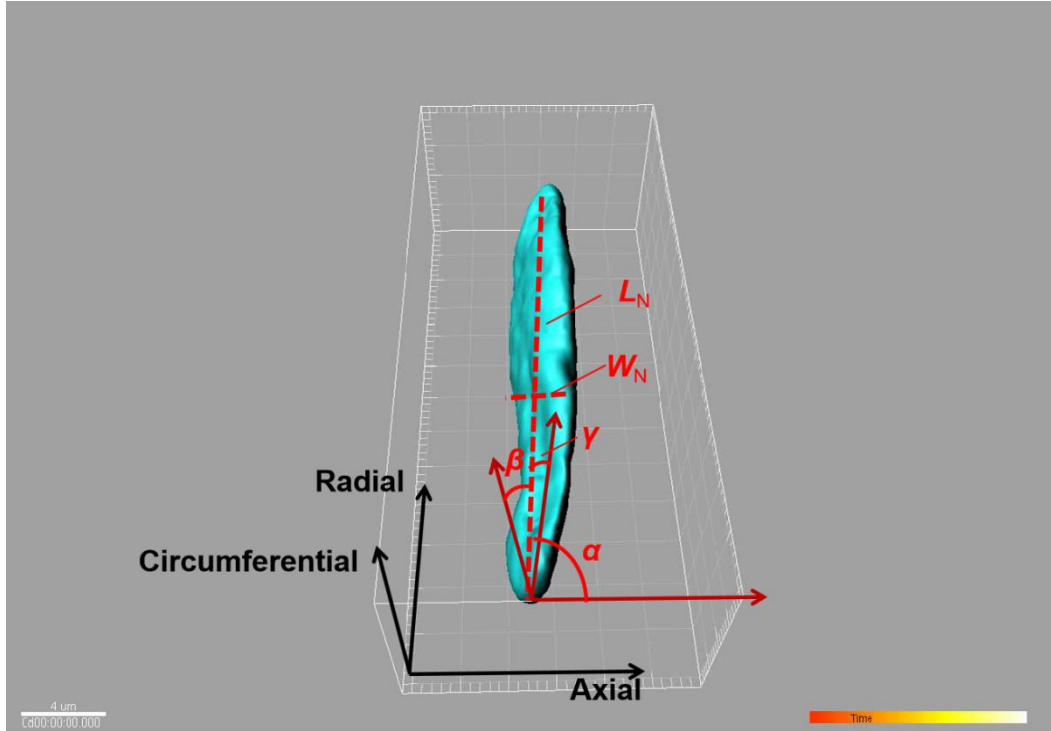


Fig. 2.13 Three-dimensional reconstructed nucleus and its longitudinal axis (L_N), transversal axis axis (W_N). The angles between its longitudinal axis and the three axes of the Cartesian coordinate of the aortic wall are marked with α , β , and γ , respectively.

2.6.5 Microscopic deformation of actin filament network in 2D

As the AF has a much more complex structure than the nucleus, its deformation cannot be calculated in the same way as the nucleus. The image correlation method (Pan et al. 2009; Zhao et al. 2012) was modified to calculate the stretch ratios of the AF network around each nucleus. For the deformation analysis, the AF network in a rectangular area of $l_N \times 3w_N$ was used in the step 0 image, where l_N and w_N are the length and width of the hypothetical ellipsoid nucleus obtained in the previous section 2.6.3, respectively. Then, the stretch ratios in the filament orientation direction and in the direction perpendicular to it between every two stretch steps i and $i+1$ were

calculated, and they were denoted as $\lambda_{Al}(i, i+1)$ and $\lambda_{At}(i, i+1)$, respectively.

Here is an example showing the processing methods for the AF network images. Fig. 2.14 shows the nucleus and the AF network in the first stretch step numbered 0–1. The periphery of the nucleus was identified manually by using a ‘Freehand Selection’ tool in Image J as shown in yellow in Fig. 2.14 (a), then it was automatically fitted to an ellipse as shown in dashed blue line to obtain the length of the fitted ellipse L . A rectangular frame with the size of $2L_N \times L_N$ where the nucleus is located centrally for each of the AF images was drawn as shown in Fig. 2.14(b)–(c). The mean oriented direction of the AF network in each rectangular frame was measured with the Image J through the 2D FFT method automatically and then marked with $\theta_A(i)$ where i is the step number.

Deformation of the AF images from stretch step 0 to 1 was characterized with the stretch ratio in the direction of AF orientation $\lambda_{Al}(0,1)$ and that in the direction perpendicular to it $\lambda_{At}(0,1)$ as the following steps:

1. The AF images in each stretch step were rotated by $\theta_A(i)$ so that the mean direction of the AF orientation within the rectangular frame corresponds to the horizontal axis (Fig. 2.14(d)).
2. The length and width of the ellipsoid fitted to the nucleus were denoted as l_N and w_N , respectively. The length l_N was measured automatically and w_N was obtained as follows:

$$w_N = \frac{A_N}{l_N} , \quad (2.18)$$

where A_N is the area of the ellipsoid.

The area of the AF network surrounding the nucleus was defined as a rectangular region of $l_N \times 3w_N$ with the nucleus at its center in the step 0 image (red frame in Fig. 2.14(e)). This smaller frame was used as the region of interest (ROI) for calculation. The size of the rectangular region was defined freely, and the difference in the mean orientation angle of the AF in the different rectangular regions was smaller than 1° , which can be neglected.

3. To calculate the stretch ratio in the ROI from Step 0 to 1, the area with the size of ROI in Step 1 image that corresponds to the ROI in the Step 0 image (termed as matched region, MR) was defined. To do this, the region of search (ROS) was defined, and it is shown in red in Fig. 2.14(f). The ROS in the Step 1 image was drawn to involve the ROI in the Step 0 image.

4. The MR was identified in ROS with Matlab (Ver.12, MathWorks, USA) using an image correlation method. Process to define the ROI, ROS, and MR was described in Fig. 2.15.

5. Fig. 2.16 describes the process to obtain the stretch ratios λ_x and λ_y between the two stretch steps. As the AF network extends along its orientation direction and shrinks perpendicular to the orientation during the tensile test in the circumferential direction, the ROI image was extended by λ_x in the horizontal direction, *i.e.*, the direction of AF orientation, and compressed it by λ_y in the direction perpendicular to AF orientation to find the best combination of extension and compression to fit in the MR. The size of the ROI was changed by 0.5% from 100% to 120% in the extension direction and from 100% to 80% in the compression direction independently and repeatedly to get

resized images of ROI (one case shown in Fig. 2.16, Process 2).

6. For each resized image of ROI, its central part with the same horizontal length as the MR (Process 3) was cut out. Then the central part of the MR with the same vertical length as the resized ROI (Process 3) was also cut out. Thus, two central parts with the same size from the resized ROI and MR were obtained. Then the image correlation coefficient r between these two central parts (Process 4) was calculated. These processes were repeated to find the combination of λ_x and λ_y that maximizes r (Process 5). Thus obtained λ_x and λ_y were used as the stretch ratios of the AF network in the fiber direction $\lambda_{Af}(0,1)$ and in the direction perpendicular to the fiber $\lambda_{Af}(0,1)$, respectively, from stretch step 0 to 1.

7. After repeating procedures 1–6 by increasing the step number, the stretch ratios between every two stretch steps of the AF network were obtained to the circumferential stretch.

8. For the slices stretched in the axial direction, the similar methods were used as the circumferential stretch case shown above in 1–4 and eventually a MR image of the AF from step i to $i+1$ was obtained as shown in Fig. 2.17. By using the similar resize methods to the circumferential stretch case to resize the ROI images, it was compared to MR images by calculating the image correlation coefficient r . Eventually, the extension and compression values were obtained, and they were used as the stretch ratios of the AF network in the direction perpendicular to the fiber λ_{Af} and in the fiber direction λ_{Af} , respectively. The ROI region for axial stretch case is also defined freely.

By performing procedures 1–8, the stepwise stretch ratio of the AF against both

circumferential and axial stretch cases were gotten. Next, the stretch ratio from step 0 to i was calculated. For both stretch cases, the stretch ratios of the AF network in the filament orientation direction $\lambda_{Al}(i)$ and in the direction perpendicular to it $\lambda_{At}(i)$ from step 0 to i were calculated as follows:

$$\lambda_{Al}(i) = \prod_{j=0}^i \lambda_{Al}(j-1, j), \quad (2.19)$$

$$\lambda_{At}(i) = \prod_{j=0}^i \lambda_{At}(j-1, j). \quad (2.20)$$

Orientation of AF network was characterized by the mean network orientation angle θ_A , which is calculated automatically from the twice magnified actin images with ImageJ using the 2D FFT method. Change in the orientation angle of the AF network was obtained as:

$$\Delta\theta_A(i) = \theta_A(0) - \theta_A(i), \quad (2.21)$$

where $\theta_A(0)$ and $\theta_A(i)$ represent the network orientation angle in steps 0 and i .

Then, the hypothetical deformations of the AF network assuming homogeneous deformation of the wall were calculated. The hypothetical stretch ratios of the AF network in its oriented direction and in the direction perpendicular to its orientation were denoted as $\lambda_{Al}^h(n)$ and $\lambda_{At}^h(n)$, respectively. They were calculated as:

$$\lambda_{Al}^h(n) = \prod_{i=0}^n \lambda_{Al}^h(i, i+1), \quad (2.22)$$

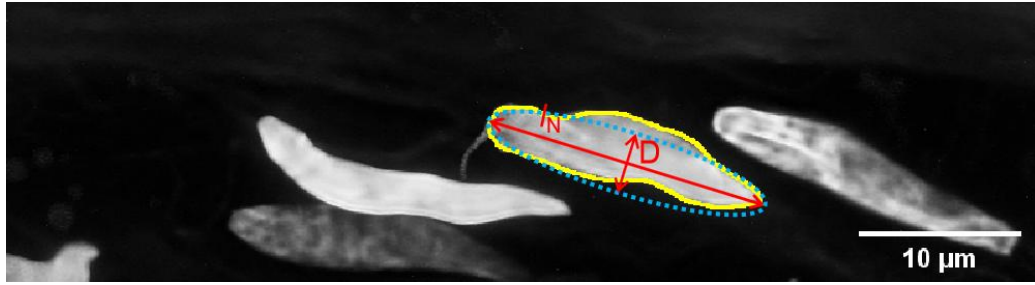
and

$$\lambda_{At}^h(n) = \prod_{i=0}^n \lambda_{At}^h(i, i+1), \quad (2.23)$$

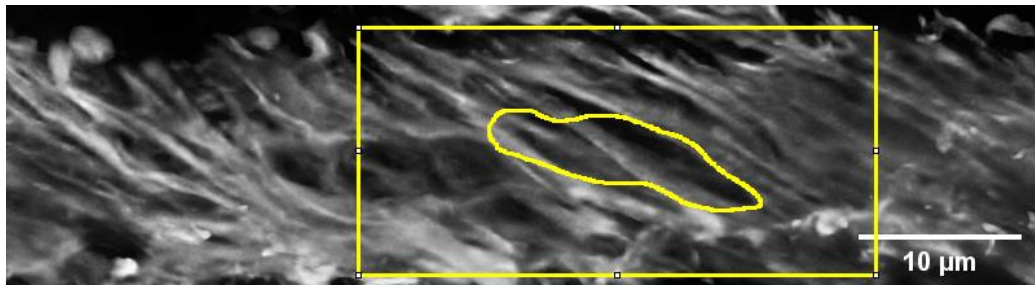
where $\lambda_{Al}^h(i, i+1)$ and $\lambda_{At}^h(i, i+1)$ represent the stepwise stretch ratio of the AF in the oriented direction and the direction perpendicular to its orientation respectively.

$\lambda_{Al}^h(i, i+1)$ and $\lambda_{At}^h(i, i+1)$ were calculated by substituting hypothetical nuclear

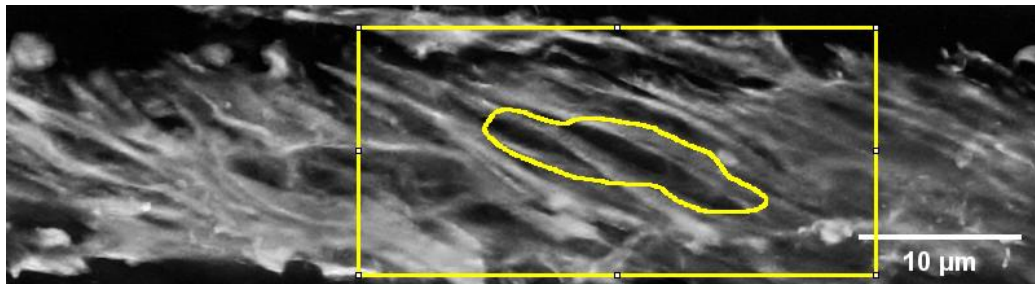
orientation angle $\theta_N^h(i)$ with hypothetical AF orientation angle $\theta_A^h(i)$ in the Eqs. 2.12 and 2.15, respectively. The $\theta_A^h(i)$ was calculated from Eq. 2.10, and $\theta_A^h(0) = \theta_A(0)$ referring to the step 0 image.



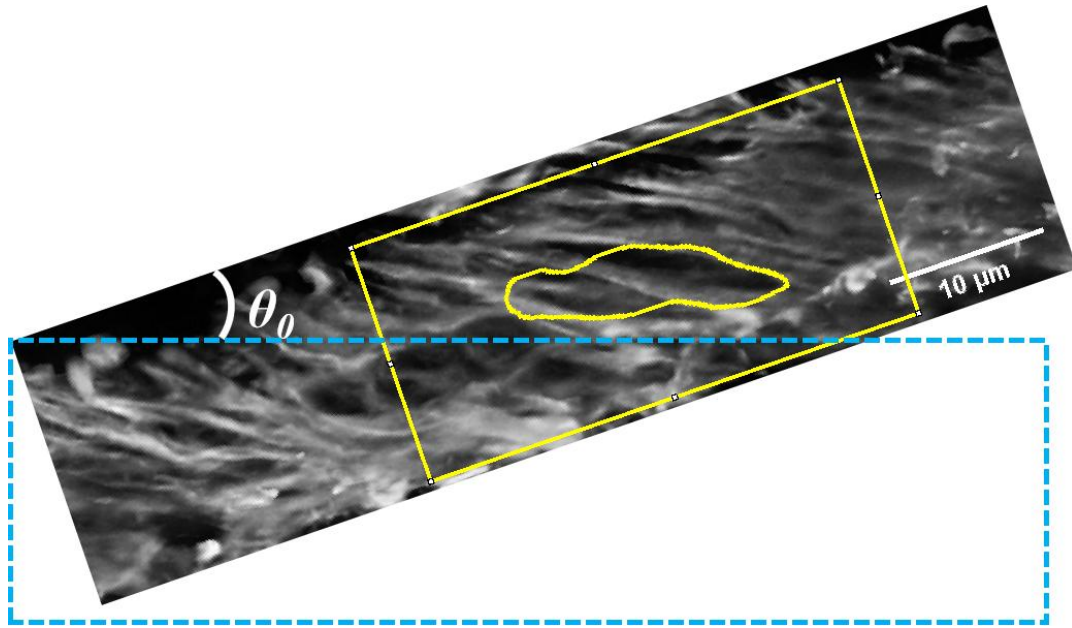
(a) Nuclei at Step 0 (no load)



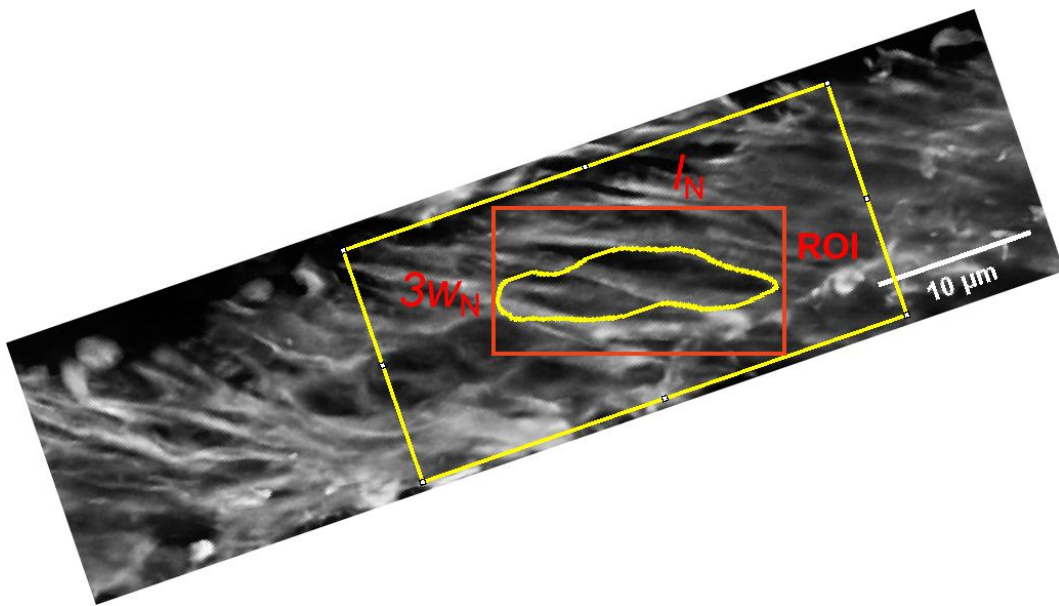
(b) Actin filament at Step 0 (no load)



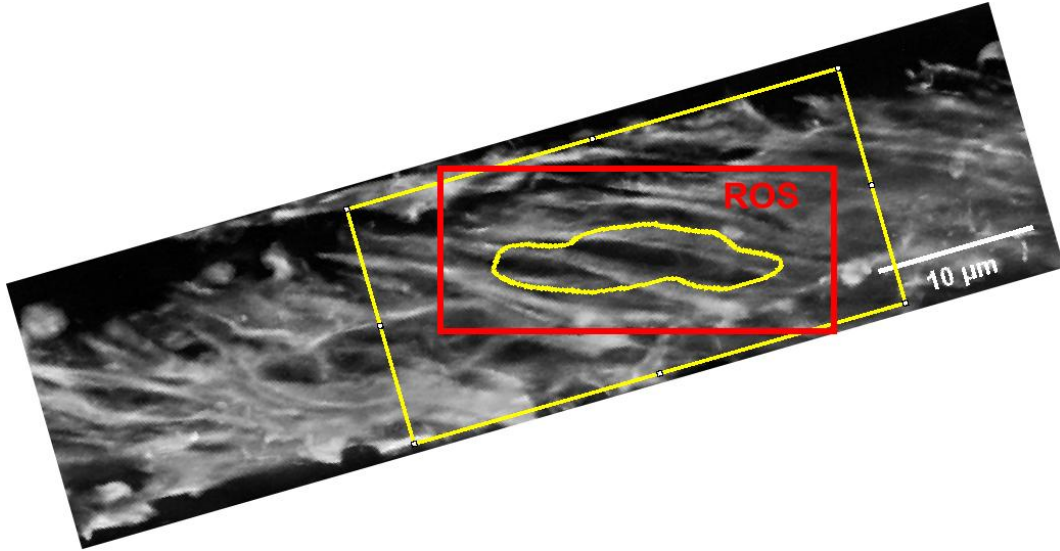
(c) Actin filament at Step 1



(d) Rotation of the actin image (Step 0)



(e) Definition of the ROI (Step 0)



(f) Definition of the ROS (Step 1)

Fig. 2.14 The image processing procedure to obtain the region of interest (ROI) in Step i and corresponding region of search (ROS) in Step $i+1$ in the circumferential stretch case.

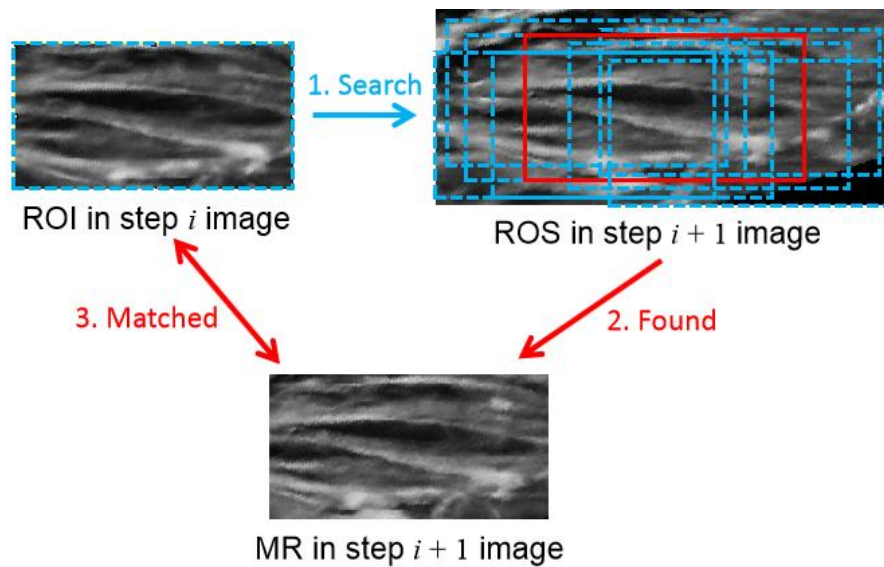


Fig. 2.15 The schema of searching for the MR area with the most similar region of interest (ROI), *i.e.*, matched region (MR) within the region of search (ROS).

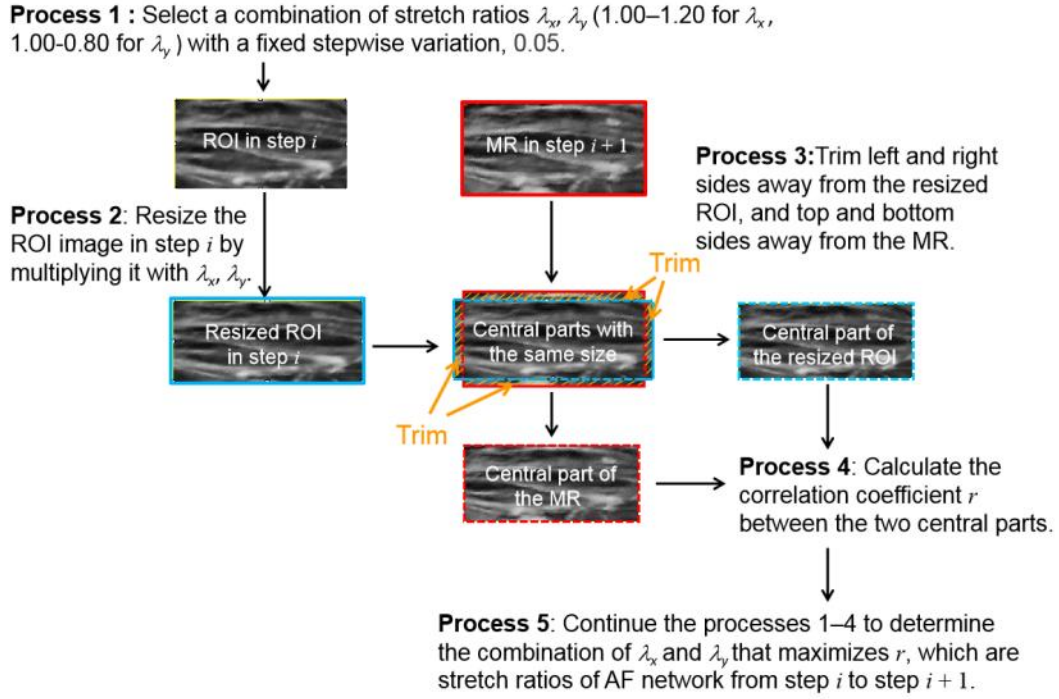
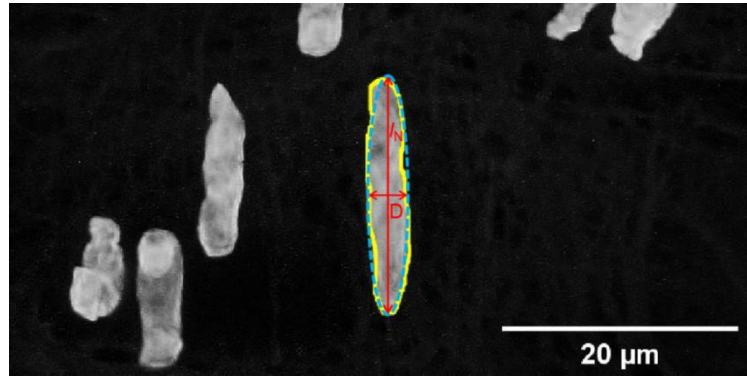
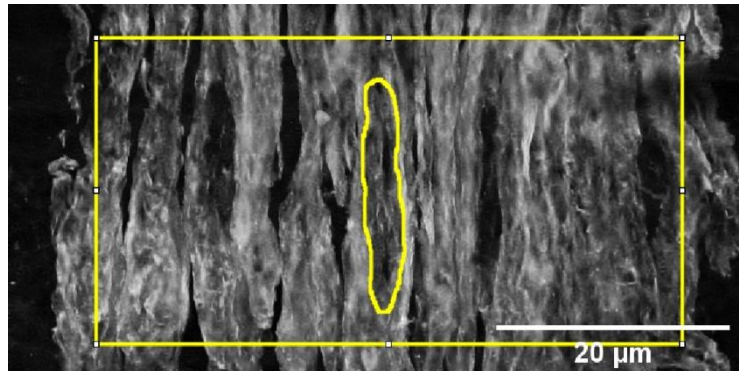


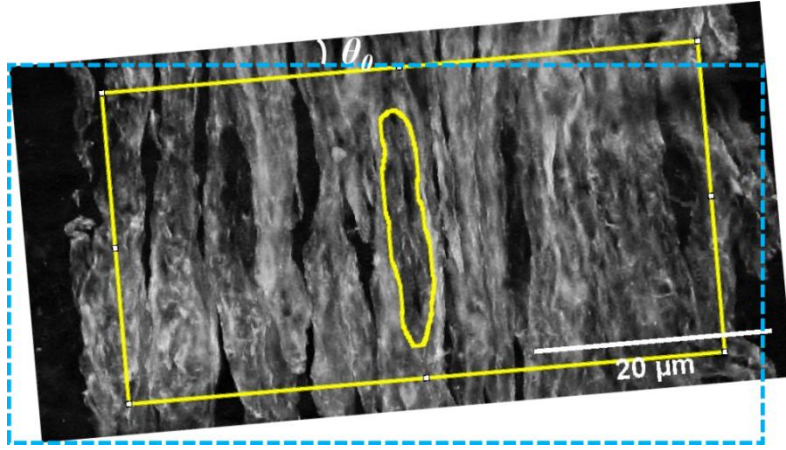
Fig. 2.16 The image processing procedure to obtain the stretch ratios between the two stretch steps.



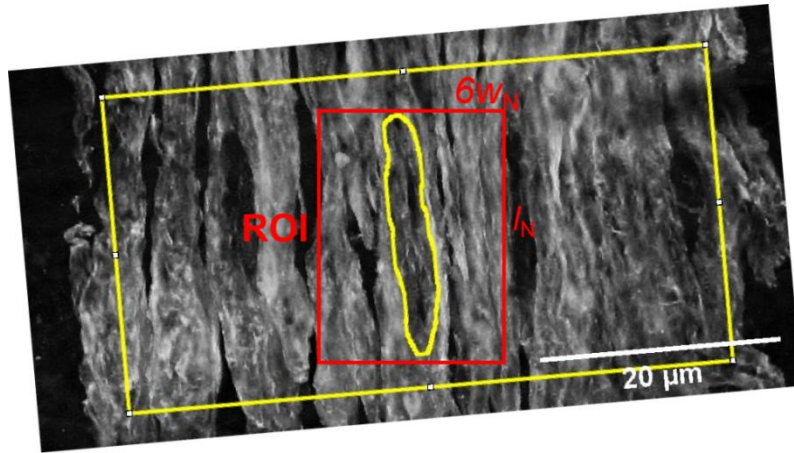
(a) Nuclei at Step 0 (no load) in axial stretch



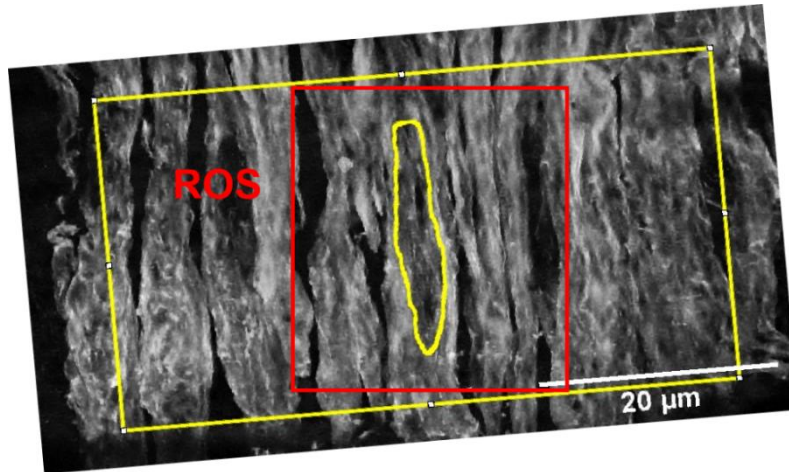
(b) Actin filament at Step 0 (no load), yellow frame is $3L_N \times 1.5L_N$



(c) Rotation of the actin image (Step 0) in the axial stretch



(d) Definition of the ROI (Step 0) in the axial stretch, the size of the ROI is $l_N \times 6w_N$



(e) Definition of the ROS (Step 1)

Fig. 2.17 The image processing procedure to obtain the region of interest (ROI) in Step i and corresponding region of search (ROS) in Step $i+1$ in the axial stretch case.

2.7 Statistical analyses

All the data were expressed as mean \pm SD. Differences in the data between nucleus and actin were analyzed with paired Student's t-test, whereas the differences in the data between circumferential stretch and axial stretch of nucleus or actin were analyzed with unpaired Student's t-test.

2.8 Discussion

This chapter introduces the method of experiment and analysis. To improve the reproducibility of the experiment and to reduce the variation of the data obtained in the experiment, the discussion will concentrate on several points in the experiment and analysis.

First, all tensile tests were performed within 24 hours after the rabbit was sacrificed. The tissue can be preserved for long times at low temperate, it can be preserved for up to 7 days within stabilization solutions and even longer time when it is frozen (Lou et al. 2014). To minimize the effect of photo bleaching caused by laser irradiation during the observation, the tensile process for every slice was finished within 2 hours. To assess the deviations effect of the photobleaching, a time-lapse observation experiment was performed for the sample slices, the length change of the nuclei major axis was less than 0.5% ($n = 4$, $P < 0.05$).

To measure the length of the longitudinal and transverse axes of the nucleus, ImageJ was utilized to match the nuclear outline to the ellipsoid automatically. Although the longitudinal axis can be obviously determined after fitting to the ellipsoid, the transverse axis of the ellipsoid might be different from the original nucleus because some nuclei bend along the transverse direction. To uniformly and conveniently evaluate, the length of the transverse axis was defined as that it is equal to the area of the ellipsoid divided by its longitudinal axis.

Some other research measured the number of the stress fibers within a cell, for

example, Nagayama et al. 2010 measured the number of stress fibers with a single SMC by using the fluorescent intensity distribution of SFs in a direction perpendicular to the cell major axis. The number of peaks of the intensity distributions was regarded as the number of SFs. Theoretically speaking, by measuring the interval distance change between two peaks of the intensity distributions, the stretch ratio of the AF network can be measured, while this method requires an extremely clear image of the AF network where every single stress fiber can be recognized. Obviously, that is impossible in this experiment, so the present method was developed, by which the stretch ratio of the AF can be measured with an image of any sharpness. This method can be used to measure any tissue deformation in theory.

To test if the method being used to measure AF deformation was correct, an artificial image was used for verification. The image has a size of 565×555 pixels (Fig. 2.18(a)), its size was modified to 679×500 pixel (Fig. 2.18(b)), so the stretch ratios are about 1.2 and 0.9 in the vertical and horizontal directions, respectively, i.e., the absolute strains are 0.2 and 0.1, respectively. An ROI was defined in the image before modification (red square in Fig. 2.18(a)). Then, a best-matched MR (matched region, defined in step 3 of Section 2.6.5) image (Fig. 2.18(d)) using MATLAB (see Appendix 2 for the codes used in the analysis) was found within the defined ROS in the image after modification (Fig. 2.18(b)). Then MATLAB was used to find the strain in the vertical and horizontal directions to match Fig. 2.18(c) and (d), the procedure of the image analysis has already been explained in Section 2.6.5. The

strains were calculated by using the MATLAB. The absolute vertical and horizontal strains are about 0.195 and 0.105, which are very close to the strains given for Fig. 2.18(b). Thus, it can be concluded that the code works well on calculation.

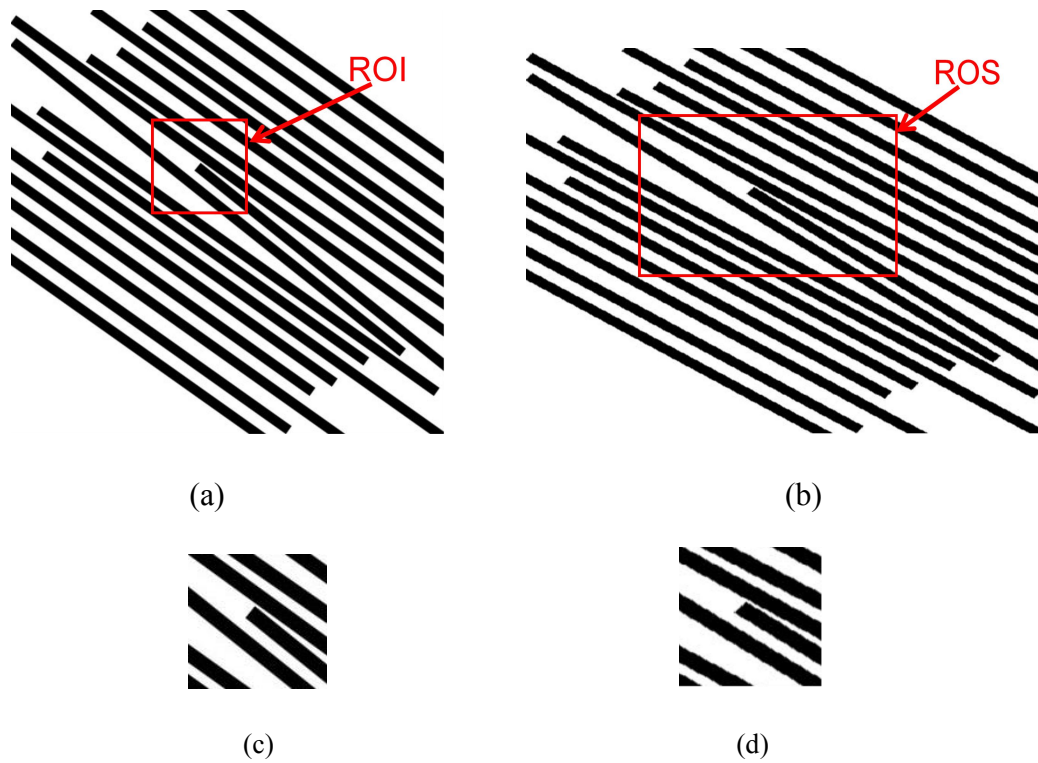


Fig. 2.18 Artificial images used to check the MATLAB code I wrote for the image analysis of the AF. The original image (a) was stretched 20% in the horizontal direction and compressed 10% in the vertical direction (b). The best matched image (d) of the ROI in the original image (c) was searched within the ROS in (b).

References

Fan Y, Wang JF, Maeda E, Murase K, Matsumoto T (2019) Analysis of heterogeneous deformation in the wall of rabbit thoracic aorta at microscopic level. *Adv. Biomed. Eng.* 8:7–13.

Lou JJ, Mirsadraei L, Desiree ES et al (2014). A review of room temperature storage of biospecimen tissue and nucleic acids for anatomic pathology laboratories and biorepositories. *Clin. Biochem.* 47(4-5):267–73.

Matsumoto T, Abe H, Ohashi T, Kato Y, Sato M (2002) Local elastic modulus of atherosclerotic lesions of rabbit thoracic aortas measured by pipette aspiration method. *Physiol. Meas.* 23(4):635–648.

Nagayama K, Matsumoto T (2010) Estimation of single stress fiber stiffness in cultured aortic smooth muscle cells under relaxed and contracted states: Its relation to dynamic rearrangement of stress fibers, *J. Biomech.* 43(8): 1443–1449.

Pan B, Qian K, Xie H, Asundi A (2009) Two-dimensional digital image correlation for in-plane displacement and strain measurement: a review. *Meas. Sci. Technol.* 20:062001.

Zhao R, Simmons CA (2012) An improved texture correlation algorithm to measure substrate-cytoskeletal network strain transfer under large compressive strain. *J. Biomech.* 45:76–82.

Chapter 3 Heterogeneous deformation of the media

3.1 Summary of this chapter

There is growing evidence that the aortic wall does not deform uniformly during pressurization. It has been reported that the aortic wall shows not only heterogeneous deformation at a microscopic level (Matsumoto et al. 2013) but also shear deformation (Sugita et al. 2020) in response to circumferential stretch. This chapter will show the measurement and calculation results of the heterogeneous deformation of the media against the mechanical stretch.

The result of type-1 slices was used, i.e., deformation measured in the section perpendicular to the vessel axis for the calculation. Firstly, the media was divided into several layers referring to the elastic laminas. The stretch ratio of each layer was calculated as well as the shear deformation between every two adjacent layers. Then, the heterogeneous deformation was observed between the elastic laminas.

Then, the distribution of horizontal, vertical and shear components of Green strain along with the stretch process were calculated for type-1 slice. They were calculated by plotting the nuclei in the image to draw triangles and then by tracing the movement of the vertex of every triangle during the stretch. More obvious heterogeneity of the media was observed using this method compared to that at the lamina level.

3.2 Macroscopic shear deformation between the laminae of the media

Fig. 3.1 shows a case of how I divided the laminae, it can be seen that these lamina layers contract in the vertical direction and elongated in the stretch direction obviously along with the stretch process. The shear deformation between the laminae was calculated at a macroscopic viewpoint (Section 2.6.2) *i.e.*, on a scale of about 200 μm , as shown in Fig.3.1.

The representative data of the macroscopic elongation of the specimen, and the microscopic elongation of the SMLs are shown in Fig. 3.2. As shown in Fig. 3.2(a), the elongation of each layer is relatively close to the homogeneous body line where both macroscopic and microscopic stretch ratios are the same. In terms of strain (= stretch ratio - 1), the maximum deviation of the absolute difference between the value of the individual layer and the homogeneous body line, is 20% at $A_x = 1.45$. It is also evident that the elongation rate of the SMLs is inconsistent among the seven layers examined up to $A_x = 1.16$; the rate is almost consistent in the seven layers thereafter. This may indicate that the wavy ELs became almost straight and the rotation of most of the nucleus ceased over this point, causing homogeneous deformation. With regard to shear strain between two adjacent laminae, it changes primarily in the low-strain range ($A_x < 1.16$) and appeared to become stabilized over this point except at $A_x = 1.46$ (Fig. 3.2(b)). This may indicate that heterogeneous deformation occurs primarily in the low-strain region, as shown in (a). The maximum shear strain is as large as 10%.

Considering that the shear strain in the homogeneous body is zero, such 10% strain is not negligible. The results of another specimen show the maximum deviation of 6% for the stretch ratio, and a shear strain of within 12%. The mean maximum deviation for the laminae stretch ratio of the two samples was 13%, and the mean maximum deviation for the shear strain was 11%.

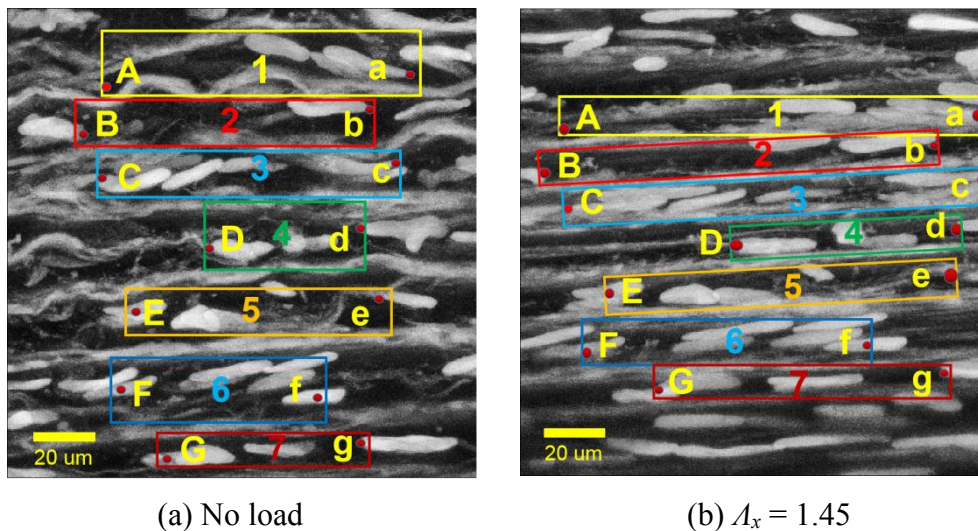
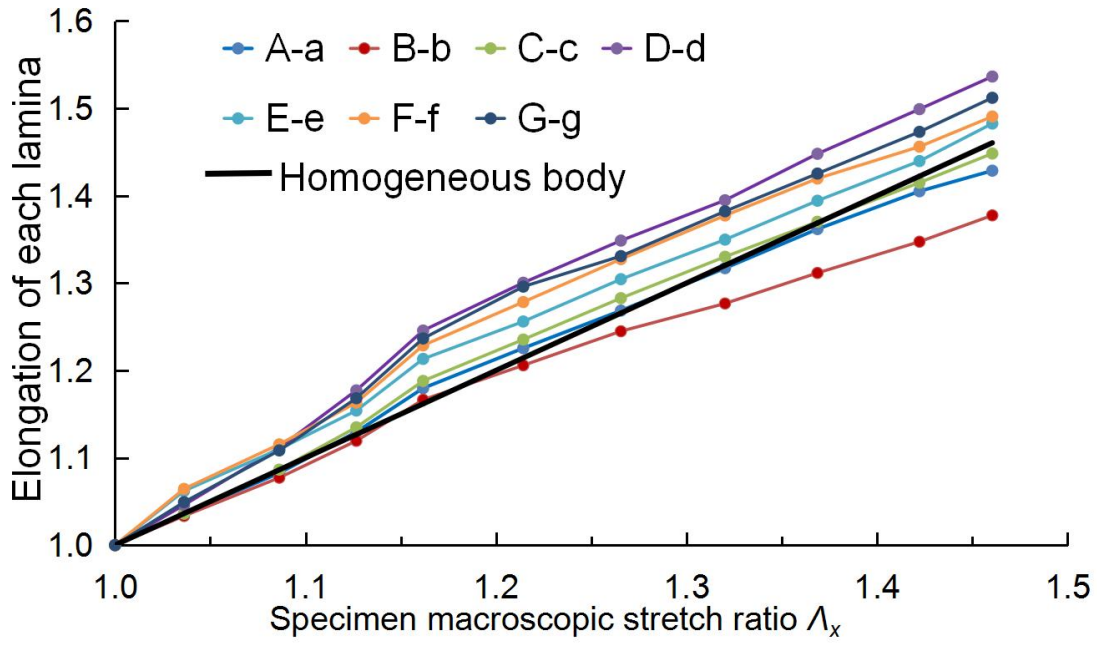
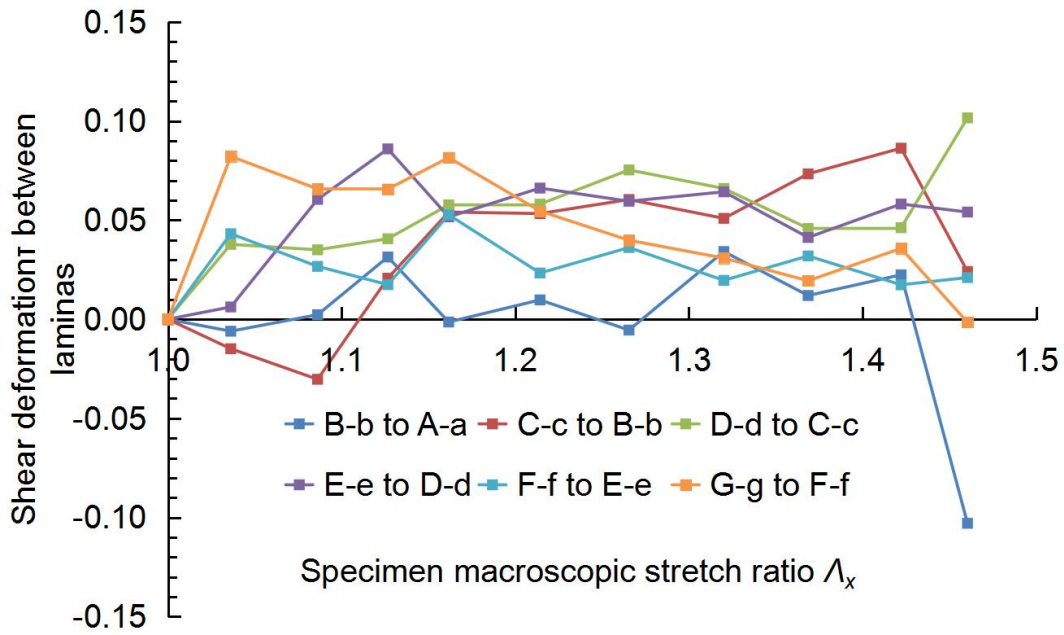


Fig. 3.1 Fluorescent images of a media of type-1 slice. Smooth muscle nuclei and elastic laminae are shown in white. Capital and small alphabet letters (A-G and a-g) indicate different layers (Fan et al. 2019)



(a) Elongation of each SML

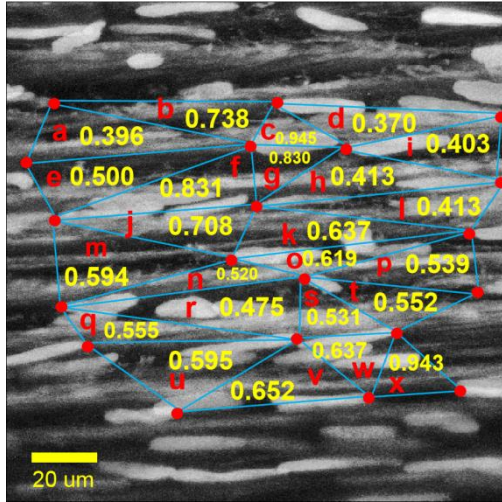


(b) Shear deformation between SMLs

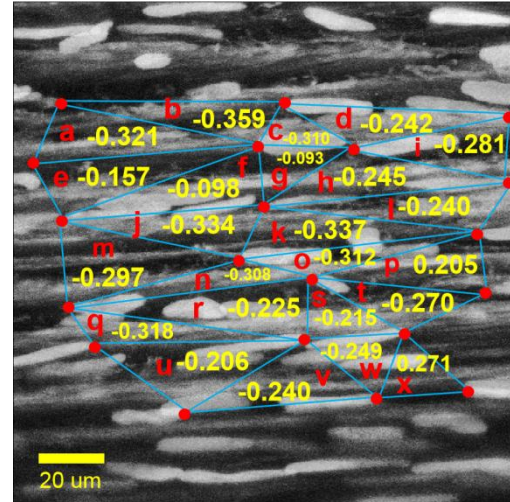
Fig. 3.2 Relationship between the stretch ratio of elastic layers and the ratio of the macroscopic stretch (a). Relationship between shear deformation between two adjacent laminae and the macroscopic stretch ratio (b). (Fan et al. 2019).

3.3 Microscopic heterogeneous deformation of the media

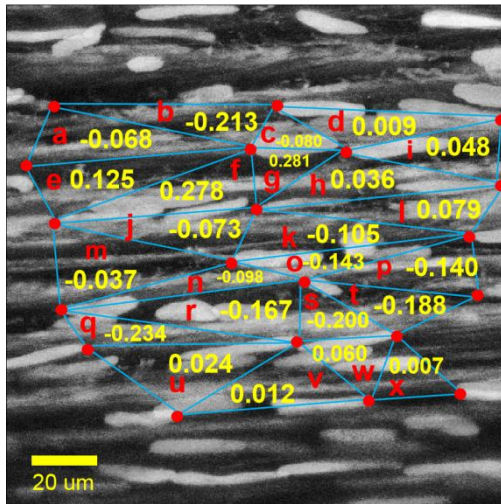
The heterogeneous deformation of the media was calculated at a microscopic viewpoint *i.e.*, on a scale of the nucleus of about 20 μm (shown in Fig. 3.3). A representative example of the Green strain distribution at $\lambda_x = 1.45$ is shown in Fig. 3.3. When each Green strain component, namely, E_{11} , E_{22} , and E_{12} according to the formula 2.5 is plotted against the macroscopic stretch ratio λ_x as shown in Fig. 3.4, the deviation from the homogeneous body line was as high as 117% in E_{11} . The E_{11} values were varied in the same SML as well as between different SMLs (Fig. 3.3(a)). For example, it varied from 0.413 to 0.831 in the regions e, f, g, h that constitute one layer of SM. Regions d, h, k, s with similar circumferential position but from different layer of lamina have various strain from 0.370 to 0.637. Contrary to the shear strain between adjacent layers, it continues to increase with the circumferential stretch, as shown in Fig. 3.4(a). The E_{22} also varies in the same or different SMLs, as shown in Fig. 3.3(b) like E_{11} . And E_{22} decreased as the sample was stretched (Fig. 3.4(b)). In some locations, the shear strain of a triangle was even twice as large as that between the adjacent layers (Fig. 3.3(c)). For example, the strain at region f and l was twice as large as those in region e and h, respectively. These results indicate that the heterogeneity observed at the lamellar level becomes larger when observed at the cellular level.



(a) Horizontal

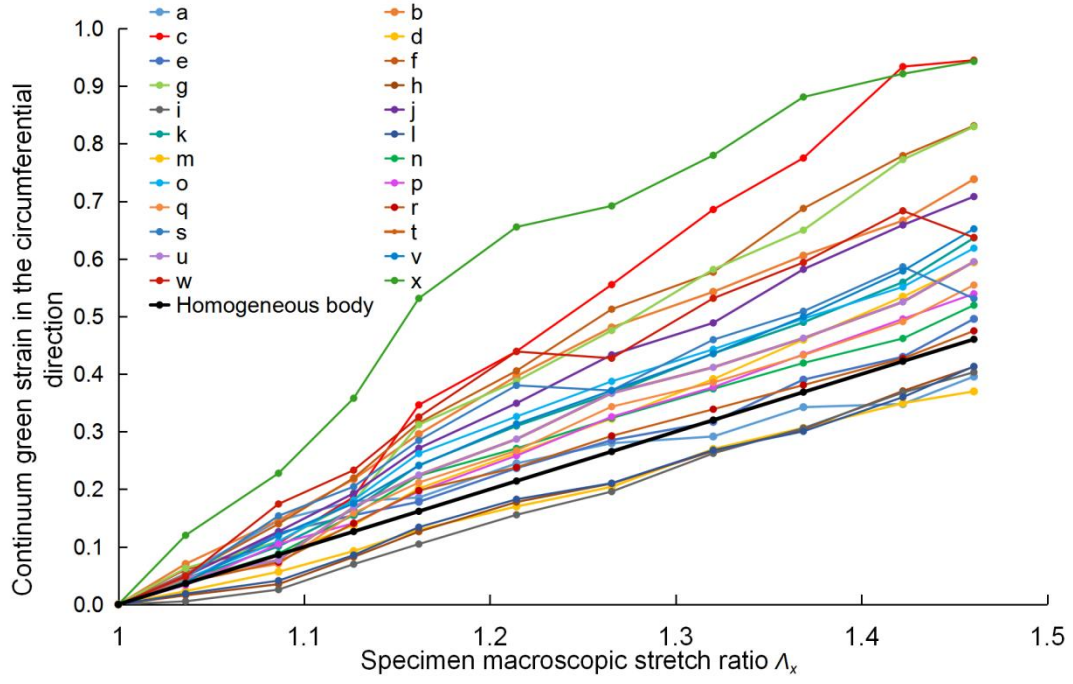


(b) Vertical

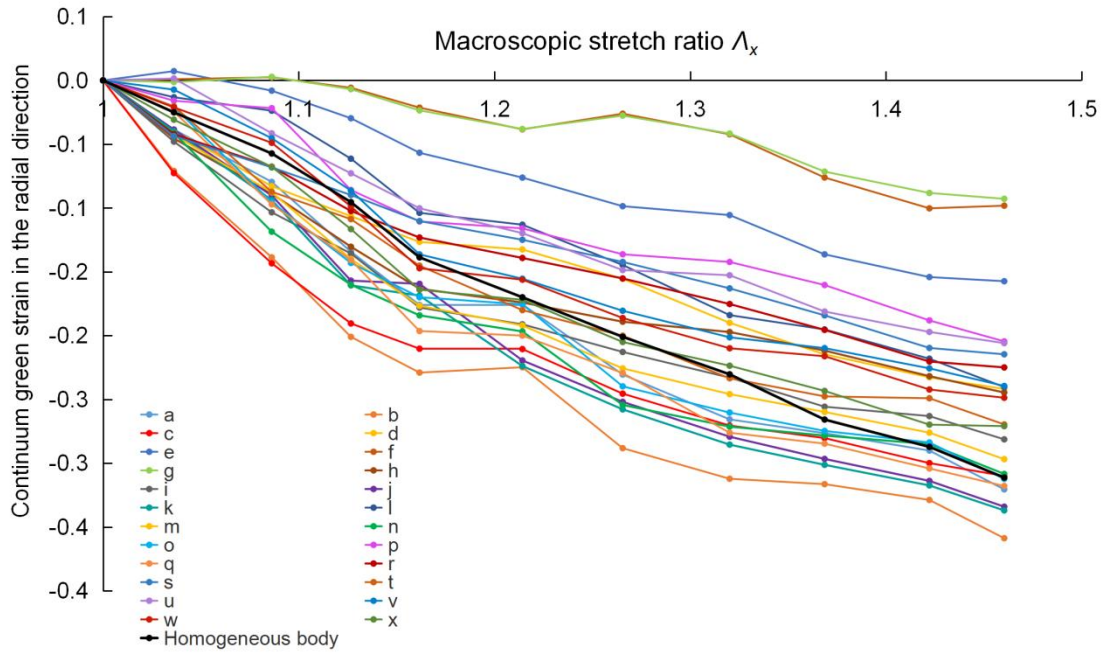


(c) Shear

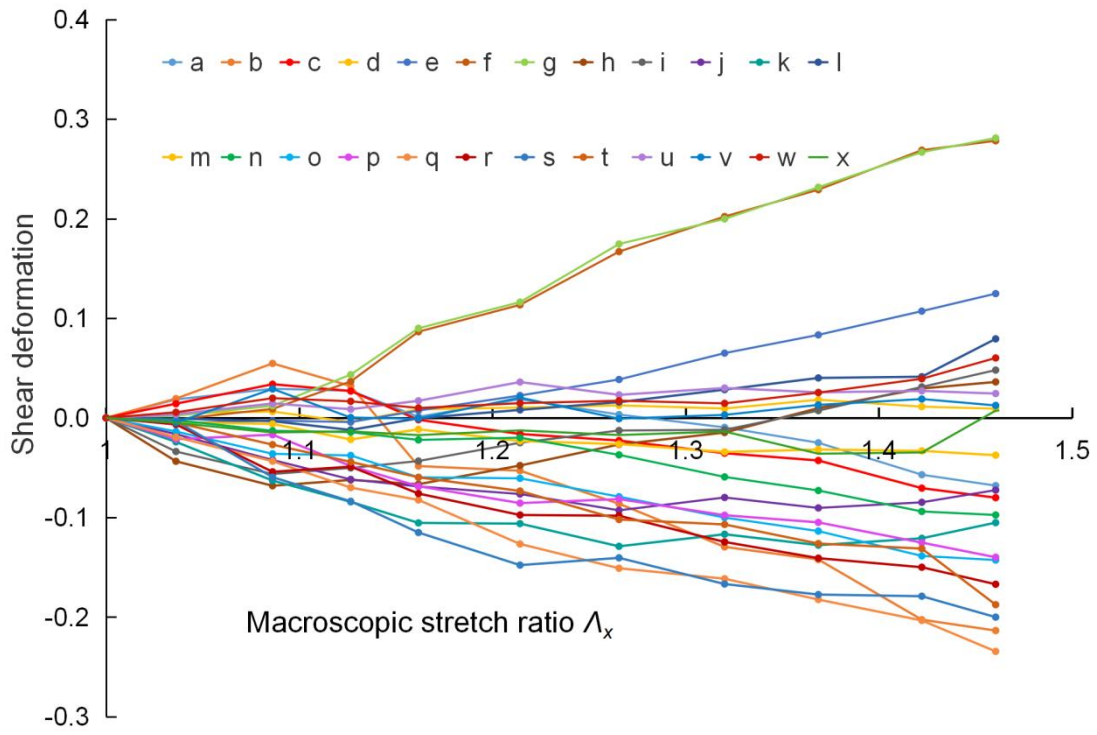
Fig. 3.3 Example of Green strain distributions for a type-1 slice after circumferential stretch ($\lambda_x = 1.45$). Green strains in the horizontal (a) and vertical (b) directions, and the shear component (c) are shown in each triangle. (Fan et al. 2019).



(a) Circumferential strain E_{11}



(b) Radial strain E_{22}



(c) Shear strain E_{12} ($=E_{21}$)

Fig. 3.4 The change in strain in each triangle against circumferential stretch. Characters a to x corresponds to individual triangles in the Fig. 3.3. (Fan et al. 2019).

3.4 Discussion

The media of the aorta primarily consist of SMCs, and elastin and collagen fibers. The mechanical heterogeneity of the media is caused by the difference in Young's modulus of the elastin, collagen and SMC. The aorta has been demonstrated to show complex mechanical behaviors when it is subjected to physiological loading from the unloaded state in vivo (Matsumoto et al. 2004). These complex mechanical phenomena are caused by the intricate structure of the three components (Chow et al. 2013). The intricate structure also causes the heterogeneity of stress distribution in the media (Nagayama and Matsumoto 2004). Furthermore, it has been suggested that the protein synthesis in SMCs is closely correlated with the heterogeneity of the vessel wall (Matsumoto et al. 2015). In addition, the deformation of the aorta due to pressurization is complicated because of the structural heterogeneity of tissue layers and the differences in the elastic properties of elastin layers (ELs), smooth muscle layers (SMLs), and the surrounding collagen and elastin (Sugita and Matsumoto 2017). Nonetheless, the details of heterogeneous deformation and strain field within the media remain to be studied.

This study focused on the mechanical heterogeneity of the rabbit thoracic aortic walls by measuring their deformations of SMLs, as well as the nuclei of SMCs during the tensile test in the circumferential and longitudinal directions. The elongation of each SML showed weak heterogeneity in response to circumferential stretch (Fig. 3.2), and this heterogeneity became more remarkable when the deformation was evaluated

with the local Green strain (Figs. 3.3 and 3.4). These results may indicate that the heterogeneity increases more as at smaller scales of at least the cellular level.

According to Figs. 3.2(b), 3.3(c) and 3.4(c), the aortic wall shows shear deformation during circumferential stretch. This clearly indicated that the aortic wall was deformed with the combination of stretch and shear deformations during the tensile test, which coincided with the findings of a past study (Matsumoto et al. 2004). Although the amount of shear deformation was not large (<0.1) in most cases, this might exhibit profound effects on the physiological functions of the SMCs.

The precise mechanism causing such heterogeneities is still unclear at this stage. However, the apparent structural heterogeneity in the wall may account for the observed heterogeneity. This includes the varied thickness and structure of the SMLs and ELs, and the connections of ELs to the collagen fiber networks. Since the ELs and the nuclei can be visualized only in a superficial region ($\sim 20\text{ }\mu\text{m}$ from the surface at the maximum) of the 200- μm -thick specimens, a new method that can visualize the specimen in the whole thickness is awaited.

It also shows that the corrugated elastin layers became straight after stretching, as shown in Fig. 3.1. The different waviness of different lamellar units in Fig.3.1 at no-load state may be evidence of the heterogeneous distribution of the circumferential residual stress along the vascular radial direction at physiological state (Matsumoto et al. 1996).

In conclusion, the SMLs in rabbit thoracic aorta exhibited heterogeneous deformation in response to circumferential tensile stretch at both the macroscopic and

microscopic levels, and the heterogeneity was more prominent at the microscopic level. At macroscopic viewpoint, the difference between the largest and smallest strain is about 1.4 times at $A_x = 1.45$, as shown in Fig.3.2 (a), while at a microscopic viewpoint, the largest strain is about 2.4 times smallest at $A_x = 1.45$, which means that if we consider the nucleus together with the elastic laminae, the heterogeneity of the tissue will be greater. From a macroscopic view, the heterogeneity changes primarily in the low-strain range ($A_x < 1.16$, the slopes of lines are quite different) and appeared to become stabilized over this point except at $A_x = 1.46$ (Fig. 3.2(a)). However, this kind trend has not been shown in Fig.3.4 from a microscopic viewpoint.

References

Chow MJ, Choi M, Yun SH, Zhang YH (2013) The Effect of Static Stretch on Elastin Degradation in Arteries. PLoS ONE 8(12): e81951.

Fan Y, Wang JF, Maeda E, Murase K, Matsumoto T (2019) Analysis of heterogeneous deformation in the wall of rabbit thoracic aorta at microscopic level. Adv. Biomed. Eng. 8:7–13.

Matsumoto T, Hayashi K (1996) Stress and strain distribution in hypertensive and normotensive rat aorta considering residual strain. ASME. J. Biomech. Eng. 118:62–73.

Matsumoto T, Goto T, Furukawa T, Sato M (2004) Residual stress and strain in the lamellar unit of the porcine aorta: experiment and analysis. J. Biomech. 37(6): 807–815.

Matsumoto T, Fukunaga A, Narita K, Uno Y, Nagayama K. Chapter 14 Heterogeneity in Microscopic Residual Stress in the Aortic Wall. F. Barthelat et al. (2013) Mechanics of Biological Systems and Materials, Volume 4, Conference Proceedings of the Society for Experimental Mechanics Series.

Matsumoto T, Uno Y, Iijima S, Moriyama Y, Sugita S, Nagayama K, Matsumoto A. Microscopic heterogeneity in the aortic wall: Correlation between mechanical environment and protein expression, Proc 2015 Summer Biomech Bioeng Biotrans Conf, SB3C2015–567.

Nagayama K, Matsumoto T (2004) Mechanical anisotropy of rat aortic smooth muscle cells decreases with their contraction. JSME. Int. J. 47(4): 341–348.

Sugita S, Matsumoto T (2017) Multiphoton microscopy observations of 3D elastin and collagen fiber microstructure changes during pressurization in aortic media.

Biomech. Model. Mechanobiol. 16:763–773.

Sugita S, Kato M, Wataru F , Nakamura M (2020) Three-dimensional analysis of the thoracic aorta microscopic deformation during intraluminal pressurization. Biomech. Model. Mechanobiol. 19(1):147–157.

Chapter 4 Deformation of the actin filament (AF) network against stretch

4.1 Summary of this chapter

AF plays an important role in transmitting the extracellular force to the nucleus. Their deformation induces local deformation of the nucleus, which might enhance protein synthesis. Will AF show anisotropic deformation? What is the difference between the deformation of AF and the cell body? This chapter will show the results of AF deformation against circumferential and axial stretches.

All the slices were stretched to about 1.40 times greater than that of lengths under no-load state within 5–6 stretch steps with 6–8% stepwise strain. Since the series of the macroscopic stretch ratios applied to each slice is different among slices, to compare the results of different slices, I calculated the stretch ratios for all slices with linear interpolations at every 0.05 from $\lambda_x = 1$ to 1.35 in the 2D analysis. The AF deformation was analyzed at the 2D view because the 3D analysis of the AF could not be performed due to its complex structure. There was no significant difference in the deformation between AF and the entire cell for both stretch cases.

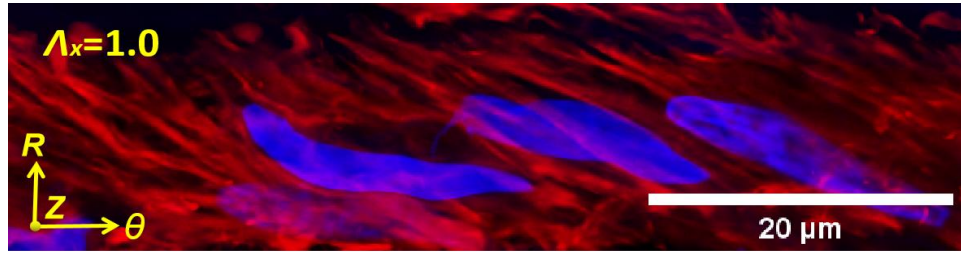
4.2 Deformation of the AF

4.2.1 Circumferential stretch

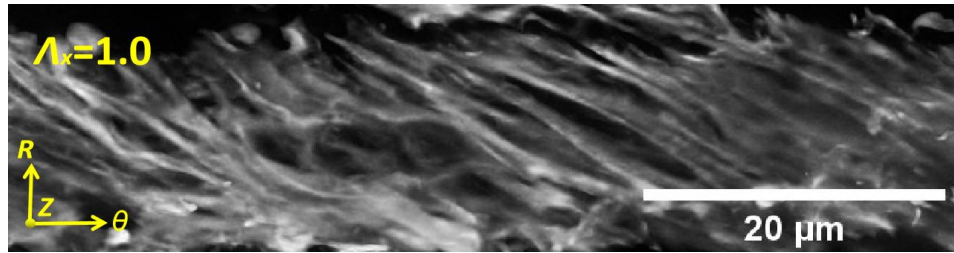
Figs. 4.1 and 4.2 show the AF around a nucleus before and after applying a circumferential stretch, respectively. The interval of the AF became smaller along with the stretch process. While the AF network elongated in its orientation direction, it did not exactly align along the horizontal direction. The AF network was slightly inclined with a small angle so that this was taken into consideration in the calculation of the hypothetical deformation in Eqs. 2.10–2.12, 2.14–2.15 by adding the parameter of orientation angles of nucleus and AF network. For example, in the SMC case, by taking the hypothetical orientation angle $\theta_N^h(i)$ into Eq.2.10, we got $\theta_N^h(i+1)$, and by taking $\theta_N^h(i)$ into Eqs.2.12–16, we got hypothetical stretch ratio of the SMC for every stretch step.

Fig. 4.3 (a) and (b) represent the stretch ratios of the AF networks in their oriented direction and the direction perpendicular to their orientation against the circumferential stretch. The AF network elongated in its oriented direction, whereas it shrank in the direction perpendicular to its orientation against the circumferential stretch. Fig. 4.3 (a) and (b) represent that the mean stretch ratios of λ_{Al} and λ_{At} at $\lambda_x = 1.35$ were 1.40 ± 0.20 ($n = 8$) and 0.76 ± 0.10 with a large variability from 1.08 to 1.71 and 0.61 to 0.92, respectively. $\varepsilon_{At}/\varepsilon_{Al}$ at $\lambda_x = 1.35$ does not meet the Poisson's number, the reason may be that the AF is not orientated aligned in the horizontal direction completely when the stretch process begins, although that orientation angle

is small.

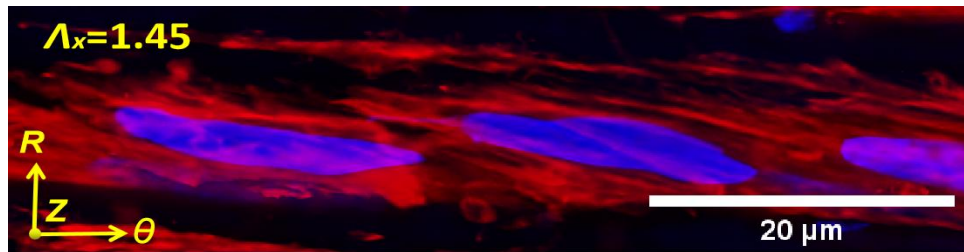


(a) Merged image of the nucleus and AF before stretch

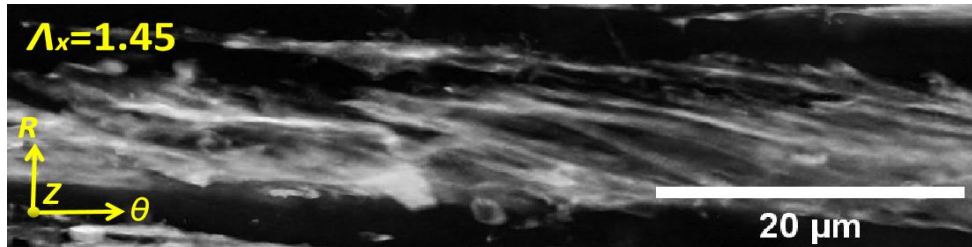


(b) Black and white image of the AF before stretch

Fig. 4.1 Staining images of the AF and nucleus at a no-load state ($\lambda_x = 1.00$) before the circumferential stretch. Blue and red color in (a) indicate SMC nuclei and AF network, respectively.

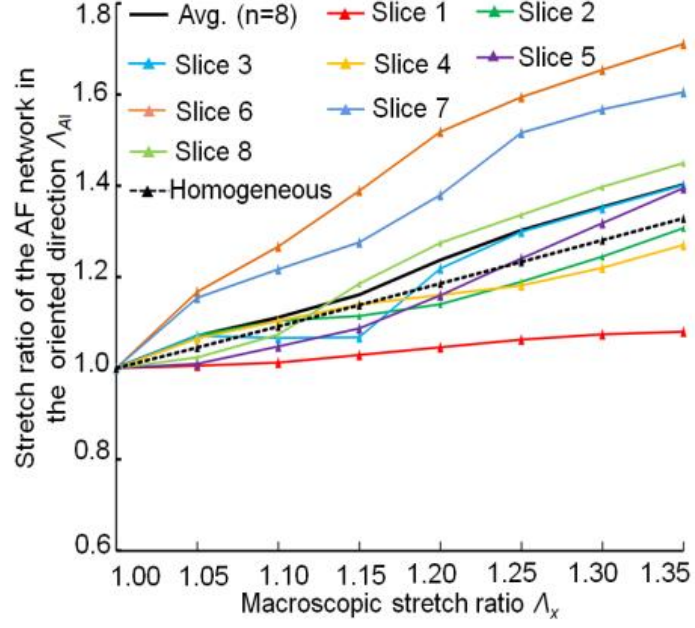


(a) Merged image of the nucleus and AF after stretch

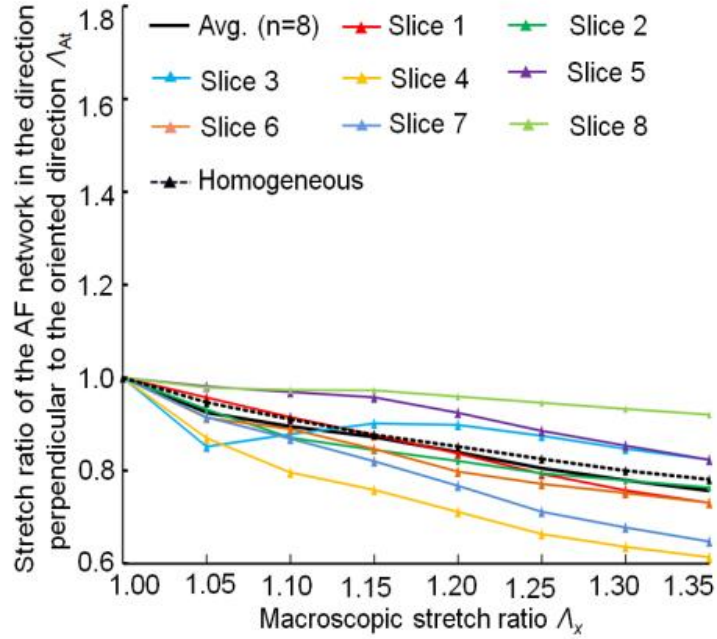


(b) Black and white image of the AF after stretch

Fig. 4.2 Staining images of the AF and nucleus after stretch ($\lambda_x = 1.45$) against the circumferential stretch. Blue and red color in (a) indicate SMC nuclei and AF network, respectively.



(a) AF deformation λ_{Al} in circumferential stretch



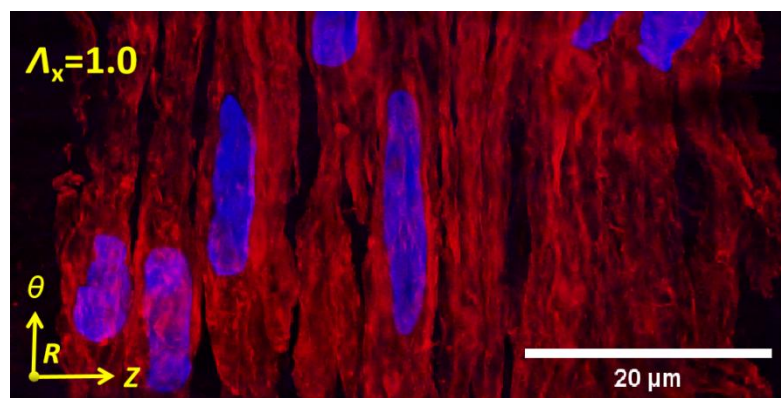
(b) AF deformation λ_{At} in circumferential stretch

Fig. 4.3 Two-dimensional deformations of the AF network in the oriented direction (a) and the direction perpendicular to its orientation (b) against the circumferential stretch.

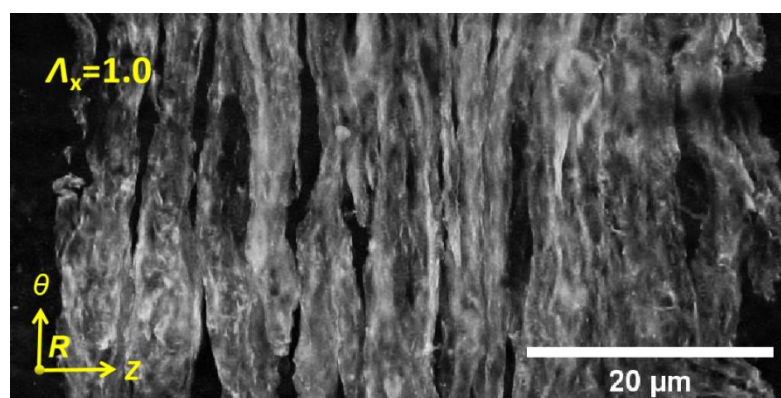
4.2.2 Axial stretch

Fig. 4.4 and 4.5 show the AF before and after applying an axial stretch, respectively. The AF shrank in its oriented direction, whereas it elongated in the direction perpendicular to the orientation direction against the axial stretch.

Fig.4.6 (a) and (b) represent the stretch ratios of the AF networks in their oriented direction and the direction perpendicular to their orientation against the axial stretch, respectively. The mean stretch ratios of λ_{Al} and λ_{At} at $\lambda_x = 1.35$ were 0.90 ± 0.07 ($n = 5$) and 1.26 ± 0.11 , ranging from 0.81 to 0.98 and 1.14 to 1.40, respectively.

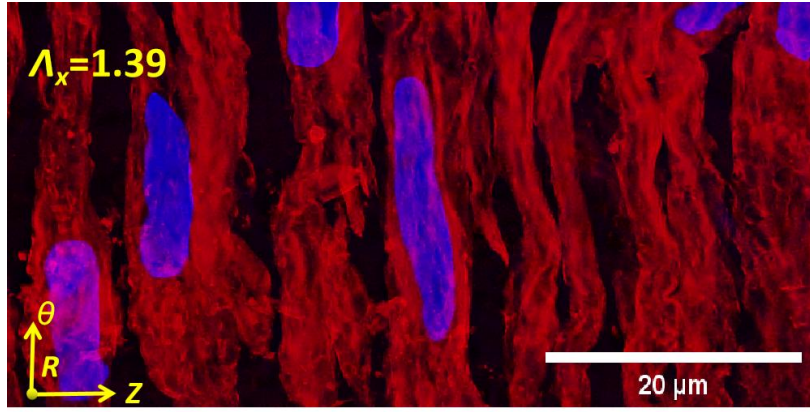


(a) Merged image of the nucleus and AF before stretch

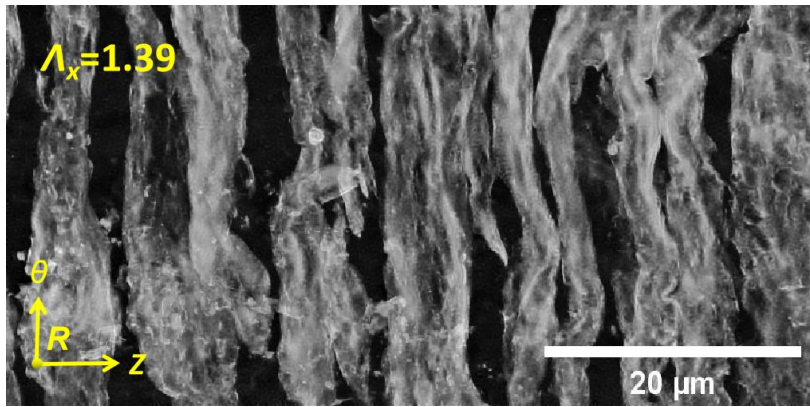


(b) Black and white image of the AF before stretch

Fig. 4.4 Staining images of the AF and nucleus at no-load state ($\lambda_x = 1.0$) against the axial stretch. Merge image of the nucleus and AF (a). Blue and red color indicate SMC nuclei and AF network. Black and white image of the AF (b).

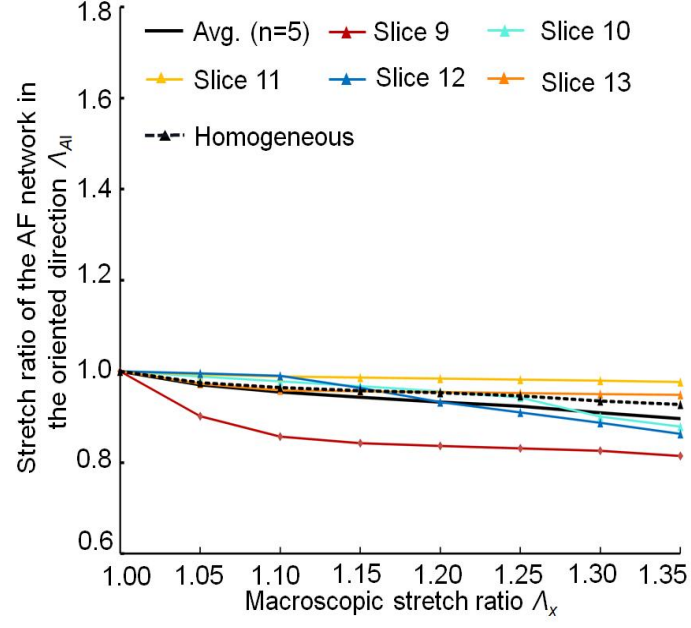


(a) Merged image of the nucleus and AF after stretch

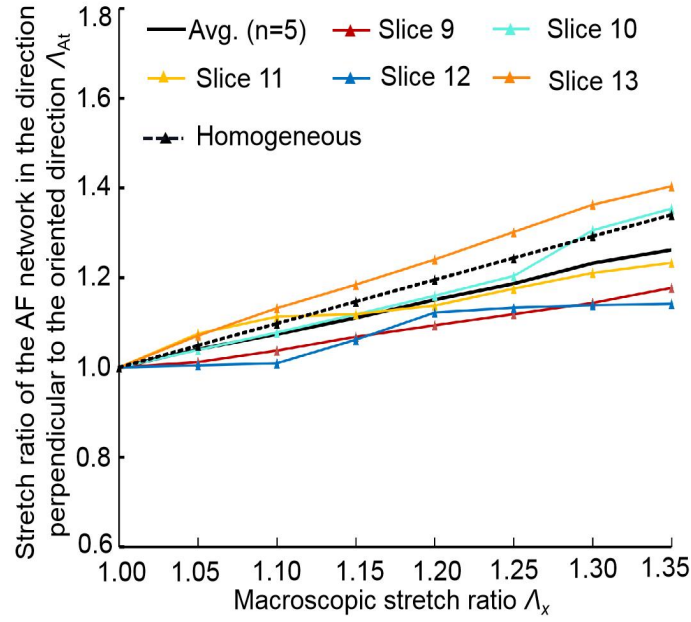


(b) Black and white image of the AF after stretch

Fig. 4.5 Staining images of the AF and nucleus at $\lambda_x = 1.39$ against the circumferential stretch. Merge image of the nucleus and AF (a). Blue and red color indicate SMC nuclei and AF network. Black and white image of the AF (b).



(a) AF deformation λ_{Ai} in axial stretch



(b) AF deformation λ_{At} in axial stretch

Fig. 4.6 Two-dimensional deformations of the AF network in the oriented direction (a) and in the direction perpendicular to its orientation (b) against the axial stretch.

4.3 Comparison with the deformation of the homogeneous body

In the circumferential stretch, the homogeneous stretch ratios λ_{Al}^h and λ_{At}^h were 1.33 ± 0.02 and 0.78 ± 0.04 ($n = 8$) at $\lambda_x = 1.35$, respectively (black solid lines in Fig.4.3). In the axial stretch, the mean homogeneous stretch ratios of λ_{Al}^h and λ_{At}^h at $\lambda_x = 1.35$ were 0.93 ± 0.06 and 1.34 ± 0.01 ($n = 5$), respectively (black solid lines in Fig.4.6).

For AF network deformation, no significant difference was observed in any cases between the measurement and the homogeneous deformation, indicating that the AF network deforms similarly to the tissue although the SD was relatively large in some cases. The large SD value may be because 1) those sliced samples are harvested from different rabbits that their stretch ratios are not the same, 2) as the AF stretch ratios were measured using the twice magnified images, SD value reveals that heterogeneity is more obvious at a microscopic view point of the cell scale, 3) for comparing all the stretch ratios of all sliced samples uniformly, the stretch ratio of each sliced sample to $\lambda_x = 1.35$ was the estimated value calculated by linear interpolation depending on the values around $\lambda_x = 1.35$, which may affect the SD value a little.

4.4 Discussion

In this chapter, the deformation of the AF network against the circumferential and axial stretches was shown. The AF network tended to elongate more in the circumferential stretch than the axial one although there was no significant difference. In both types of stretch, there were no significant differences between the deformation of the AF network (black solid lines in Figs. 4.3(a) and 4.6(b)) and the homogeneous assumption that corresponds to the deformation of the entire cell (black dash lines). As the cytoskeleton, actin filaments are connected to the cell membrane via focal adhesions. They thus deform together with the cell membrane during stretch. So, there might be no significant difference between the deformation of AF and cell body.

The mechanical stability of the nucleus is important for maintaining nuclear shape by minimizing nuclear deformation and strain when deformed (Wang et al. 2018). It is proposed that the cytoskeleton enhances nuclear mechanical stability by lowering the effective deformability of the nucleus while maintaining nuclear sensitivity to mechanical stimuli (Wang et al. 2018) *i.e.*, the AFs act as an “energy buffer” to the nucleus for minimizing the strain energy change when the cell is subjected to stimuli. So, except the larger stiffness of the nucleus than the AF, another possible reason why the deformation of the nucleus is smaller than the AF network when the cell is under stimuli is that: the strain has not yet been transferred to the nucleus through the AF.

Reference

Wang X, Liu H, Zhu M, Cao C, Xu Z, Tsatskis Y, Lau K, Kuok C, Filleter T, McNeill H, Simmons CA, Hopyan S, Sun Y (2018) Mechanical stability of the cell nucleus – roles played by the cytoskeleton in nuclear deformation and strain recovery. *J. Cell. Sci.* 131:jcs209627.

Chapter 5 Deformation of the nucleus against stretch

5.1 Summary of this chapter

In this chapter, the results of the nuclear deformation against circumferential and axial stretches will be shown.

The results will show obvious different nuclear deformation behaviors depending on two stretches. To compare the deformation of AF and nucleus in the same framework, 2D analysis for the nucleus was performed first. Then, to consider the rotation of the nucleus to the direction perpendicular to the 2D plane, 3D analysis was performed. Both 2D and 3D analyses show qualitatively similar results that the nucleus deforms smaller in the axial stretch than the circumferential stretch. But the elongation of both the nuclear longitudinal and transverse axes was smaller in 3D analysis than those in 2D. The difference may be due to the rotation of the nucleus to out of the 2D plane. The physiological significance of the heterogeneous deformation properties the nucleus will be discussed in Chapter 6.

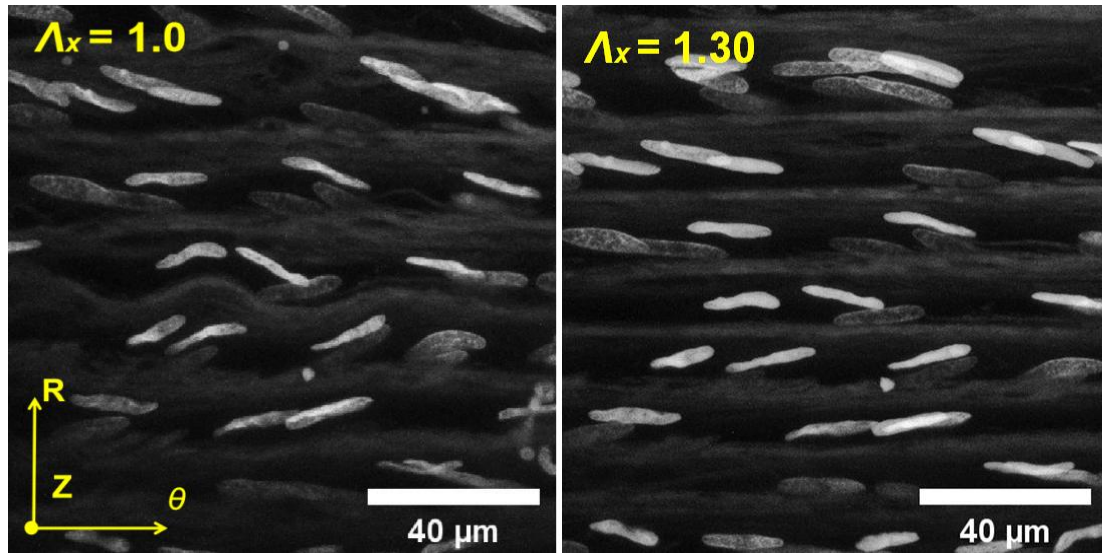
Different from the AF, this chapter will show that the nucleus deformed significantly less than cell body and the AF network for both circumferential and axial stretches. There are two major possible reasons for explaining this: 1) the nucleus is stiffer than the cell body; 2) the nucleus is connected to the cell body through weak and sparse link of AF. The details will also be discussed in Chapter 6.

5.2 Deformation and rotation in 2D

5.2.1 Circumferential stretch

Fig. 5.1 shows a type-1 slice at a macroscopic view. The macroscopic images were used to calculate the macroscopic stretch ratio λ_x . Fig. 5.2 shows a type-1 slice at a microscopic view. The images at microscopic view were used to calculate the deformation of the nucleus.

Fig. 5.3 (a) and (b) show the changes in the nuclear length and width during the circumferential stretch, respectively. The nuclei elongated in their longitudinal direction during circumferential stretch (Fig. 5.3(a)), and their stretch ratios λ_{Nl} ranged from 1.05 to 1.24 with a mean value of 1.14 ± 0.07 ($n = 8$) at $\lambda_x = 1.35$. On the other hand, Fig. 5.3(b) represents that the widths of the nuclei became smaller during the circumferential stretch. The transversal stretch ratios ranged from 0.67 to 0.91 with a mean value of $\lambda_{Nt} = 0.85 \pm 0.08$.



(a) Before stretch

(b) After stretch

Fig. 5.1 Fluorescent images of smooth muscle cell nuclei in aortic tissue slice stretched in θ direction and observed in θ - R plane (Type 1 slice).

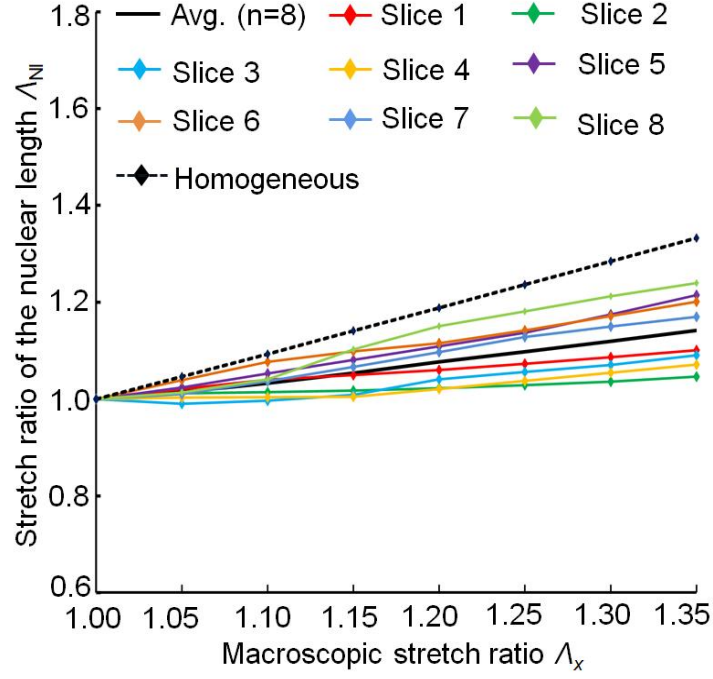


(a) Before stretch

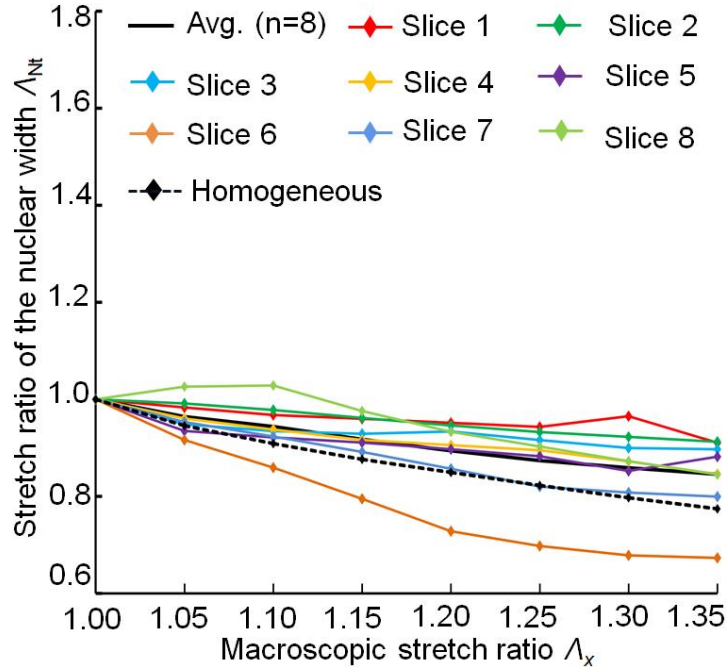


(b) After stretch

Fig. 5.2 Enlarged fluorescent images of smooth muscle cell nuclei in aortic tissue slice stretched in the circumferential direction.



(a) Nuclear length change in circumferential stretch



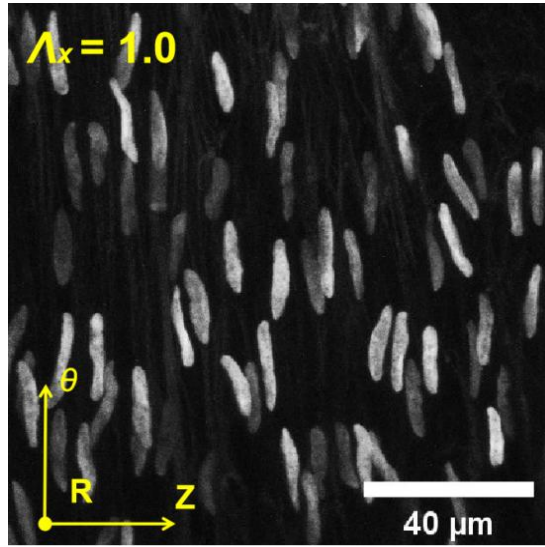
(b) Nuclear width changes in circumferential stretch

Fig. 5.3 Two-dimensional deformations of the nuclear length (a) and width (b) against the circumferential stretch. The stretch ratios were measured in one nucleus per slice.

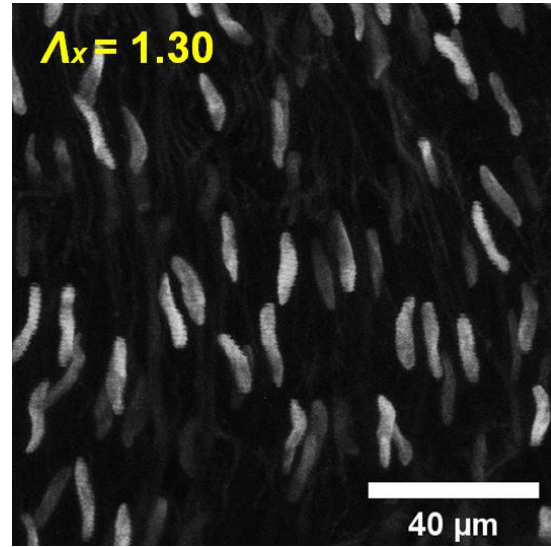
5.2.2 Axial stretch

Typical axial stretching results of the nucleus for type-2 and 3 slices at macroscopic view are shown in Fig. 5.4 and 5.5. The nuclear width did not change so much in the stretch direction. Fig. 5.6 shows the nucleus of the type 2 slice at a microscopic view.

Fig. 5.7(a) and (b) represent the stretch ratios of the length and width of the nuclei against the axial stretch. As shown in Fig. 5.7(a), the nuclear longitudinal axis became slightly shorter during the axial stretch due to the Poisson effect. The stretch ratio of λ_{Nl} ranged from 0.95 to 1.01 with a mean value of 0.98 ± 0.03 ($n = 5$). Fig. 5.7(b) shows that the nuclear width increased slightly during the axial stretch. The λ_{Nt} ranged from 1.02 to 1.1 with a mean value 1.06 ± 0.03 .

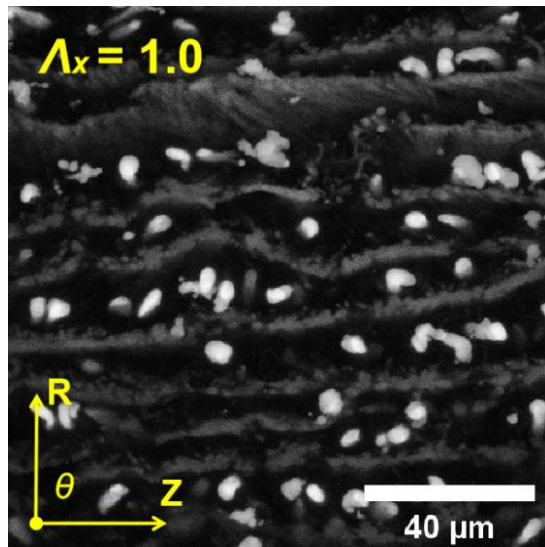


(a) Before stretch

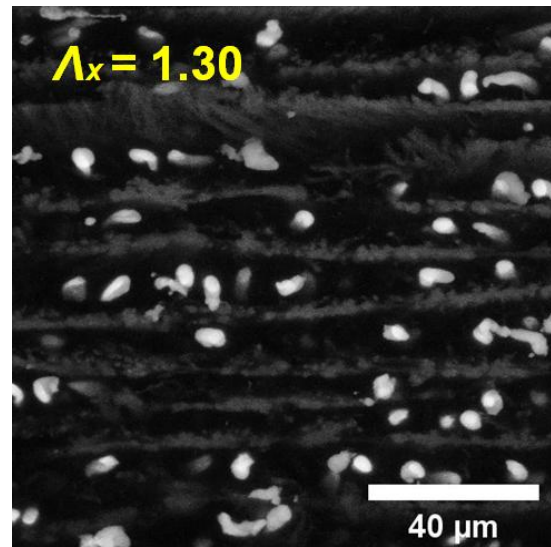


(b) After stretch

Fig. 5.4 Fluorescent images of smooth muscle cell nuclei in aortic tissue slice stretched in axial direction and observed in Z - θ plane (Type 2 specimen).

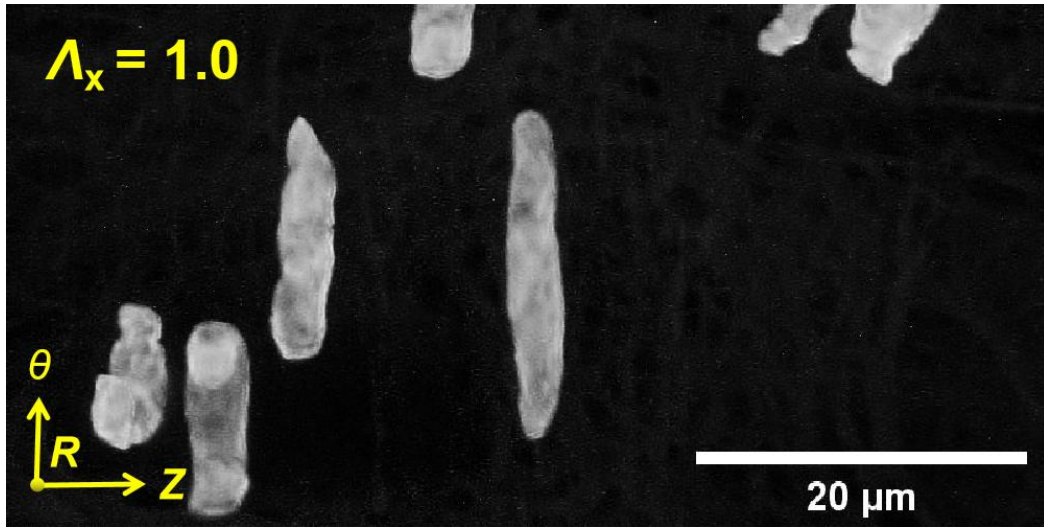


(a) Before stretch

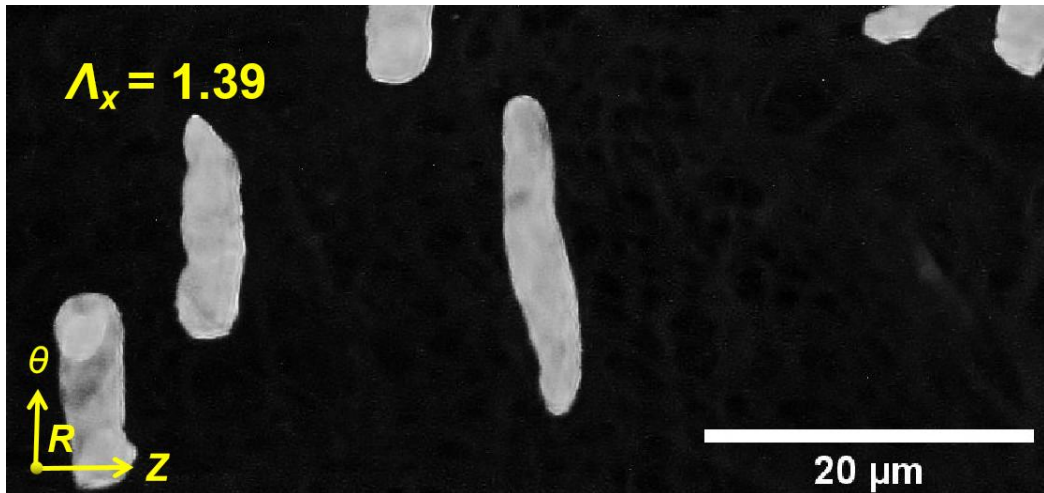


(b) After stretch

Fig. 5.5 Fluorescent images of smooth muscle cell nuclei in aortic tissue slice stretched in axial direction and observed in Z - R plane (Type 3 specimen).

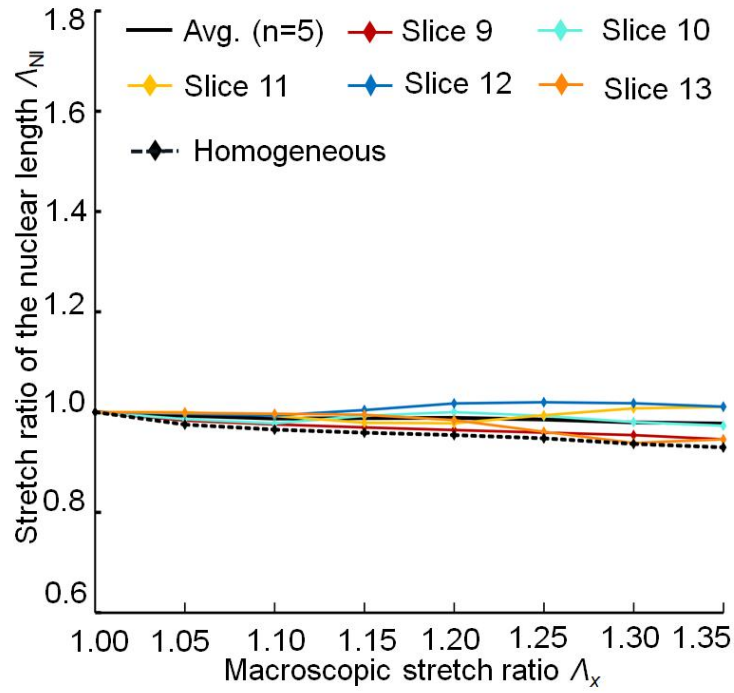


(a) Before stretch

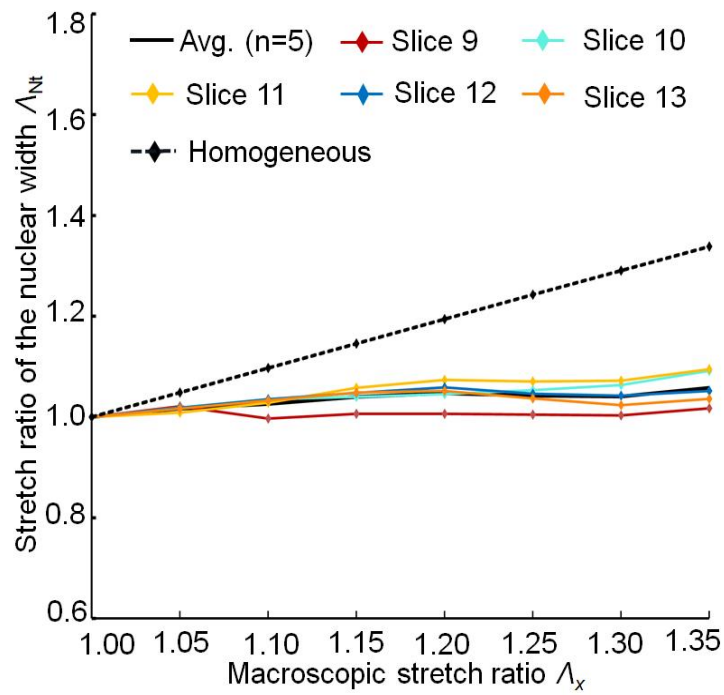


(b) After stretch

Fig. 5.6 Enlarged fluorescent images of smooth muscle cell nuclei in aortic tissue slice stretched in the axial direction (Type 2 specimen).



(a) Nuclear length change in axial stretch



(b) Nuclear width change in axial stretch

Fig. 5.7 Two-dimensional deformations of the nuclear length (a) and width (b) against the circumferential stretch. The stretch ratios were measured in one nucleus per slice.

5.2.3 Measurement of deformation of multiple nuclei in each sample slice

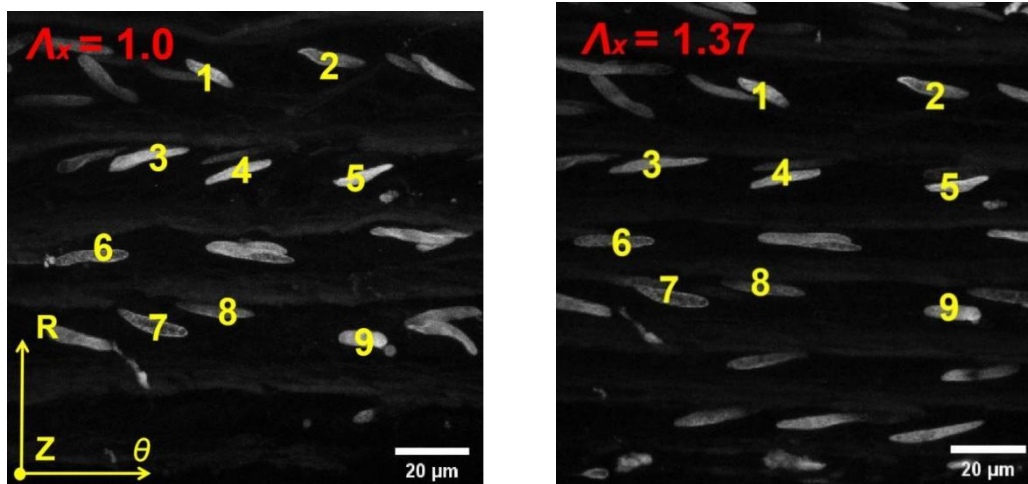
The deformation of multiple nuclei in 6 slices were also measured additionally (3 for the circumferential stretch and 3 for the axial) to evaluate its variability. For each slice, 8–10 nuclei were chosen and their length and width before and after stretching at $\lambda_x = 1.37$ were measured (Tables 5.1 and 5.2). The chosen nuclei for each chosen slice are shown in Figs. 5.8 and 5.9. There was no significant difference among the slices #1–3 and among the slices #4–6. Stretch ratio of the nuclear length in the circumferential stretch (1.097 ± 0.058 , $n=27$ in slices #1–3) was significantly larger than that of the nuclear width in the axial stretch (1.039 ± 0.048 , $n=30$ for slices #4–6) ($P < 0.001$), supporting my conclusion, *i.e.*, SMC nucleus is more deformable when the artery wall is stretched in the circumferential direction.

Table 5.1 Stretch ratio of the nuclear length at $\lambda_x = 1.37$ (circumferential stretch)

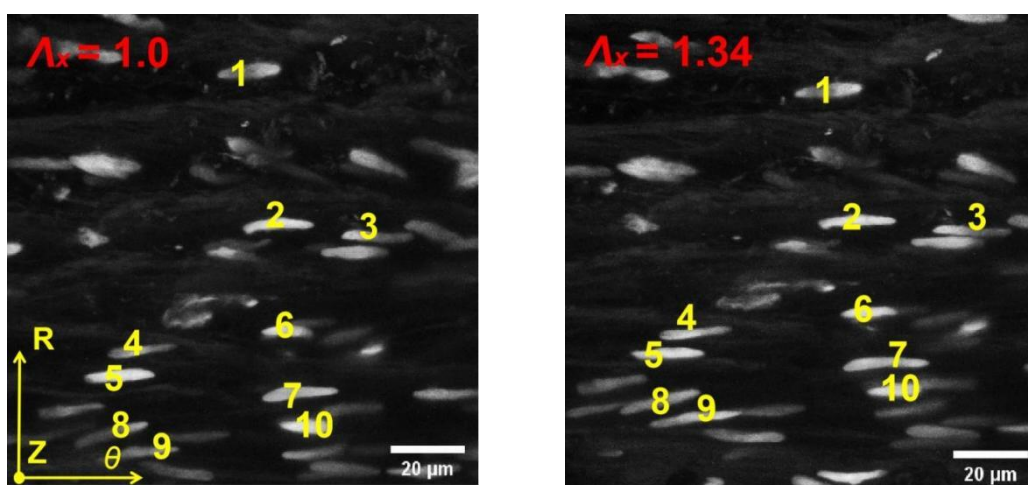
	Nuc.#1	Nuc.#2	Nuc.#3	Nuc.#4	Nuc.#5	Nuc.#6	Nuc.#7	Nuc.#8	Nuc.#9	Nuc.#10	Mean \pm SD
Slice #1	1.070	1.047	1.212	1.020	1.041	1.032	1.065	1.078	1.118	/	1.076 \pm 0.060
Slice #2	1.126	1.110	1.120	1.117	1.045	1.135	1.181	1.119	1.190	1.071	1.122 \pm 0.043
Slice #3	1.006	1.064	1.062	1.091	1.208	1.045	1.070	1.185	/	/	1.091 \pm 0.070

Table 5.2 Stretch ratio of the nuclear width at $\lambda_x = 1.37$ (axial stretch)

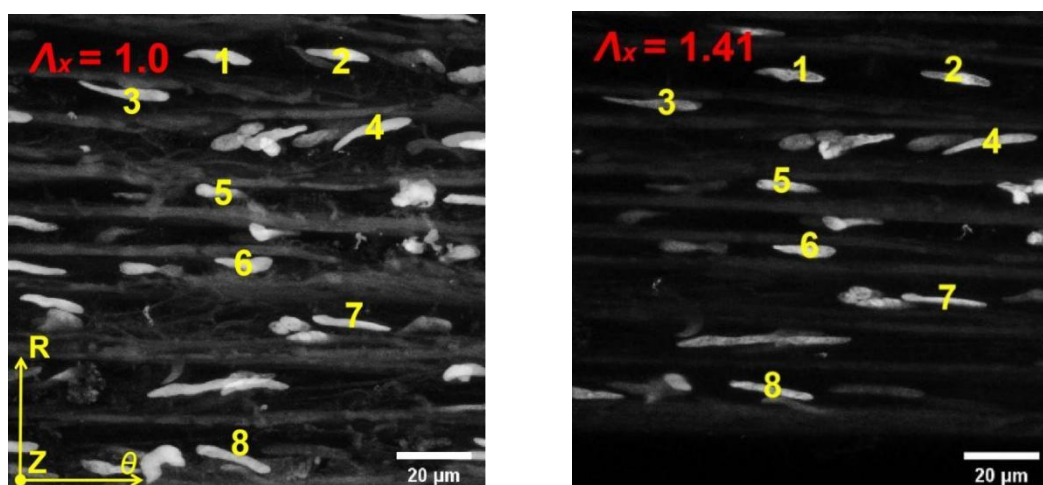
	Nuc.#1	Nuc.#2	Nuc.#3	Nuc.#4	Nuc.#5	Nuc.#6	Nuc.#7	Nuc.#8	Nuc.#9	Nuc.#10	Mean \pm SD
Slice #4	0.933	1.110	0.900	1.116	1.037	1.041	1.111	1.019	1.054	1.015	1.031 \pm 0.074
Slice #5	1.018	1.118	1.053	1.010	1.020	1.020	1.014	1.082	1.012	1.002	1.035 \pm 0.038
Slice #6	1.055	1.049	1.033	1.044	1.049	1.058	1.030	1.045	1.042	1.090	1.050 \pm 0.017



(a) Slice #1 for circumferential stretch, left(before), right (after)

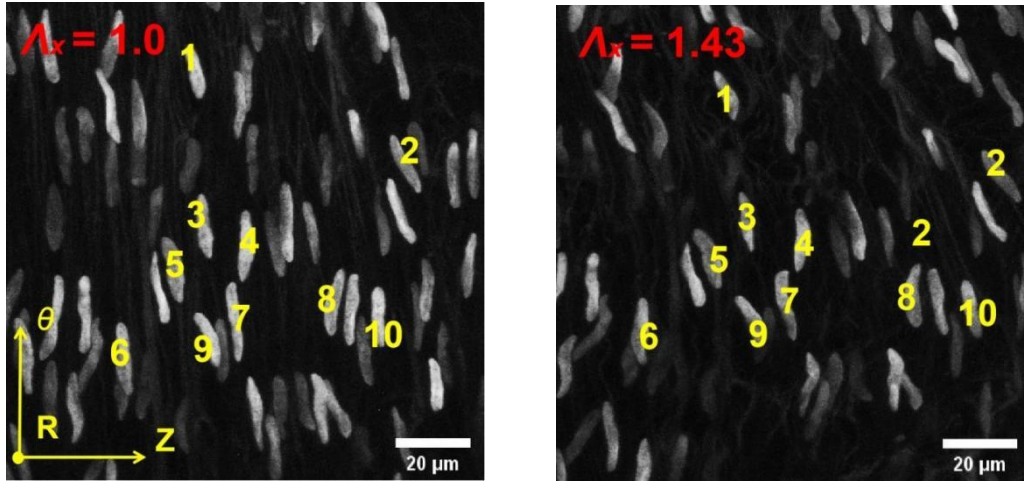


(b) Slice #2 for circumferential stretch, left (before), right (after)

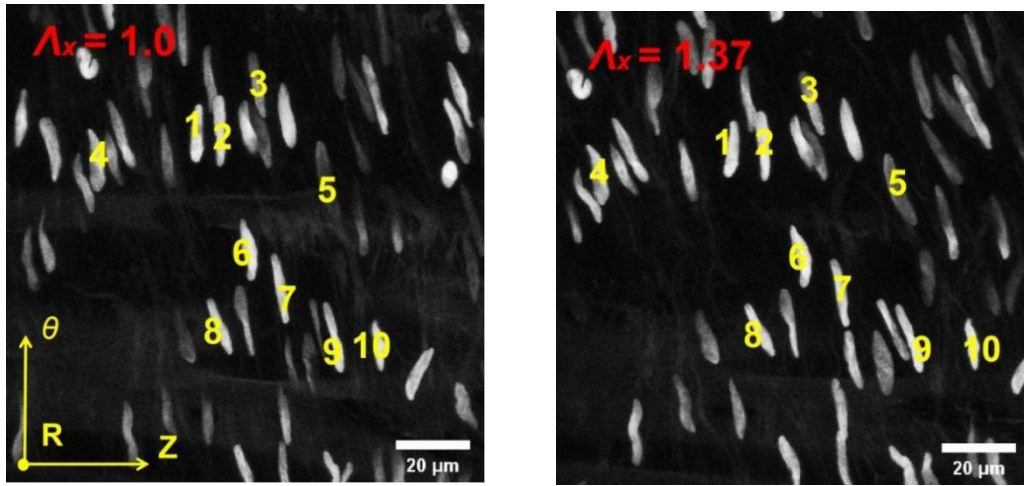


(c) Slice #3 for circumferential stretch, left(before), right (after)

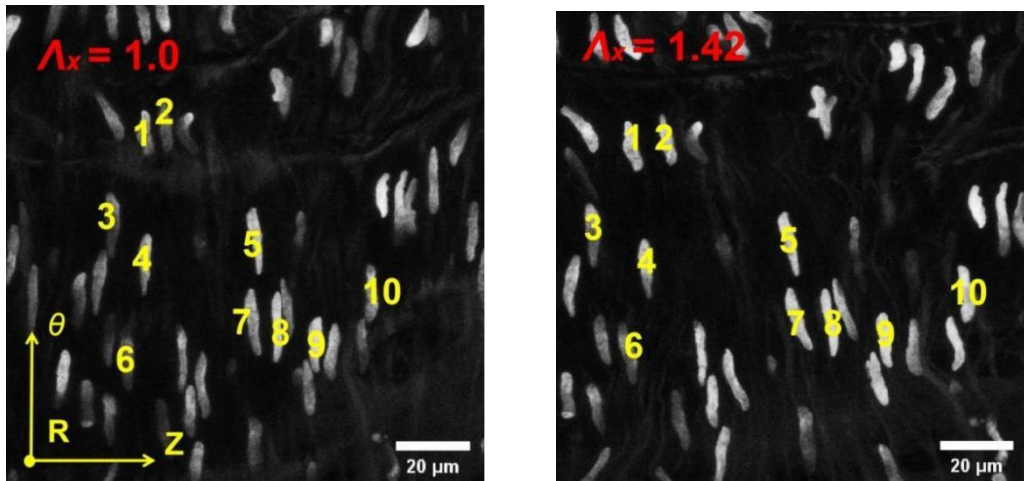
Fig. 5.8 Slices in circumferential stretch for additional measurement.



(a) Slice #4 for axial stretch, left(before), right (after)



(b) Slice #5 for axial stretch, left(before), right (after)



(c) Slice #6 for axial stretch, left(before), right (after)

Fig. 5.9 Slices in axial stretch for additional measurement.

5.2.4 Comparison with the deformation of the homogeneous body

In the circumferential stretch, at $\lambda_x = 1.35$, the homogeneous deformation λ_{NI}^h was 1.33 ± 0.02 . All the longitudinal stretch ratios were smaller than the mean stretch ratio assuming homogeneous deformation (black broken line in Fig. 5.3(a)), and λ_{NI} was significantly smaller than λ_{NI}^h ($P < 0.001$). The homogeneous deformation λ_{Nt}^h was 0.77 ± 0.03 at $\lambda_x = 1.35$. On the other hand, all the transversal stretch ratios except for Slice 6 were larger, *i.e.*, smaller compression, than the mean stretch ratio assuming homogeneous deformation (*id.*), and their difference was close to being statistically significant ($P = 0.057$).

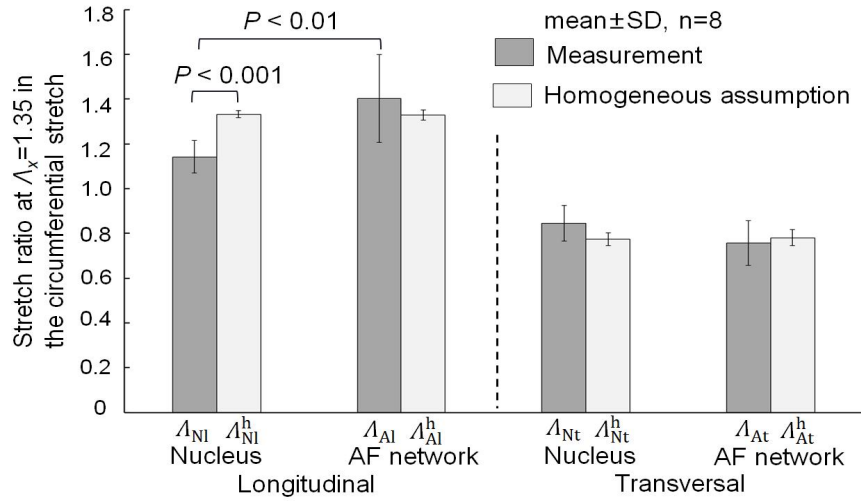
In the axial stretch, the stretch ratio assuming homogeneous deformation λ_{NI}^h was 0.93 ± 0.06 . While the λ_{Nt} is 1.06 ± 0.03 at $\lambda_x = 1.35$, the homogeneous stretch ratio λ_{Nt}^h was much greater ($P < 0.001$) and is 1.34 ± 0.01 at $\lambda_x = 1.35$.

5.2.5 Comparison with the deformation of the AF network

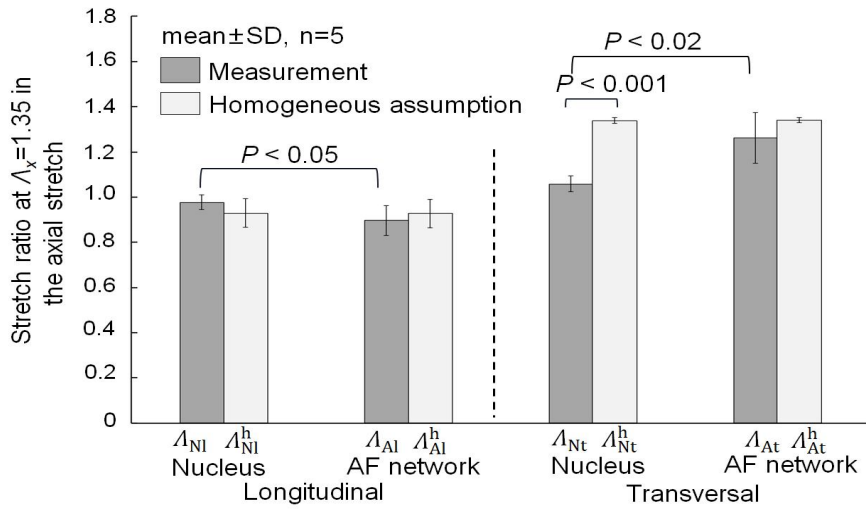
Fig. 5.10(a) and (b) summarize the stretch ratios of the nucleus and the AF network in the circumferential and axial stretch cases, respectively, at $\lambda_x = 1.35$ for measurements and theoretical values assuming homogeneous deformation. Although there was no significant difference between the measurement and homogeneous deformation of the AF, regarding the nucleus, λ_{NI} was smaller than both λ_{AI} ($P < 0.01$) and λ_{NI}^h ($P < 0.001$) in the circumferential stretch case (a) and λ_{Nt} was also smaller than λ_{At} ($P < 0.02$) and λ_{Nt}^h ($P < 0.001$) in the axial stretch case (b), indicating that the nucleus was less deformable than the surrounding tissues. In addition, the nuclear

length increased by 14.2%, which is 42.6% of the homogeneous strain in the circumferential stretch, while nuclear width increased only 5.8%, which is 17.3% of the homogeneous strain in the axial stretch, indicating that the nucleus was hardly stretched in its transversal (width) direction compared to its longitudinal (length) direction.

Fig. 5.10(c) summarizes the mean rotation angles of the nuclei and the AF network against the two stretch cases. For the rotational angle analysis, an absolute value of the $\Delta\theta_N(i)$ or $\Delta\theta_A(i)$ was utilized in Fig. 5.10(c). In the circumferential stretch, the value of $\Delta\theta_A$ was significantly greater than that of $\Delta\theta_N$ ($P < 0.02$) in the circumferential stretch case, whereas there was no significant change between $\Delta\theta_A$ and $\Delta\theta_N$ ($P = 0.34$) in the axial stretch case. The results indicated that the AF network exhibited a larger rotation than the nucleus against the circumferential stretch, whereas they showed similar rotational angles against the axial stretch. No significant differences were observed between the measurement and homogeneous values for both the nuclei and the AF in both stretch cases, possibly for large SD values.

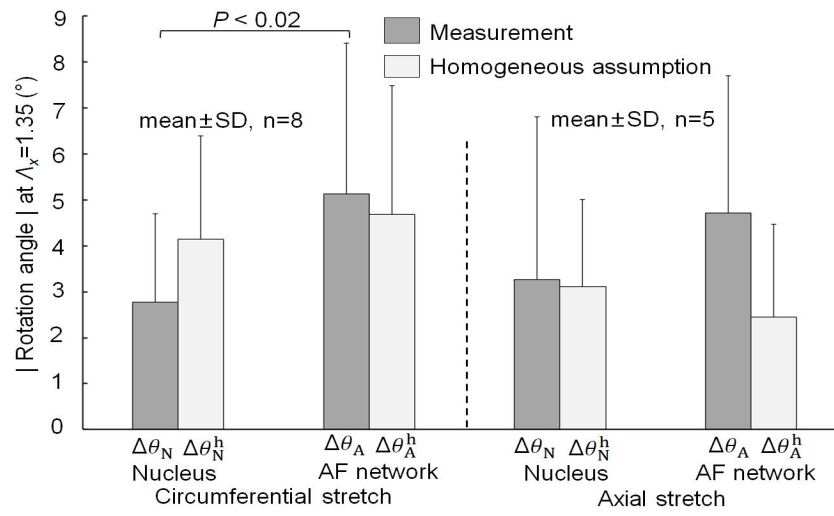


(a) Stretch ratios in circumferential stretch



(b) Stretch ratios in axial stretch

Fig. 5.10 Summary of deformations of the nuclei and AF network against circumferential and axial stretches. Difference between the nucleus and AF network as well as actual deformations measured in the experiment and deformations calculated from homogeneous assumption are compared. Statistical difference was evaluated using paired Student's t-test in the left four data and the right four data separately.



(c) Rotation angles in circumferential and axial stretches

Fig. 5.10 (Continued).

5.3 Deformation and rotation in 3D

5.3.1 Nuclear deformation in the circumferential and axial stretch

Examples of 3D reconstruction of the nuclei are shown in Fig. 5.11. Using Imaris software, the 3D nuclei was reconstructed by stacking 2D images of the nuclei at every stretch step under the circumferential and axial stretches.

Fig. 5.12(a) and (b) show the stretch ratios of the nuclear longitudinal axis A_{Nl} in the circumferential stretch and those in the nuclear transverse axis A_{Nt} in the axial stretch, respectively. Nucleus d in (a) and nucleus l in (b) showed an irregular length change. Detailed observation result revealed that these nuclei bent during the stretch process for unknown reasons, and it was omitted from the further analysis. In 3D analysis, A_{Nl} at $A_x = 1.35$ in the circumferential stretch was 1.088 ± 0.070 ($n = 7$) while A_{Nt} at $A_x = 1.35$ in axial stretch was 1.005 ± 0.032 ($n = 7$). A_{Nt} was significantly smaller than A_{Nl} ($P < 0.05$), indicating that the nucleus was deformed less in the axial stretch as in the 2D analysis. To compare 2D and 3D analyses, the average stretch ratio lines in Figs. 5.3, 5.7 and 5.12 were fitted to the straight lines. Against the circumferential stretch, the slope of the fitted line of nuclear length for the 3D analysis in Fig. 5.12(a) was 0.242, *i.e.*, the deformation of the nucleus was 24.2% of the homogeneous deformation. The deformation of the nucleus in 3D analysis was 58.6% of the nuclear deformation in 2D analysis as the slope of the fitted line of nuclear length was 0.414 in Fig. 5.3(a). On the other hand, against the axial stretch, the slope of the fitted line of the nuclear width was 0.055 for the 3D analysis (Fig.

5.12 (b)), *i.e.*, the deformation of the nucleus was 5.5% of the homogeneous deformation for the 3D analysis (Fig. 5.12(b)). The deformation of the nucleus in 3D analysis was 39.2% of the nuclear deformation in 2D analysis as the slope of the fitted line of nuclear length was 0.139 in Fig. 5.7(b). The nuclear deformation was smaller in the 3D analysis than in the 2D analysis.

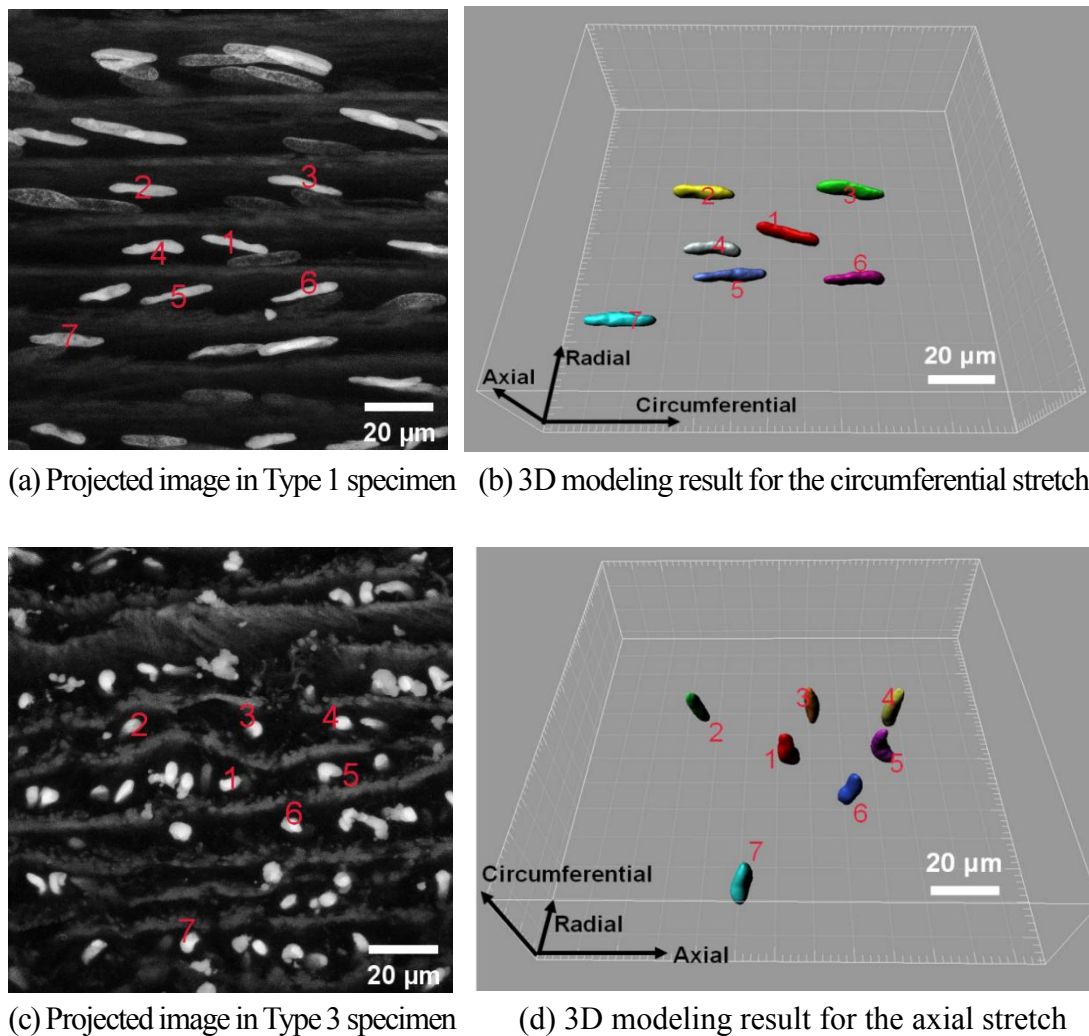
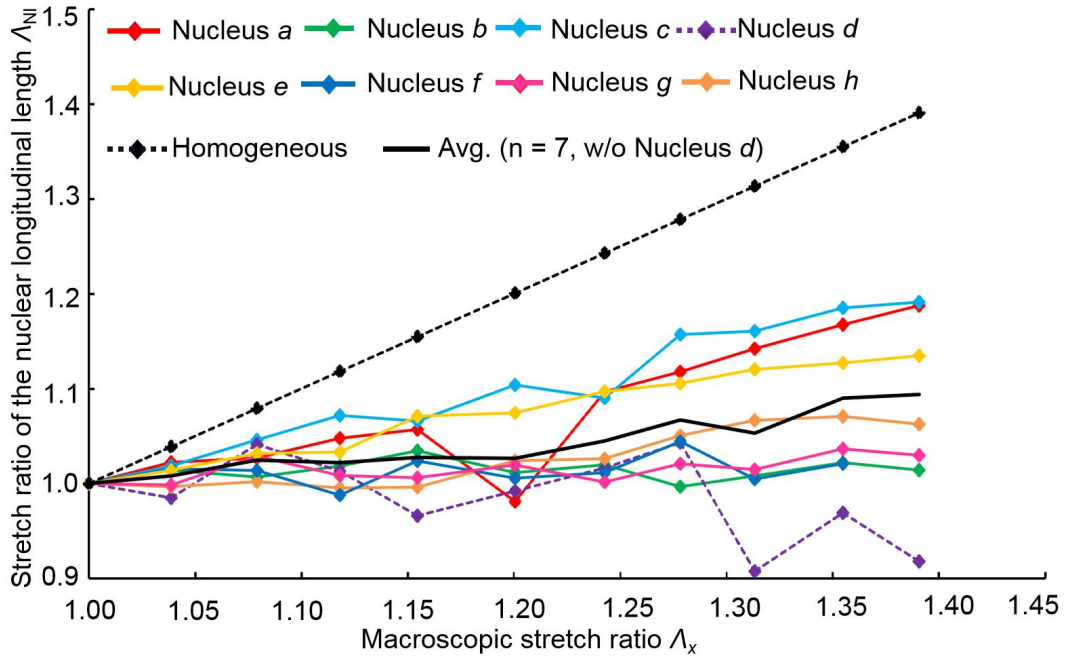
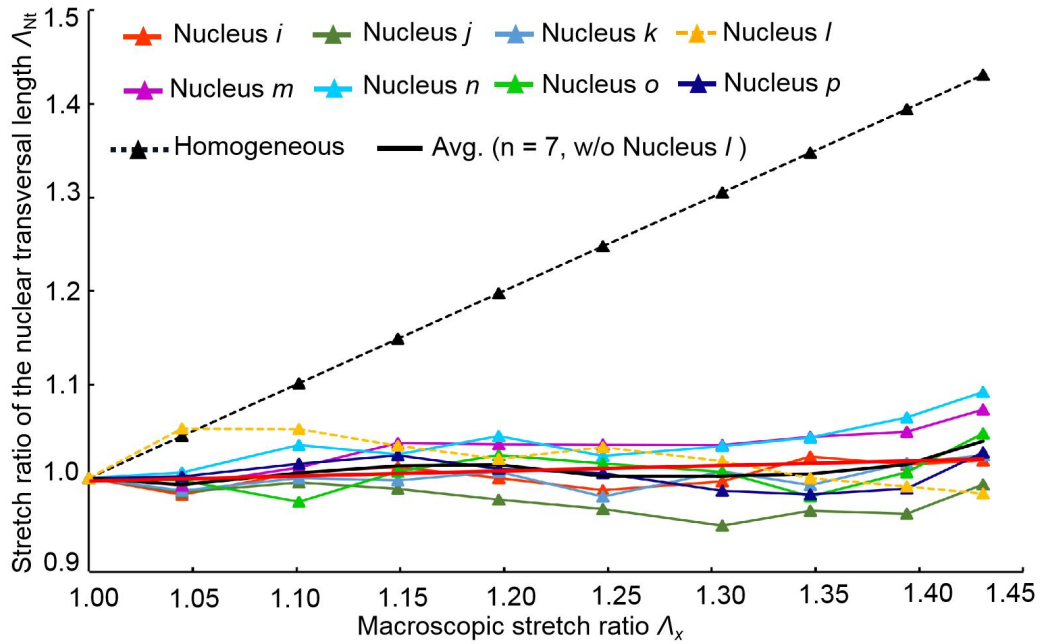


Fig. 5.11 Three-dimensional modeling of the smooth muscle cell nuclei reconstructed from a stack of images. Stack of 2D images taken in Type 1 specimen (a) was used for 3D reconstruction (b) for circumferential stretch. Stack of 2D images taken in Type 3 specimen (c) was used for 3D reconstruction (d) for axial stretch.



(a) Elongation of the longitudinal axis in response to circumferential stretch

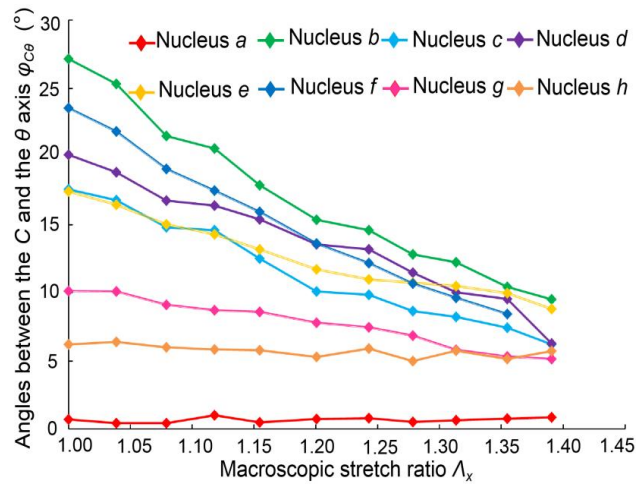


(b) Elongation of the transversal axis in response to axial stretch

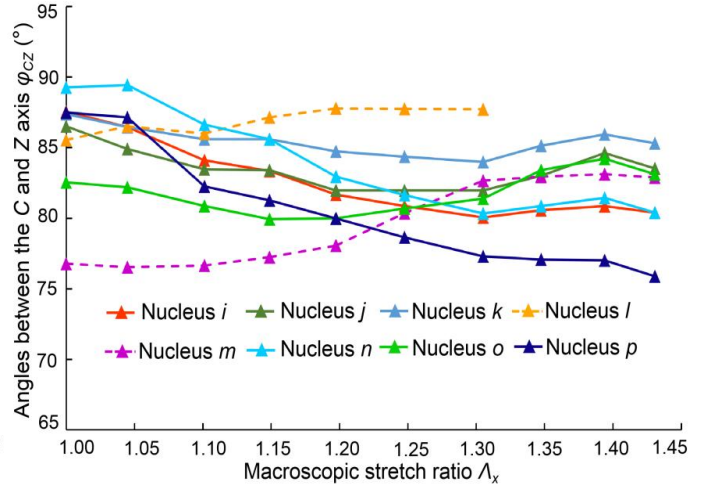
Fig. 5.12 Three-dimensional deformation of the smooth muscle nuclei in the circumferential (a) and axial (b) stretches. Elongation of the longitudinal axis of the nucleus was measured against the circumferential stretch (a) while that of the transversal axes was measured against the axial stretch (b). Nuclei d and l were omitted from the analysis because they were bent during stretch.

5.3.2 Orientation angle change of the nucleus

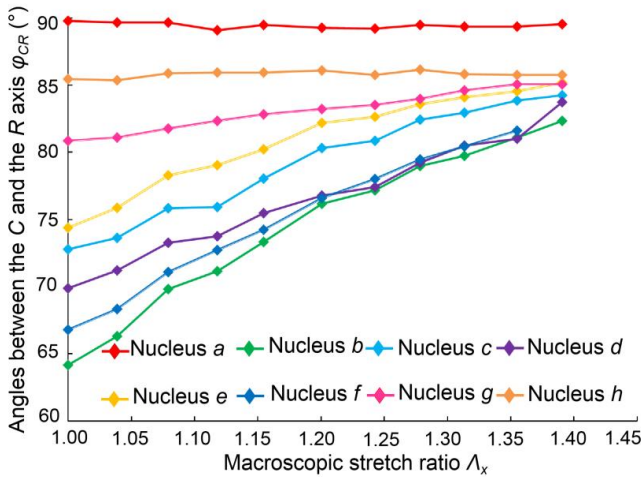
Fig. 5.13 shows the 3D nuclear orientation against circumferential and axial stretch cases. It described the angles between the nuclear longitudinal axis C and the three axes (θ , R , Z) of Cartesian coordinates. In the circumferential stretch, $\varphi_{C\theta}$ decreased from $15.4 \pm 9.0^\circ$ to $7.1 \pm 3.3^\circ$, with a decrease of $8.2 \pm 6.1^\circ$ ($n = 8$) ($P < 0.01$) (a). On the other hand, φ_{CR} increased from $75.5 \pm 9.1^\circ$ to $84.0 \pm 2.8^\circ$, with a decrease of $9.0 \pm 6.5^\circ$ ($P < 0.01$) (c). Although both $\varphi_{C\theta}$ and φ_{CR} altered significantly, φ_{CZ} did not exhibit the significant change in response to the circumferential stretch at $A_x = 1.35$ (e). The results indicate that the nuclei with various orientation angles at no load state rotated mostly in the θ – R plane to align in a uniform direction close to the circumferential axis. The change in nuclear orientation was not significant in the axial stretch when all the data were considered. Since the nucleus m tended to exhibit the reverse change and the data was partly missing for the nucleus l , the analysis was continued without considering these two cases for $A_x = 1.35$. φ_{CZ} decreased slightly from $86.8 \pm 2.3^\circ$ to $81.7 \pm 2.8^\circ$, with a decrease of $5.1 \pm 0.5^\circ$ ($n = 6$) ($P < 0.05$) (b), and φ_{CR} from $82.3 \pm 5.3^\circ$ to $79.2 \pm 7.5^\circ$, with a decrease of $3.1 \pm 2.2^\circ$ ($P < 0.05$) (d). $\varphi_{C\theta}$ increased from $9.0 \pm 4.7^\circ$ to $15.9 \pm 6.7^\circ$, with an increase of $6.9 \pm 2.0^\circ$ ($P < 0.01$) (f). Although most of the nuclei rotate similarly in each axis, no alignment to a uniform direction was observed in the axial stretch.



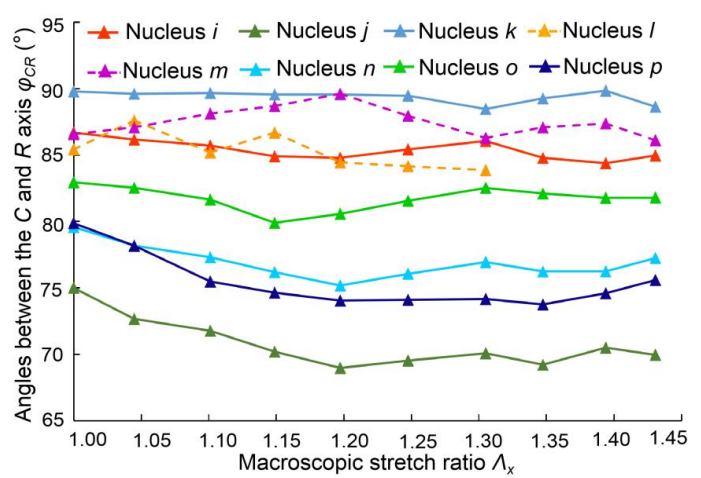
(a) To stretch direction (θ)



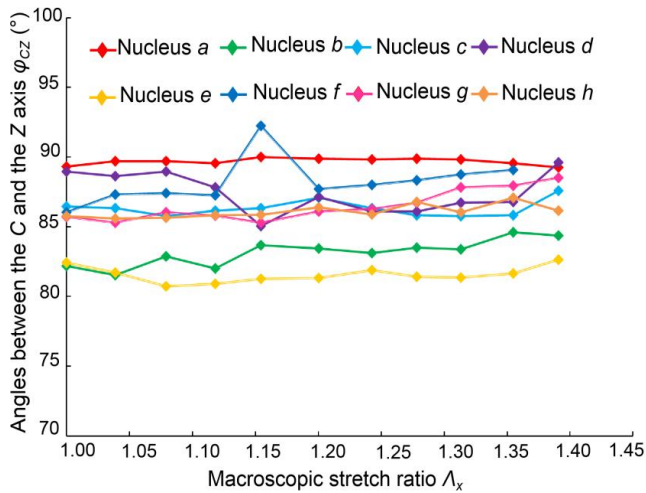
(b) To stretch direction (Z)



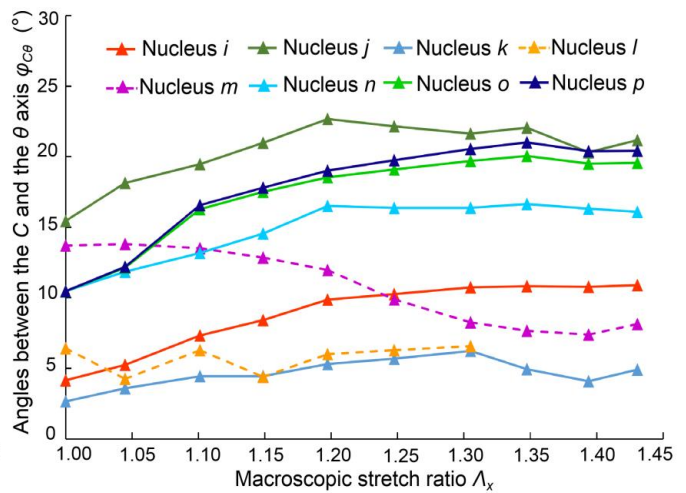
(c) To perpendicular-to-stretch direction (R)



(d) To perpendicular-to-stretch direction (R)



(e) To another perpendicular-to-stretch direction (Z)



(f) To another perpendicular-to-stretch direction (θ)

Fig. 5.13 Rotations of the smooth muscle cell nucleus in the circumferential (a), (c), (e) and axial (b), (d), (f) stretches. Angles between the longitudinal axis of the nucleus C and the circumferential θ , radial R, or axial Z directions are depicted.

5.3.3 Comparison between 3D and 2D results

The nucleus was found to be elongated more when stretched in its longitudinal direction than in its transverse direction in the 2D analysis. The elongation of nuclear longitudinal axis in the circumferential stretch was $14.2 \pm 7.3\%$ which was 2.4 times higher than that of nuclear transversal axis in the axial stretch ($5.8 \pm 3.4\%$) at $\Lambda_x=1.35$ (Fig. 5.10). It indicates that nucleus is more elongated and sensitive to the circumferential stimulation as it is reported in the previous study (Fan et al., 2019). Similar results were obtained from the 3D analysis (Fig. 5.12), but the deformations as well as their variations were much smaller than the 2D analysis. As described in Section 5.3.1, the elongation of the nuclear length in the 3D analysis was 58.6 % of the 2D analysis, while the broadening of the nuclear width in the 3D analysis was 39.2 % of the 2D analysis. Larger values were obtained in the 2D analysis than 3D analysis.

5.4 Discussion

The morphology of the SMC nucleus changed differently against the circumferential and axial stretches. The nuclei became longer against the circumferential stretch, whereas they became wider in the axial stretch.

In either circumferential or axial stretch case, the stretch ratio of the AF is larger than the nuclei. Deformation of the AF network was not significantly different from the theoretical deformation of the homogeneous materials in any deformation conditions shown in Figs. 4.3 and 4.6, although the variations among the slices were large. This may indicate that the AF network deforms similarly to the whole tissue. In contrast, the deformation of the nucleus was generally smaller than the homogeneous deformation as shown in Figs. 5.3 and 5.7. The average of the measured strain, *i.e.*, $\lambda - 1$, was about 43%, 68%, 33%, and 17% of the homogeneous strain for Figs. 5.3(a), 5.3(b), 5.7(a), and 5.7(d), respectively. These results may indicate that the nucleus is stiffer than its peripheral tissue or that the connection between the nucleus and the peripheral tissue is weak.

When a material is stretched in one direction, it shrinks in the direction perpendicular to the stretch direction due to the Poisson effect. This happened both in the nucleus and AF network. When stretched in the circumferential direction, the nuclei (Fig. 5.3(b)) and AF network (Fig. 4.3(b)) shrunk almost similarly to that of homogeneous body, and there was no significant difference among λ_{Nt} , λ_{At} , λ_{Nt}^h , and λ_{At}^h at $\lambda_x = 1.35$ (Fig. 5.10(a)). While in the axial stretch, the AF network shrunk almost similarly to the homogeneous body (Fig. 4.6(a)), but the nuclei shrunk much

less than that of the homogeneous body (Fig. 5.7(a)). As a result, A_{NI} was significantly larger ($P < 0.05$) than A_{AI} at $A_x = 1.35$ (Fig. 5.10(b)). This may indicate that the nucleus is not subjected to the compressive force in the longitudinal direction of the cell.

Larger values obtained in the 2D analysis may be caused by the rotation of the nucleus during stretch (Fig. 5.13). For example, the longitudinal axis of the nucleus rotated mostly in the θ - R plane. Rotation was larger in the nucleus with higher $\varphi_{C\theta}$, and the largest rotation was obtained in the nucleus *b* which rotated from $\varphi_{C\theta} = 27^\circ$ to 10° (a). This rotation corresponds to 10% elongation in the 2D analysis. The wide variation of the elongation is caused by the variation of $\varphi_{C\theta}$ before stretch. Thus, the difference between 2D and 3D results can be explained by the rotation of the nucleus. It also implies that 3D analysis is necessary to understand the deformation of the nucleus in response to the mechanical stretch. The 3D analysis showed that the longitudinal deformation of the nucleus against the circumferential stretch of the tissue was 18 times higher than its transversal deformation against the axial stretch, indicating that the relative insensitivity of the nucleus in the axial stretch is much higher than one estimated from the 2D analysis.

The relatively small deformation of the nuclei might also be caused by shrinking of their image due to photobleaching. The time lapse photobleach test was performed to simulate the stretch test, and found that the deviation caused by the photobleach was less than 0.5% ($n = 4$, $P < 0.05$) within 1.5 h. Hence, the effect of photobleach is thought to be minimal.

Reference

Fan Y, Wang JF, Maeda E, Murase K, Matsumoto T (2019) Analysis of heterogeneous deformation in the wall of rabbit thoracic aorta at microscopic level. *Adv. Biomed. Eng.* 8:7–13.

Chapter 6 Discussion

6.1 Possible causes of the difference in the strain between the nucleus and entire cell

According to the results, in both stretch cases, deformation of AF was not significantly different from the entire cell, while nuclear deformation was smaller than AF or the cell body. Why is the nuclear deformation smaller than the tissue deformation? One of the possible reasons might be that the nucleus is stiffer than the rest of the cell. In 2002, Caille et al. reported that the elastic modulus of the nucleus is 10 times higher than that of the cytoplasm (Caille et al. 2002). Since then, there have been many studies on the mechanical properties of the nucleus, and it has been reported that the Young's modulus of the nucleus varies with conditions such as cell types (Li et al. 2015; Zhou et al. 2018), pathological states (Li et al. 2015; Wang et al. 2018; Fischer et al. 2020), activity of the myosin (Martens et al. 2008), and the experiment conditions (Rowat et al. 2006; Zhou et al. 2018). However, no conclusive results have been obtained especially for the nucleus of the cells in the tissues.

In addition to their difference in Young's modulus, another possible explanation might be that the connection between the nucleus and cell body is sparse and weak, which may cause smaller deformation of the nucleus than the cell body.

6.2 Difference in the mechanical properties of the nucleus and cell body cannot explain the difference in strain

To evaluate the effects of higher stiffness of the nucleus, deformations of the cell and the nucleus were estimated with a simple cylindrical model (Fig.6.1).

Let us assume that the cell body is a cylinder with the length L_0 , radius R_0 , and Young's modulus E_C , and the nucleus a cylinder with the length l_0 , radius r_0 , and Young's modulus E_N , located at the center of the cell body (Fig.6.1), the cell consists of three parts marked with I, II, and III, and the parts I and III are symmetrical to the part II. When the cell is stretched by the force F , the lengths of the cell and the nucleus become L and l , respectively, the nucleus and the cell body in the part II bear force F_N and F_C , respectively, and no shear deformation occurs during stretch and stresses are nominal for simplicity.

For the cell body part I (= part III):

$$F = \pi \cdot R_0^2 \cdot \sigma_{C\ I} \quad (6.1)$$

$$\sigma_{C\ I} = E_C \cdot \varepsilon_{C\ I}, \quad (6.2)$$

$$\varepsilon_{C\ I} = \frac{(L-l)/2 - (L_0-l_0)/2}{(L_0-l_0)/2}, \quad (6.3)$$

where σ_C and $\varepsilon_{C\ I}$ represent the stress and strain of the cell body, respectively.

For the nucleus in part II :

$$F_N = \pi \cdot r_0^2 \cdot \sigma_N \quad (6.4)$$

$$\sigma_N = E_N \cdot \varepsilon_N \quad (6.5)$$

$$\varepsilon_N = \frac{l-l_0}{l_0} \quad (6.6)$$

where σ_N and ε_N represent the stress and strain of the nucleus, respectively.

For the cell body in part II :

$$F_C = \pi \cdot (R_0^2 - r_0^2) \cdot \sigma_{CII} \quad (6.7)$$

$$\sigma_{CII} = E_C \cdot \varepsilon_{CII} \quad (6.8)$$

$$\varepsilon_{CII} = \frac{l-l_0}{l_0} \quad (6.9)$$

where σ_{CII} and ε_{CII} represent the stress and strain of the cell body in part II , respectively.

From the balance of forces, I obtain

$$F = F_C + F_N. \quad (6.10)$$

From Eqs.6.1–6.10, I obtain

$$R_0^2 \cdot E_C \cdot \frac{(L-l)-(L_0-l_0)}{(L_0-l_0)} = r_0^2 \cdot E_N \cdot \varepsilon_N + (R_0^2 - r_0^2) \cdot E_C \cdot \varepsilon_N. \quad (6.11)$$

Strain of the whole cell is expressed as

$$\varepsilon_{all} = \frac{L-L_0}{L_0}. \quad (6.12)$$

If we assume the Young's modulus of the nucleus is k times higher than that of the cell body,

$$E_N = k \cdot E_c \quad (k > 1). \quad (6.13)$$

Relative strain of the nucleus to the whole cell is obtained by taking Eqs.6.6, 6.13 into Eq.6.11 to eliminate L and l , respectively, and by using Eq.6.13,

$$\frac{\varepsilon_N}{\varepsilon_{all}} = \frac{L_0 R_0^2}{L_0 R_0^2 + (L_0 - l_0) r_0^2 (k-1)} \quad (6.14)$$

Roughly speaking,

$$r_0 = 0.3 R_0 \text{ and } l_0 = 0.3 L_0. \quad (6.15)$$

We thus obtain

$$\frac{\varepsilon_N}{\varepsilon_{all}} = \frac{1}{1+0.063(k-1)} . \quad (6.16)$$

This equation indicates the relative strain of the nucleus decrease only slightly with an increase in the Young's modulus of the nucleus. This equation indicates the relative strain of the nucleus decrease only slightly with an increase in the Young's modulus of the nucleus. For example, the nuclear strain is 94%, 80%, and 64% of the whole cell strain even if the nucleus is stiffer than the rest of the cell by 2, 5, and 10 times, respectively.

In the 3D analysis, the deformation of the nucleus was only 24.2% and 5.5% of the homogeneous deformation in the circumferential and axial stretch, respectively, as described in the section 5.3. To attain such small deformations ($\frac{\varepsilon_N}{\varepsilon_{all}} = 24.2\%$ and 5.5%), the nucleus needs to be extraordinary stiffer ($k = 51$ and 274 , respectively) than the rest of the cell according to Eq.6.16, which is hard to imagine. Thus, it is difficult to explain the very small deformation of the nucleus when the artery wall is stretched in the axial direction with the difference in the elastic modulus of the nucleus and the whole cell. It is difficult to explain the anisotropic response of the nucleus with this model, either.

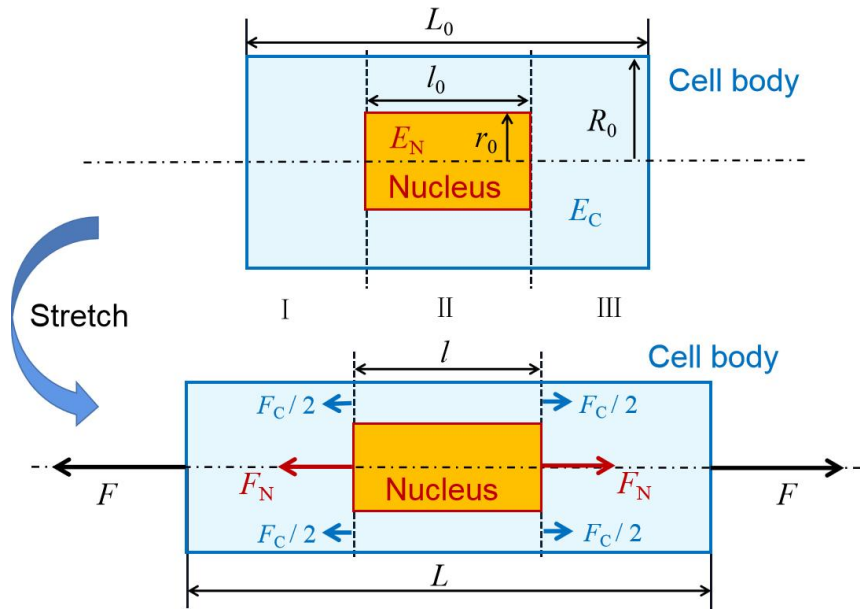


Fig. 6.1 A simple cylindrical cell model estimating the difference in strain between the cell body and the nucleus. Force applied to the cell body in the part II is F_C in total, but was divided into two $F_C/2$ s for 2D drawing.

6.3 Anisotropic nuclear deformation against different stretches:

Qualitative explanation

The anisotropic deformation of the nucleus might be because the nucleus is connected to the outside of the cell anisotropically. According to my observation results in chapter 4 and 5, the nuclei are aligned in the vascular circumferential direction, the AFs align mostly in the longitudinal direction of the cells. A simple and novel cell model of the nucleus and the AFs (Fig.6.2) is proposed, which enables to explain the anisotropic response of the nuclear deformation. When the cell is stretched in its longitudinal direction, the nucleus is also easily stretched via the AFs (Fig.6.2 lower half). On the other hand, while the cell is stretched in its transversal direction, the nucleus is not stretched efficiently because the stretch direction is perpendicular to the direction of the AFs (Fig.6.2 upper half).

To estimate the connection between the AF network and nucleus, changes in the width of the actin bundles adjacent to the nucleus were measured at three positions along the nucleus in specimen type 2 as shown in Fig.6.3. Actin bundle boundaries (orange lines) were identified manually and the distance between the boundaries was measured at three positions. Stretch ratios in response to the axial stretch are summarized in Table 6.1. The stretch ratio measured at the center of the nucleus was significantly smaller than the average measured at both sides, indicating the lateral connection between the nucleus and the actin filament bundle. The result revealed that the distance between the AFs increased more in the region where the nucleus is absent

than at the central region attached to the nucleus. This may also support the model in Fig.6.2.

Anisotropic nuclear deformation against different stretches may also raise an important issue in the measurement of the mechanical properties of the nucleus. The present results indicate that nuclear deformation is highly dependent on the alignment of the actin filaments. Thus, it is necessary to reevaluate the reported elastic modulus of the nucleus considering the alignment of actin filament.

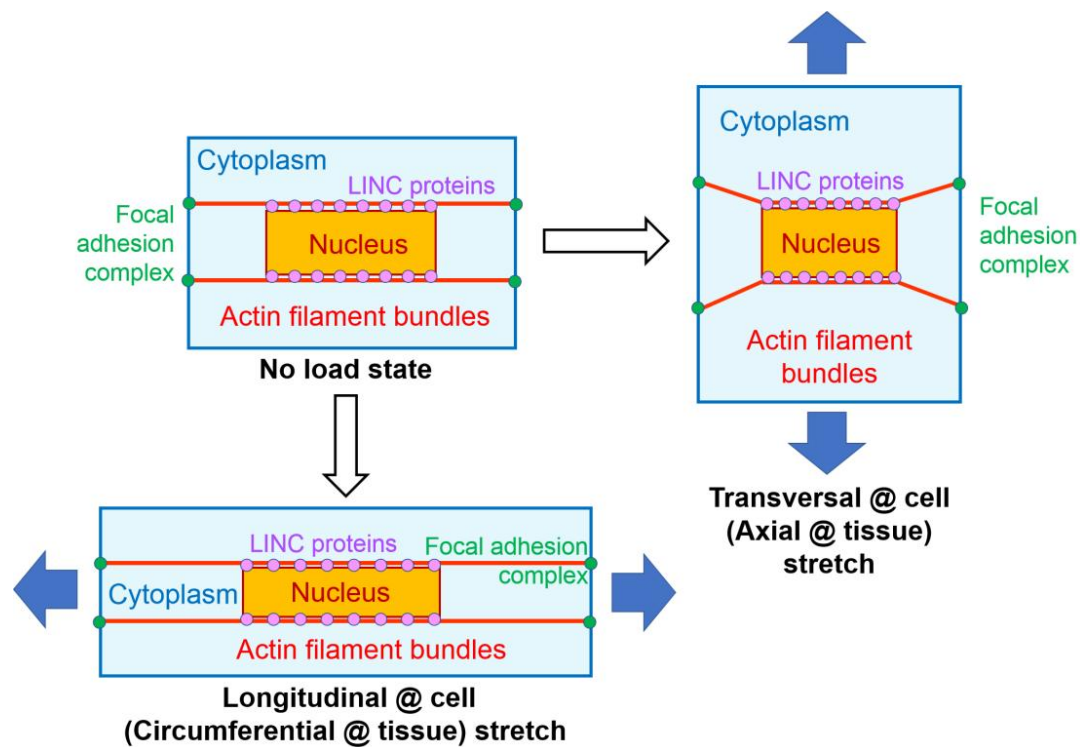
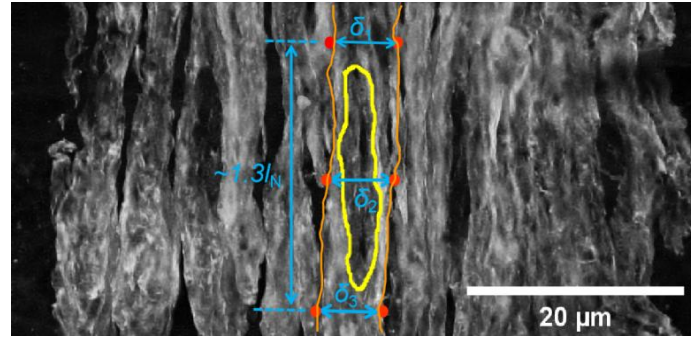
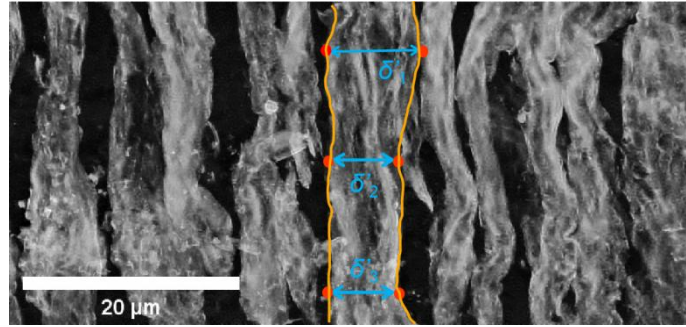


Fig. 6.2 A novel simplified model of a cell explaining anisotropic response of the nuclear deformation against mechanical stretching.



(a) $\Lambda_x = 1.0$



(b) $\Lambda_x = 1.39$

Fig. 6.3 Change in the width of actin bundles at the upper, central and lower positions of the nucleus before (a) and after stretch (b) in the axial direction.

Table 6.1 Stretch ratios measured at the blue lines in Fig.6.3.

Sample	(δ'_1/δ_1)	(δ'_2/δ_2)	(δ'_3/δ_3)	$[(\delta'_1/\delta_1) + (\delta'_3/\delta_3)]/2$
A	1.144	1.051	1.406	1.275
B	1.206	1.130	1.390	1.298
C	1.441	1.191	1.209	1.325
D	1.155	1.084	1.229	1.192
Mean \pm SD	1.237 ± 0.139	1.114 ± 0.061	1.309 ± 0.104	$1.273 \pm 0.06^*$

* $P < 0.01$ vs (δ'_2/δ_2) .

6.4 Anisotropic nuclear deformation against different stretches:

Quantitative analysis

Next, the issue focuses on quantitatively illustrating the smaller deformation of the nucleus in the axial stretch with a model. Although the model in Fig.6.2 can illustrate the circumferential and axial stretch cases separately and qualitatively, it is still a two-dimensional model without considering the initial orientation angle of the nucleus and AF in the θ - R plane.

Based on the observation, a simple three-dimensional model of a smooth muscle cell sandwiched with a pair of elastic lamellas, i.e., lamellar unit (Fig. 6.4) has been proposed, and the deformation of the nucleus in response to stretch in the circumferential, θ , and the axial, Z , directions have been calculated. This model can explain the difference between the circumferential and axial stretch cases at the same time.

The model consists of a cuboid cell body in which a cuboid nucleus is placed obliquely with an angle α_0 at its center. The nucleus is connected to the cell membrane with four identical AFs aligned in parallel to the nucleus. The cell body as well as the nucleus are assumed to be incompressible, homogenous, and isotropic. The no-load length, width, and height are L_{N0} , W_{N0} , and H_{N0} , respectively, for the nucleus, and L_{C0} , $3W_{N0}$, and $3H_{N0}$, respectively for the cell body. The length of the actin filaments was L_{A0} for the no-load state. The stiffness of the nucleus and each actin filament was assumed to be K_N and K_A , respectively.

Circumferential stretch case

In the circumferential stretch case, the model was projected to the R - θ plane (Fig. 6.5). The nucleus is connected to the cell body with two AFs for each side. Subscripts of dimensions change from 0 to 1 in response to the circumferential stretch. To meet the condition of my experiment, the cell body was assumed to be stretched 1.35 times the original length in the longitudinal direction. So, the stretch ratio of the cell body in the circumferential stretch λ_{Cl} is

$$\lambda_{Cl} = \frac{L_{C1}}{L_{C0}} = 1.35. \quad (6.17)$$

Because the cell body is incompressible and isotropic,

$$W_{C1} = W_{C0} \lambda_{ct} = W_{C0} \sqrt{\frac{1}{\lambda_{cl}}}, \quad (6.18)$$

where λ_{ct} is the stretch ratio of the width of the cell body.

Tension applied to the nucleus, F_{N1} , is obtained as

$$F_{N1} = \left(\frac{L_{N1}}{L_{N0}} - 1 \right) K_N = (\lambda_{N1} - 1) K_N, \quad (6.19)$$

where λ_{N1} is the stretch ratio of nuclear longitudinal length, i.e.,

$$L_{N1} = L_{N0} \cdot \lambda_{N1} \quad (6.20)$$

Tension applied to the actin filament, F_A , is

$$F_{A1} = \left(\frac{L_{A1}}{L_{A0}} - 1 \right) K_A = (\lambda_{A1} - 1) K_A, \quad (6.21)$$

where λ_{A1} is the stretch ratio of each AF, i.e.,

$$L_{A1} = L_{A0} \cdot \lambda_{A1}, \quad (6.22)$$

From the balance of forces,

$$2F_{A1} = F_{N1}. \quad (6.23)$$

From Eqs. 6.19–6.21, we obtain

$$\frac{(\lambda_{NI}-1)}{2(\lambda_{AI}-1)} = \frac{K_A}{K_N}. \quad (6.24)$$

Assume the nucleus is k times stiffer than the surrounding cytoskeleton, then

$$\frac{(\lambda_{NI}-1)}{2(\lambda_{AI}-1)} = \frac{K_A}{K_N} = \frac{1}{k}, \text{ i.e., } \lambda_{AI} = (\lambda_{NI} - 1) \frac{k}{2} + 1. \quad (6.25)$$

For simplicity, let us assume that the AFs have the same length with the nucleus at no-load state:

$$L_{A0}=L_{N0}. \quad (6.26)$$

From the geometrical relationship in Fig. 6.5,

$$(2L_{A0} + L_{N0})^2 = L_{C0}^2 + W_{C0}^2 \quad (6.27)$$

$$W_{C0}=L_{C0} \cdot \tan \alpha_0, \quad (6.28)$$

$$(2L_{A1} + L_{N1})^2 = L_{C1}^2 + W_{C1}^2 \quad (6.29)$$

By taking Eqs. 6.17, 6.18, 6.20, 6.22, 6.25, 6.26, 6.27, 6.28 into Eq. 6.29, we obtain

$$(1 + \tan^2 \alpha_0)(2\lambda_{AI} + \lambda_{NI})^2 = 9 \left(\lambda_{CI}^2 + \tan^2 \alpha_0 \cdot \frac{1}{\lambda_{CI}} \right). \quad (6.30)$$

By taking (6.25) into (6.30), a quadratic equation for λ_{NI} is obtained. By solving it, we get

$$\lambda_{NI} = \frac{\left[\sqrt{\frac{9}{1+\tan^2 \alpha_0} \left(\lambda_{CI}^2 + \frac{\tan^2 \alpha_0}{\lambda_{CI}} \right) + k - 2} \right]}{k+1}. \quad (6.31)$$

Alignment angle of the nucleus α_0 is around 15° in my study (Fig. 5.3(a) in Section 5.2.1) and it has been reported that the nucleus is approximately 5 to 10 times stiffer than the surrounding cytoskeleton (Lammerding 2011). By taking $\alpha_0 = 15^\circ$ and $k = 8$ into Eq. 6.31. Then the following equation is obtained

$$\lambda_{NI} = 1.108 \quad (6.32)$$

which is very close to the value obtained in the present study ($\lambda_{NI} = 1.088$ for 3D, 1.14 for 2D).

Axial stretch case

In the axial stretch case, the model (Fig.6.6) projected to the plane containing the four actin filaments in Fig.6.4 was used for simplicity. It might be better to use a model projected to the z - θ plane, but because the angle α seldom change in response to the axial stretch and the $\cos \alpha_0$ is close to unity (0.966), so this model was used. Subscripts of dimensions change from 0 to 2 in response to the circumferential stretch. The AF aligns in the longitudinal direction of the cell at no-load state and rotates β_2 in response to the axial stretch. To meet the condition of my experiment, the cell body was assumed to be stretched 1.35 times the original length in the transversal direction. So, the stretch ratio of the cell body in the axial stretch λ_{Ct} is

$$\lambda_{Ct} = \frac{W_{C2}}{W_{C0}} = 1.35, \quad (6.33)$$

and because the cell body is incompressible,

$$L'_{C2} = L'_{C0} \lambda_{Cl} = L'_{C0} \sqrt{\frac{1}{\lambda_{Ct}}}. \quad (6.34)$$

In the axial stretch, the nucleus is stretched both in the axial and circumferential directions by the four actin filaments. Considering stress-strain relationship in 2D, the deformation of the nucleus would be

$$\varepsilon_{Nl} = (\lambda_{Nl} - 1) = \frac{1}{E_N} (\sigma_{Nx} - \nu \sigma_{Ny}) = \frac{w_{N0}^2}{K_N} \cdot \left(\frac{2F_{A2} \cos \beta_2}{w_{N0}^2} - \nu \frac{2F_{A2} \sin \beta_2}{w_{N0} \cdot L_{N0}} \right), \quad (6.35)$$

$$\varepsilon_{Nt} = (\lambda_{Nt} - 1) = \frac{1}{E_N} (\sigma_{Ny} - \nu \sigma_{Nx}) = \frac{w_{N0}^2}{K_N} \cdot \left(\frac{2F_{A2} \sin \beta_2}{w_{N0} \cdot L_{N0}} - \nu \cdot \frac{2F_{A2} \cos \beta_2}{w_{N0}^2} \right), \quad (6.36)$$

where ε_N , λ_N , and σ_N are nominal strain, stretch ratio, and nominal stress, respectively, of the nucleus with the subscript l and t for the longitudinal and transversal directions, respectively, K_N and E_N are the stiffness and the Young's modulus of the nucleus, respectively, ν is the Poisson's ratio and taken as 0.5, and F_{A2} is the tension in each

AF applied to the nucleus which is defined as

$$F_{A2} = (\lambda_{Al} - 1) \cdot K_A, \quad (6.37)$$

where λ_{Al} is the stretch ratio of the actin filament and K_A is its stiffness.

From Fig. 6.4, it is known that

$$n = \tan \alpha_0 = W_{C0}/L_{C0} = W_{N0}/L_{N0} \quad (6.38)$$

By taking Eqs.6.37, 6.38, and $\nu = 0.5$ into Eqs.6.35 and 6.36, we obtain:

$$(\lambda_{Nl} - 1) = \frac{K_A(\lambda_{Al}-1)}{K_N} (2\cos\beta_2 - n \sin \beta_2), \quad (6.39)$$

$$(\lambda_{Nt} - 1) = \frac{K_A(\lambda_{Al}-1)}{K_N} (2n \sin\beta_2 - \cos \beta_2). \quad (6.40)$$

From Eqs. 6.25, 6.39 and 6.40,

$$\sin \beta_2 = \frac{k\{(\lambda_{Nl}-1)+2(\lambda_{Nt}-1)\}}{3 \cdot n \cdot (\lambda_{Al}-1)} \quad (6.41)$$

$$\cos \beta_2 = \frac{k\{2(\lambda_{Nl}-1)+(\lambda_{Nt}-1)\}}{3 \cdot (\lambda_{Al}-1)} \quad (6.42)$$

From the geometrical relationship in Fig. 6.13,

$$\sin \beta_2 = \frac{W_{N0} \lambda_{Ct} - W_{N0} \lambda_{Nt}}{2L_{A0} \lambda_{Al}} = \frac{W_{N0}}{L_{N0}} \cdot \frac{\lambda_{Ct} - \lambda_{Nt}}{2\lambda_{Al}} \quad (6.43)$$

$$\cos \beta_2 = \frac{L_{C0} \sqrt{\frac{1}{\lambda_{Ct}}} - L_{N0} \lambda_{Nl}}{2L_{A0} \lambda_{Al}} = \frac{L_{N0}}{L_{A0}} \cdot \frac{3 \sqrt{\frac{1}{\lambda_{Ct}}} - \lambda_{Nl}}{2\lambda_{Al}}. \quad (6.44)$$

From another geometrical relationship in Fig. 6.6,

$$\left(\frac{W_{N0} \lambda_{Ct} - W_{N2}}{2}\right)^2 + \left(\frac{L_{C2} - L_{N2}}{2}\right)^2 = (L_{A2})^2 = (L_{A0} \lambda_{Al})^2, \text{ i.e.,} \quad (6.45)$$

$$n^2 (\lambda_{Ct} - \lambda_{Nt})^2 + \left(3 \sqrt{\frac{1}{\lambda_{Ct}}} - \lambda_{Nl}\right)^2 = 4 \cdot (\lambda_{Al})^2 \quad (6.46)$$

From Eqs. 6.41 and 6.43,

$$\frac{\lambda_{Al}-1}{\lambda_{Al}} = \frac{2k\{(\lambda_{Nl}-1)+2(\lambda_{Nt}-1)\}}{3n^2(\lambda_{Ct}-\lambda_{Nt})}. \quad (6.47)$$

From Eqs. 6.42 and 6.44, we obtain

$$\frac{\lambda_{Al}-1}{\lambda_{Al}} = \frac{2k\{2(\lambda_{Nl}-1)+(\lambda_{Nt}-1)\}}{3 \left(3 \sqrt{\frac{1}{\lambda_{Ct}}} - \lambda_{Nl}\right)}. \quad (6.48)$$

Eqs. 6.46-6.48 are three independent equations for three variables λ_{Al} , λ_{NI} , and λ_{Nt} , and we can solve these equations numerically. By taking $n = \tan 15^\circ$, $k = 8$ and $\lambda_{Ct} = 1.35$ into them, we obtain

$$\lambda_{Nt} \approx 1.020, \quad (6.49)$$

which is much smaller than the λ_{NI} in the circumferential stretch (1.108) and almost similar to the present results ($\lambda_{Nt} = 1.005$ for 3D study and 1.06 for 2D study). This model explains the deformation behavior of the nucleus not only qualitatively but also quantitatively and supports the hypothesis on anisotropic deformation of the nucleus.

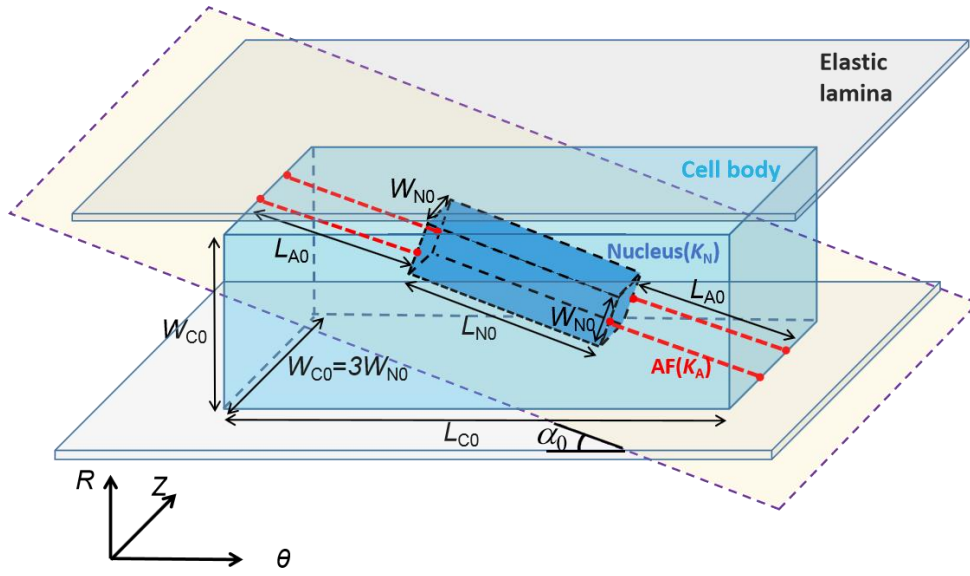


Fig. 6.4 Simple model of a lamellar unit at no-load state.

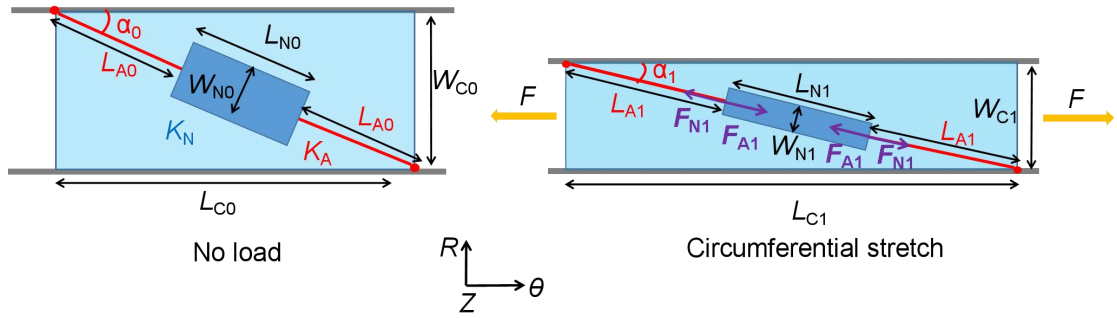


Fig. 6.5 The cell and the nucleus subjected to the circumferential stretch.

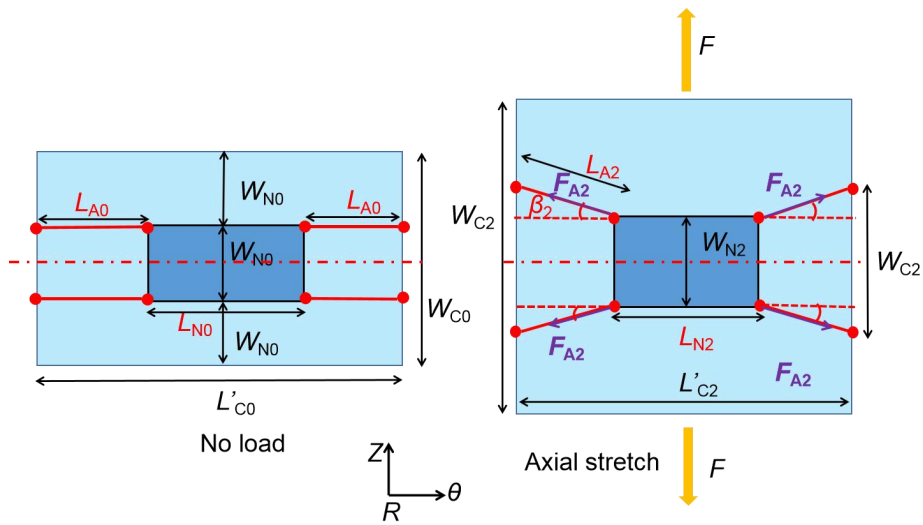


Fig. 6.6 The cell and the nucleus subjected to the axial stretch.

6.5 Comparison of the present results with biaxial stretch case

In this study, no constraint was applied to the specimen in the axial directions for the circumferential stretch, and no constraint was applied to the specimen in the circumferential directions for the axial stretch case. But in a physiological state, the aortic wall is stretched in both circumferential and axial directions, and the intraluminal pressure is also applied. What happens in such a case? Let us assume that a thick section of the aorta is being stretched biaxially as shown in Fig.6.7, and this section including the nucleus can be regarded as an isotropic material. According to the inverted form of the Hooke's law for an isotropic elastic solid (Fung 1993):

$$\varepsilon_{\theta} = \frac{1}{E}[\sigma_{\theta} - \nu(\sigma_Z + \sigma_R)], \quad (6.50)$$

$$\varepsilon_Z = \frac{1}{E}[\sigma_Z - \nu(\sigma_{\theta} + \sigma_R)], \quad (6.51)$$

$$\varepsilon_R = \frac{1}{E}[\sigma_R - \nu(\sigma_{\theta} + \sigma_Z)], \quad (6.52)$$

where the $\varepsilon_{\theta}, \varepsilon_Z$ and ε_R indicate the strain of the specimen in circumferential, axial and radial directions; the $\sigma_{\theta}, \sigma_Z$ and σ_R indicate the stress in circumferential, axial and radial directions; ν refers the Poisson's ratio; E is the Young's modulus of the specimen.

In this study, for example, $\sigma_R = \sigma_Z = 0$ in the case of circumferential stretch and thus $\varepsilon_{\theta} = 0.40$. While in the physiological state, σ_Z is positive and has a value of about 127 kPa, σ_R is negative and has a value about 70 kPa (Matsumoto and Hayashi, 1996), and the $\varepsilon_{\theta} \approx 0.61$. Thus, circumferential strain used in this study was 34.4% smaller than the value expected in a physiological state. So, the future experiment may

concentrate on the biaxial stretch case, which mimics the physiological state more closely.

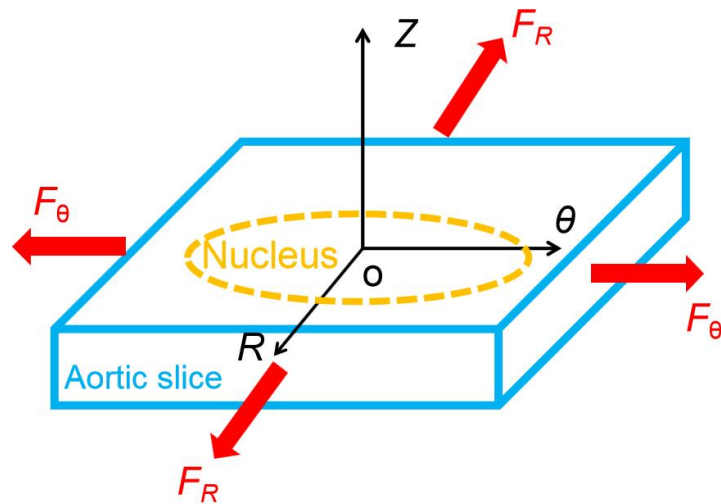


Fig. 6.7 Hypothetical biaxial stretch of a type 2 slice. Z , vascular axial direction; θ , vascular circumferential direction; R , vascular radial direction.

6.6 Deformation of the nucleus and the cell body under physiological condition.

To examine whether the cell viability affects the results obtained in the present study, an additional experiment in which living cultured cells were stretched was performed in their longitudinal and transversal directions.

In short, smooth muscle cells obtained from genetically engineered mice whose actin filaments were combined with a green-fluorescent protein (GFP) were plated in a PDMS chamber (STB-CH-0.2-H4, STREX, Japan) and cultured for 24 hours. Cell nuclei were stained with DRAQ5 (Thermo Fisher Scientific Inc., USA). Then the cells on the chamber were deformed under a microscope maintained at 38°C by stretching the chamber by 20-25%. Elliptical cells with elongated nucleus (ratio of major axis to minor axis is larger than 1.5) and aligned in the stretch direction or perpendicular to the stretch direction were selected and the deformation of the cell body and the nucleus were measured as shown in Fig. 6.8. Results were summarized in Tables 6.2 and 6.3, in which the strain applied to the nuclei in the stretch direction was normalized with the strain applied to the cell body, $(A_N-1)/(A_C-1)$. The normalized deformation of the nucleus was smaller than 1 for both cell types, indicating that the nucleus is less deformable than the cell body, which corresponds to my conclusion in chapters 3-5. And also, it was significantly smaller in the cells aligned perpendicular to the stretch direction than in the cells aligned in the stretch direction ($P < 0.001$), indicating that even in cultured alive cells, the nucleus is less

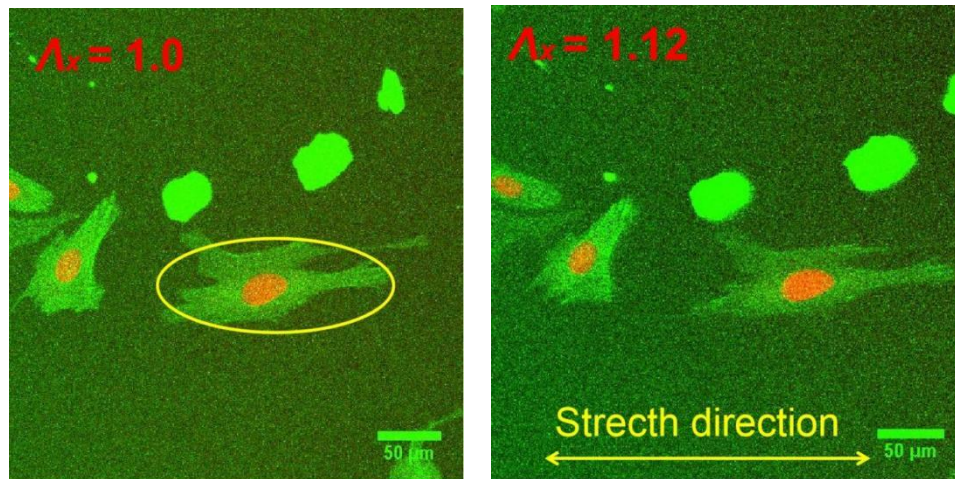
deformable in its transversal direction (vascular axial direction) than its longitudinal direction (vascular circumferential direction), which corresponds to my conclusion.

Table 6.2 Relative deformation of the nucleus to the cell body in the cells aligned in the stretch direction.

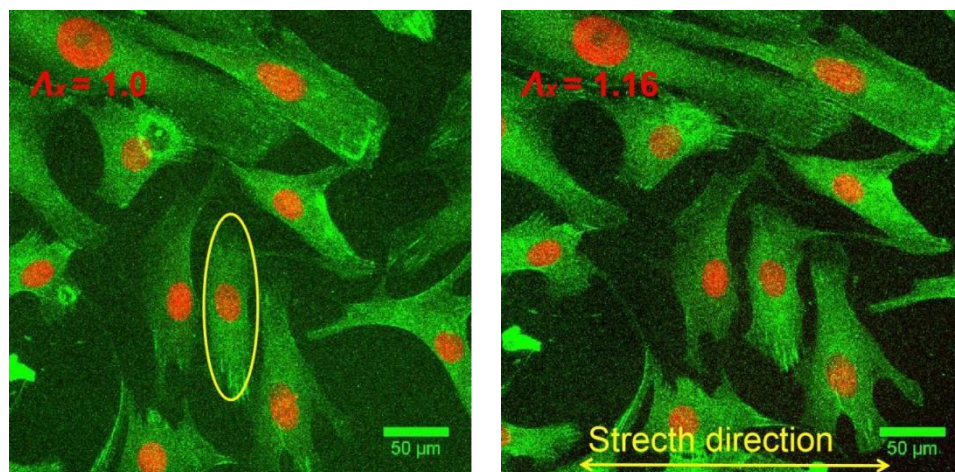
	Cell #1	Cell #2	Cell #3	Cell #4	Cell #5	mean \pm SD
$(A_{Ni}-1)/(A_{Ci}-1)$	0.873	0.535	0.562	0.822	0.823	0.723 ± 0.161

Table 6.3 Relative deformation of the nucleus to the cell body in the cells aligned perpendicular to the stretch direction.

	Cell #6	Cell #7	Cell #8	Cell #9	Cell #10	mean \pm SD
$(A_{Ni}-1)/(A_{Ci}-1)$	0.195	0.158	0.135	0.206	0.230	0.185 ± 0.038



(a) A typical cell aligned in the stretch direction (circled)



(b) A typical cell aligned perpendicular to the stretch direction (circled)

Fig. 6.8 Example of cells whose deformation in the stretch direction was measured for the nucleus and cell body. λ_z indicates the deformation of the membrane.

6.7 Physiological implications: Anisotropic nuclear deformation causes the anisotropic response of aortic media to hypertension

When the arterial hypertension occurs, the stress decreases in the axial direction while it remains unchanged in the circumferential direction of the aortic wall compared to the normotensive aorta at a macroscopic viewpoint (Matsumoto et al. 1996). Vaishnav et al (1990) reported a reduced axial extension ratio of the hypertensive aortic segment compared to the normotensive one. They concluded that the tissue growth in the axial direction tends to increase the vessel wall thickness which eventually reduces the axial and circumferential stress. Similar mechanism was also pointed out by Matsumoto et al. (1996) but neither of them discussed the underlying mechanism explaining the difference in the directions. Taking the mechanotransduction via the nucleus (Janota et al., 2000) into account, it is hypothesized in this dissertation that such anisotropic response is caused by anisotropic deformation of the nucleus.

As it has been proposed in chapter 1, it can be reasonably assumed that the deformation of the nucleus causes the enhancement of protein synthesis when hypertension occurs. According to the obtained results in this dissertation, the nucleus is sensitive to the circumferential stimuli but not the axial stimuli. Hence, it is the circumferential stimulation that deforms the nucleus to enhance the protein synthesis, further inducing the vessel hypertrophy.

6.8 Limitations and future works

In this work, the normotensive rabbit aortas were used to perform the tensile tests because according to my hypothesis in Chapter 1, the hypertrophy starts from the normal state of the vessel via the enhanced stimulation of normal SMC.

The experiment was performed at room temperature within 24h after the tissue was harvested. Although the sliced specimens were immersed in PBS solution, the experimental condition was different from *in vivo* state. Besides, any SMC activities were not detected. Thus, the behavior of the SM nuclei obtained in the present study might be different from that obtained in a physiological condition. However, in Section 6.6, an additional stretch experiment with living cultured cells in a physiological condition was performed. The nuclear behavior obtained in the present study was similar to that obtained in Chapters 3–5. Thus, it is reasonable to conclude that the anisotropic behavior of the SM nucleus may occur in the physiological condition.

In the physiological state, the thoracic aorta is stretched in both the axial and circumferential direction to about 1.4 times to the no-load length and blood pressure is applied as a compressive stress in the radial direction. These multiple axis loading conditions were discussed in Section 6.4 and that the nuclear deformation in the physiological state should be smaller than that obtained in this study. Therefore, the conclusion may not be completely recapitulating the actual situation. As the biaxial experiment was very difficult to conduct according to the existing conditions, it has not been performed.

References

- Caille N, Thoumine O, Tardy Y, Meister JJ (2002) Contribution of the nucleus to the mechanical properties of endothelial cells. *J. Biomech.* 35:177–87.
- Davidson PM, Cadot B (2021) Actin on and around the nucleus. *Trends. Cell. Biol.* 31:211–223.
- Fischer T, Hayn A, Mierke CT (2020) Effect of nuclear stiffness on cell mechanics and migration of human breast cancer cells. *Front. Cell. Dev. Biol.* 8:393.
- Fung YC (1993) *Biomechanics: Mechanical Properties of Living Tissues*. Springer, New York. pp.38–40.
- Janota CS, Calero-Cuenca FJ, Gomes ER (2020) The role of the cell nucleus in mechanotransduction. *Curr. Opin. Cell. Biol.* 63:204–211.
- Lammerding J (2011) Mechanics of the nucleus. *Compr. Physiol.* 1: 783–807.
- Li M, Liu LQ, Xi N, Wang YC, Xiao XB, Zhang WJ (2015) Effects of temperature and cellular interactions on the mechanics and morphology of human cancer cells investigated by atomic force microscopy. *Sci. China Life. Sci.* 58:889–901.
- Martens JC, Radmacher M (2008) Softening of the actin cytoskeleton by inhibition of myosin II. *Pflug. Arch. Eur. J. Phy.* 456:95–100.
- Matsumoto T, Hayashi K (1996) Stress and strain distribution in hypertensive and normotensive rat aorta considering residual strain. *ASME. J. Biomech. Eng.* 118:62–73.
- Matsumoto T, Okumura E, Miura Y, Sato M (1999) Effect of smooth muscle cells on the mechanical response of rabbit carotid arteries in culture. *JSME Int. J. C-Mech. Sy.* 42:514–520.
- Owens GK, Schwartz SM (1983) Vascular smooth muscle cell hypertrophy and hyperploidy in the Goldblatt hypertensive rat. *Circ. Res.* 53:491–501.
- Rowat AC, Lammerding J, Ipsen JH (2006) Mechanical properties of the cell nucleus and the effect of emerin deficiency. *Biophys. J.* 91:4649–4664.
- Vaishnav RN, Vossoughi J, Patel DJ, Cothran LN, Coleman BR, Ison-Franklin EL (1990) Effect of hypertension on elasticity and geometry of aortic tissue from dogs. *J. Biomech. Eng.* 112:70–74.

Wang X, Liu H, Zhu M, Cao C, Xu Z, Tsatskis Y, Lau K, Kuok C, Filleter T, McNeill H, Simmons CA, Hopyan S, Sun Y (2018) Mechanical stability of the cell nucleus – roles played by the cytoskeleton in nuclear deformation and strain recovery. *J. Cell. Sci.* 131:jcs209627.

Wiener J, Loud AV, F Giacomelli F, and Anversa P (1977) Morphometric analysis of hypertension-induced hypertrophy of rat thoracic aorta. *Am. J. Pathol.* 88:619–633.

Zhou S, Yang X, Hu J, Mo C, Cao Y, Yang C (2018) Continuous hypergravity alters the cytoplasmic elasticity of MC3T3-E1 osteoblasts via actin filaments. *J. Biomech.* 72:222–227.

Chapter 7 Conclusions

As it has been pointed out in Chapter 1, soft biological tissues consist of various materials with a wide variety of Young's modulus and they have microscopic residual stress caused by such heterogeneity. Thus, deformation of tissues is highly complicated at the cell level, and it is important to measure the microscopic deformation of real tissues directly.

In this work, tensile tests of the aortic slices were performed in the circumferential and axial directions while observing the nuclear deformation both in 2D and 3D as well as the deformation of the AF network. The results showed that 1) the deformation of the nucleus is smaller than the macroscopic deformation of the tissue; 2) the deformation of the actin filaments was almost similar to that of the tissue; 3) the deformation of the nucleus is especially small when the cell is stretched in the direction perpendicular to its longitudinal (transversal) direction. Based on the deformations observed in the present study and the nanostructures of the cell reported in the literature, a novel cell model that explains the smaller nuclear deformation in the axial stretch was proposed. The deformation of this model corresponded well to the real deformation of the actin filament network. The minute deformation of the nucleus in response to the transversal stretch indicates the nucleus is insensitive to the deformation of the tissue in this direction. These findings might lead to a better understanding of that the artery walls do not maintain the axial stress unchanged while they maintain the circumferential stress in response to hypertension.

In this work, the normotensive rabbit aorta was used. Future work contains the stretching experiment with specimens obtained from hypertensive animals. Hypertrophy causes the increase in SMC volume and extracellular matrix (ECM) (Wiener et al. 1977; Owens and Schwartz 1983; Matsumoto et al. 1999), and such volume increase happens in radial and axial directions concomitantly (Matsumoto and Hayashi 1996). So, exploring the difference in the deformability of the nuclei of normotensive and hypertensive SMC will be meaningful to elucidate the mechanotransduction pathway to anisotropic response of aortic media to hypertension.

The spatial deformation of the AF network in a 3D view may also become a meaningful issue. One can use more advanced microscope, for example ZEISS LSM 880 confocal microscope (Carl Zeiss Corporation, Germany) to get stack images of the actin filaments during tensile test, then, input the images into Imaris to build the 3D model of the AF. Then, one can measure the spatial length and orientation angle change of the AF during stretch.

Appendix

Appendix 1

%%Matlab code for calculating Green strain of the smooth muscle layers.

```
function X = Calculation(p)
```

```
XO0=p(1);
```

```
YO0=p(2);
```

```
XP0=p(3);
```

```
YP0=p(4);
```

```
XQ0=p(5);
```

```
YQ0=p(6);
```

```
XO1=p(7);
```

```
YO1=p(8);
```

```
XP1=p(9);
```

```
YP1=p(10);
```

```
XQ1=p(11);
```

```
YQ1=p(12);
```

```
LOP0=sqrt((XP0-XO0)^2+(YP0-YO0)^2);
```

```
LOP1=sqrt((XP1-XO1)^2+(YP1-YO1)^2);
```

```
LPQ0=sqrt((XQ0-XP0)^2+(YQ0-YP0)^2);
```

```
LPQ1=sqrt((XQ1-XP1)^2+(YQ1-YP1)^2);
```

```
LOQ0=sqrt((XQ0-XO0)^2+(YQ0-YO0)^2);
```

```
LOQ1=sqrt((XQ1-XO1)^2+(YQ1-YO1)^2);
```

```
dOPX=abs(XO0-XP0);
```

```

dOPY=abs(YO0-YP0);
dPQX=abs(XP0-XQ0);
dPQY=abs(YP0-YQ0);
dOQX=abs(XO0-XQ0);
dOQY=abs(YO0-YQ0);

A=[2*dOPX^2      2*dOPX*dOPY      2*dOPY^2;2*dPQX^2      2*dPQX*dPQY
2*dPQY^2;2*dOQX^2 2*dOQX*dOQY 2*dOQY^2];

B=[LOP1^2-LOP0^2;LPQ1^2-LPQ0^2;LOQ1^2-LOQ0^2];
C=horzcat(A,B);
if rank(A)==3&&rank(C)==3
    disp('one solution.')
    syms x1 x2 x3;
    f1=2*x1*dOPX^2+2*x2*dOPX*dOPY+2*x3*dOPY^2-(LOP1^2-LOP0^2);
    f2=2*x1*dPQX^2+2*x2*dPQX*dPQY+2*x3*dPQY^2-(LPQ1^2-LPQ0^2);
    f3=2*x1*dOQX^2+2*x2*dOQX*dOQY+2*x3*dOQY^2-(LOQ1^2-LOQ0^2);
    [x1,x2,x3]=solve(f1,f2,f3)
    a=x1;
    b=x3;
    I(1)=sqrt(2*a+1);
    I(2)=sqrt(2*b+1)

else if rank(A)==rank(C)&&rank(C)<3
    disp('Endless solution.')
    a=x1;
    b=x3;
    I(1)=sqrt(2*a+1);
    I(2)=sqrt(2*b+1)

```

```

        else
            rank(A)~=rank(C)
            disp('No solution.')
        end
    end
end

```

Appendix 2

%%Matlab code for calculating AF stepwise deformation.

%% Part one: Searching;

P=[];

A=0; %%for recording the biggest value of the corrcoef;

for idx=1:size(searchregion,1)-size(example,1)+1 %%search in line;

 for idy=1:size(searchregion,2)-size(example,2)+1 %%control the volume;

S=imread('searchregion.tif','PixelRegion',[idx,(idx+(size(example,1)-1))],[idy,(idy+(size(example,2)-1))]);

 unfold1=double(example(:));

 unfold2=double(S(:));

 R=corrcoef(unfold1,unfold2)

 R(1,2);

 var(unfold1);

 var(unfold2);

 A=R(1,2)/(var(unfold1)*var(unfold2)); ;

 P=[P,A];

end

end

Position = find(P==max(max(P)))

a = rem(Position,(size(searchregion,2)-size(example,2))+1);

b = (Position-a)/(size(searchregion,2)-size(example,2)+1);

Objectimage

=

imread('searchregion.tif','PixelRegion',{[b+1,b+1+size(example,1)-1],[a,a+size(example,2)-1]});

%% show the photo depend on the coordinates got;

imshow(Objectimage);

%%Part two: Matching;

A= before[-(size(before,2)/2),(size(before,2)/2];

B= after[-(size(after,2)/2),(size(after,2)/2)]; %% input the two photo been searched and named A and B;

C = 0;

P=0;

I=0;

J=0; %% C is used for saving value of P, I and J used for saving the maxi and j;

interval=0.005;

a=0.005;

b=0.2; %% the upper and bottom value for;

for i = a:interval:b

for j = a:interval:b

translate_m = affine2d([1+i 0 0;0 1-j 0;0 0 1]); %% make a trasnform

```

matrix;

before_t = imwarp(A,translate_m);
if rem(size(before_t,2)-size(before,2),2)==0
    cut_before_t = imcrop(before_t,[(size(before_t,2)-size(before,2))/2+1
1 (size(before,2)-1) (size(before_t,1)-1)]);

    if rem(size(before,1)-size(before_t,1),2)==0
        cut_after = imcrop(after,[1 (size(after,1)-size(before_t,1))/2+1
size(after,2)-1 size(before_t,1)-1]);
    else
        cut_after = imcrop(after,[1 ((size(after,1)-size(before_t,1))-1)/2+1
size(after,2)-1 size(before_t,1)-1]);
    end

else
    cut_before_t = imcrop(before_t,[(size(before_t,2)-size(before,2))+1)/2+1
1 size(before,2)-1 size(before_t,1)-1]);
    if rem(size(before,1)-size(before_t,1),2)==0
        cut_after = imcrop(after, [1 (size(after,1)-size(before_t,1))/2+1
size(after,2)-1 size(before_t,1)-1]);
    else
        cut_after = imcrop(after, [1 ((size(after,1)-size(before_t,1))-1)/2+1
size(after,2)-1 size(before_t,1)-1]);
    end
end

%% next, calculating correlation coeff.;
unfold1 = double(cut_before_t(:));
unfold2 = double(cut_after(:));

```



```

        R = corrcoef(unfold1,unfold2);
        R(1,2);
        var(unfold1);
        var(unfold2);
        P=R(1,2)/(var(unfold1)*var(unfold2));

        if P>C
            C = P;
            I=i;
            J=j;
        end

    end

end

disp(I)
disp(J)

```

